Dissertation

zur Erlangung des akademischen Grades
doctor rerum naturalium
(Dr. rer. nat.)

Coupling diode laser desorption with plasma ionization in mass spectrometry for analytical and biomedical applications

vorgelegt von

Alexander Knodel

geboren in Herdecke

Dortmund 2021

Fakultät Physik
Technische Universität Dortmund

und

Leibniz-Institut für Analytische Wissenschaften - ISAS - e.V.
Bunsen-Kirchhoff-Straße 11

44139 Dortmund

Datum der Einreichung:	26.03.2021
Datum der mündlichen Prüfung:	28.05.2021

Prüfungskomission:

Vorsitzender der Prüfungskomission:	Prof. Dr. Jan Kierfeld
1. Gutachter:	PD. Dr. Joachim Franzke
2. Gutachter:	Prof. Dr. Manfred Bayer
Vertreter der wiss. Mitarbeiter:	Dr. Armin Lühr

Abstract

This thesis focuses on the coupling of laser desorption with plasma ionization in mass spectrometry for analytical and biomedical applications. A diode laser is used to trigger thermal desorption of substances from a surface. For this reason, a metal-isolator sandwich structure is developed and conceptually tuned to analytical demands on the basis of a microscope slide, lithography and sputtering. The neutral desorbate is then ionized by a flexible, atmospheric pressure micro plasma and is finally detected by a mass spectrometer. Different analyte classes are investigated to evaluate the method, ranging from analytical standards to complex samples.
These insights are extended to an automated imaging of biological tissue, which requires an adaption of the substrate design. The inherent laser-based and thermal surface effects are intensively studied and optimized to the imaging. As a result, the imaging of biological samples is simplified, faster and can be carried out in ambient air without the need of a chemical matrix, which can be applied to routine analysis in life sciences. The limits of the method are finally evaluated.

Diese Arbeit beschäftigt sich mit der Kopplung von Laser-Desorption mit Plasma-Ionisierung für die Massenspektrometrie von analytischen und biomedizinischen Proben. Bei dieser Messmethodik wird ein Diodenlaser zur thermisch gesteuerten Desorption von Proben von einer Oberfläche benutzt. Auf Basis von Objektträgern, der Lithografie und der Kathodenzerstäubung wird eine zweilagige Metall-Isolator Substratstruktur für die Laser-Desorption entwickelt und auf die analytischen Anforderungen optimiert. Das durch die Laser-Desorption entstehende neutrale Desorbat wird mittels eines flexiblen, bei Atmosphärendruck arbeitenden Mikroplasmas ionisiert und schließlich mit einem Massenspektrometer detektiert. Die Methode wird an verschiedenen Analytklassen evaluiert, die von analytischen Standards bis zu komplexen Proben reichen.
Als Erweiterung der analytischen Standards wird eine automatisierte Bildgebung an biologischen Proben vorgestellt, welche eine abgewandelte Substratstruktur erfordert. Die damit einhergehenden Laser-basierten und thermischen Oberflächeneffekte werden untersucht und zur Optimierung der Methodik herangezogen. Dadurch lassen sich biologische Proben einfacher, schneller und unter Umgebungsbedingungen ohne chemische Matrix untersuchen, was in der Routineanalytik in den Lebenswissenschaften Anwendung finden kann. Schließlich werden die Grenzen der Messmethode eruiert.

Contents

List of Abbreviations

AGC	Automatic Gain Control
AIMS	Ambient Air Mass Spectrometry
APCI	Atmospheric Pressure Chemical Ionization
(AP-)MALDI/SALDI	(Atmospheric Pressure) Matrix- or Surface-assisted Laser Desorption Ionization
a.u.	Arbitrary Units
CAD	Computer-Aided Design
DAQ	Data Acquisition
DART	Direct Analysis in Real Time
DBD(I)	Dielectric Barrier Discharge (Ionization)
DC	Direct Current
(D)ESI	(Desorption) Electrospray Ionization
DLD-PI MSI	Diode Laser Desorption, Plasma Ionization Mass Spectrometry Imaging
DLPC	1,2-dilauroyl-sn-glycero-3-phosphocholine
FAPA	Flowing Atmospheric-Pressure Afterglow
FDA	Frequency Domain Analysis
FEP	Fluorethylenpropylen
FFT	Fast Fourier Transform
FWHM	Full Width (at) Half Maximum
FμTP	Flexible Microtube Plasma
GC-MS	Gas Chromatography-Mass Spectrometry
HMDS	Hexamethyldisilazan
(I)CCD	(Intensified) Charge-coupled Device
(i)LTP	(Inverse) Low Temperature Plasma
IR	Infrared

IT	Injection Time
LAESI	Laser-assisted Electrospray Ionization
LD-DBDI-MS	Laser Desorption, Dielectric Barrier Discharge Ionization Mass Spectrometry
LD-LTP	Laser Desorption, Low Temperature Plasma (Ionization Mass Spectrometry)
LOD	Limit of Detecton
LOL	Limit of Linearity
LOQ	Limit of Quantification
MeOH	Methanol
MRFA	Methionin-Arginin-Phenylalanin-Alanin
MS	Mass Spectrometer
m/z	Mass-to-Charge Ratio
Nd:YAG	Neodymium-doped Yttrium Aluminum Garnet
NSAID	Non-steroidal Anti-inflammatory Drug
PAL	Phase Alternating Line
PALDI	Plasma-assisted Laser Desorption Ionization
PEEK	Polyetheretherketone
PMMA	Polymethyl Methacrylate (Acrylic Glass)
PTFE	Polytetrafluorethylene
RF	Radio Frequency
ROI	Region of Interest
SIM	Selected Ion Monitoring
SIMS	Secondary Ion Mass Spectrometry
SPM	Sphingomyelin
TIC	Total Ion Chromatogram
t-MALDI-MS	Transmission (mode) Matrix-assisted Laser Desorption Ionization Mass Spectrometry
TTL	Transistor-Transistor Logic
u	Unified Atomic Mass Unit (Dalton, Da)
VLF	Very Low Frequency
XIC	Extracted-Ion Chromatogram

1 Introduction and Motivation

Mass spectrometry is a versatile technique used in the analysis from elements to molecular species and their reaction patterns, combining almost all natural sciences from chemistry, medicine, biology, physics and even computer science in one field only. It is therefore used in numerous applications, such as in life sciences, petroleum industry, quality control, military or even in cosmic space [1].

The main characteristic of mass spectrometry is the detection of atoms or molecules, which are firstly ionized in the gas phase and consequently separated by their mass-to-charge (m/z) ratio with a certain ion intensity in a mass spectrum. The target molecule for analysis is called the *analyte*. The analyte can be a standard with a known concentration or a molecule in an unknown sample. The two notions of standards and analytes are synonymously used throughout this thesis as no identification of unknown substances is carried out.

Assuming single charged species, the spectrum helps to identify an analyte by its mono-isotopic mass. Many effects can modify the observed species, ranging from the fragmentation, dissociation, protonation to the adduct formation. The capability of ionizing molecules without fragmentation is vaguely called *soft ionization*. In that case, the analyte is detected as a molecular ion or as protonated species (*quasi-molecular ion*). In rare cases, multi-charged ions are observed, for instance using electrospray ionization methods [2]. However, the efficiency of the ion detection is a complex topic, as many processes are convoluted in mass spectrometry. For that reason, research groups mostly specialize on a single aspect of mass spectrometry. For instance, an aspect may cover the detection of certain classes of analytes such as lipids or proteins or the sample feed and the ion generation.

Different approaches are suggested in literature in order to transfer the analyte to the gas phase [3, 4]. Besides well-established methods such as gas chromatography, lasers have gained lots of interest as they can be used as an effective heating source and for imaging applications in mass spectrometry.

The most prominent laser-based method in mass spectrometry is matrix-assisted laser desorption ionization (MALDI). MALDI utilizes a photosensitive, chemical matrix on desorption substrates for both desorption and ionization of the analyte by a laser. This method is commonly carried out under vacuum conditions. However, these vacuum conditions complicate measurements for routine analysis. Moreover, the ion yield is around 10^{-5}, demanding for the coupling of an additional ionization source after laser application [5]. Examples for these hybrid methods are laser ablation electrospray ionization (LAESI) [6] or plasma-assisted laser desorption ionization (PALDI) [7].

Plasmas are extensively studied since early 1920s [8] and are used in numerous fields in both research and industry, such as surface coating [9], lightning technology [10] or plasma welding [11]. From a simplified point of view, plasmas are partially ionized gases driven by charge carriers and uncharged particles. Dielectric barrier discharges (DBD) [12] are one type of plasmas, in which the plasma is not in direct contact with the electrodes, but shielded by a dielectric, commonly glass. The dielectric also confines the plasma expansion and thus dictates the necessary gas pressure and generator voltage required for ignition, according to the law of Paschen [13] and similitude model scaling [14]. In case of millimeter-discharges, the operating gas pressure is at atmospheric pressure. Mostly inert noble gases such as Helium are used. DBDs are easy-to-use within existing setups as they are compact-build basically using a gas pipe, a glass capillary and at least one electrode attached to a voltage generator. However, plasmas are complex tools, as they are susceptible to its operational conditions, such as the discharge volume, choice of noble gas or voltage applied [15, 16]. Further characteristics of plasmas with a focus on DBDs and similar ionization sources for mass spectrometry will be briefly described in the next chapter.

In this thesis, a flexible and miniaturized plasma is coupled with a diode laser in mass spectrometry. On the one hand, this combination decouples the desorption of molecules and their ionization for mass spectrometry. On the other hand, lower laser intensities compared to pulsed neodymium-doped yttrium aluminum garnet (Nd:YAG) lasers can be used. For the specific combination of the diode laser and the plasma, desorption substrates are developed, characterized and used with analytical standards and biological tissue in mass spectrometry.

The fundamentals will deal with the concepts of mass spectrometry, described on

the basis of an ion trap and a quadrupole mass analyzer. The basics of diode lasers and laser-surface-interaction as well as plasma-based ionization will complete the fundamentals.

The third chapter will introduce the different methods and setups used in this work. In this sense, a diode laser is presented as a low-price, compact and robust alternative to cost-intensive and room-filling pulsed Nd:YAG lasers. For ionization, a recent study [4] suggests that ionization in a small area is achieved with micrometer plasmas. Therefore, the flexible microtube plasma (FμTP) [17] is chosen, taking only 250 µm in inner diameter. In this concern, close distances to the inlet of the mass spectrometer can be achieved without particle transport to the inlet of the mass spectrometer.

Previous research [18] outlined the lack of reproducible droplet deposition and criticized non-standardized ink spots for laser desorption. Motivated from this niche, chapter four will begin with a systematic material study to construct metal-glass desorption substrates. After material decision, the substrates are tuned using lithography and sputtering that help to tackle the aforementioned issues. The laser intensity required for desorption of analytical standards will be quantized by using both the laser spot area and the desorption area on the surface. On basis of these results, the laser-surface interaction and different intensity thresholds of the analytes required for desorption will be outlined. An important topic will deal with the formation of a laser-induced plasma on the surface.

The fifth chapter will cover the analytical perspective, describing cholesterol as a model analyte for the group of lipids, even in a chemical matrix and in a complex sample. The ionization mechanism of other hydrophobic compounds in positive and negative ionization will be covered as well. In that regard, the analytical performance of the methods will be outlined. Finally, propazine, as a representative of the pesticides of the previous study [18], is taken to compare the desorption substrates from this thesis to the substrate design of the authors.

In chapter six, laser desorption, plasma ionization mass spectrometry is carried out on animal tissue, which leads to a different substrate design. In this manner, different laser-induced thermal effects are systematically investigated. The possibilities and limits of diode lasers are inherently discussed. Software for screening the tissue and a post processing script are developed and described, which allow mass spectrometry imaging even on low-cost and in existing experiments. Two scanning modes of the

substrate design are compared. Finally, a reconstructed image of mouse liver tissue is presented and linked to the morphology of the tissue.

In the last chapter, the limits of the method are critically discussed. In that manner, physical parameters such as the decrease rate in laser desorption or the particle density of the desorbed analyte molecules are given and compared in different experimental setups. Further, the desorption and ionization limits are discussed, which are related to the questions whether guided transport of the particles or external ion focusing are required. In addition, a bias potential will be used on the substrate to compare the tuning methods of MALDI to this method. Moreover, charge effects on the substrate are investigated, which will finish the main body of this thesis.

2 Fundamentals of Mass Spectrometry, Laser Desorption and Plasma Ionization

The first part of the fundamentals presented in this chapter briefly outlines the general characteristics of mass spectrometry by means of an ion trap mass spectrometer. While the detector rather strikes as a black box, both the sample feed and the ion generation can be fully customized. Through the scope of this thesis, the sample is dried on a surface and thermally desorbed to the gas phase using a laser. Therefore, the characteristics of laser diodes and laser-surface interaction are addressed. On that basis, different laser-based desorption methods used in mass spectrometry are presented. In these methods, only a small fraction of the desorbate is ionized. Therefore, plasmas are subsequently presented as a versatile, yet robust and easy-to-use tool for ionization after laser desorption in mass spectrometry. It is worth noting that these fundamentals are limited to the contents of this thesis. A general description of the basic concepts of mass spectrometry, lasers and plasmas is optimally given in textbooks only.

2.1 Mass Spectrometry

This section will cover two types of mass spectrometers as well as a description of a basic calibration method used for the analysis of a compound in mass spectrometry.

2.1.1 Three Dimensional Ion Trap Mass Spectrometry

A mass spectrometer (MS) consists of an ion source, ion optics, a mass analyzer, and a detector. A simplified schematic of a Paul ion trap mass spectrometer with an ion transfer capillary is shown in Figure 2.1. The *LCQ DecaXP* [20] is one of numerous commercially available ion trap mass spectrometers that will be extensively used

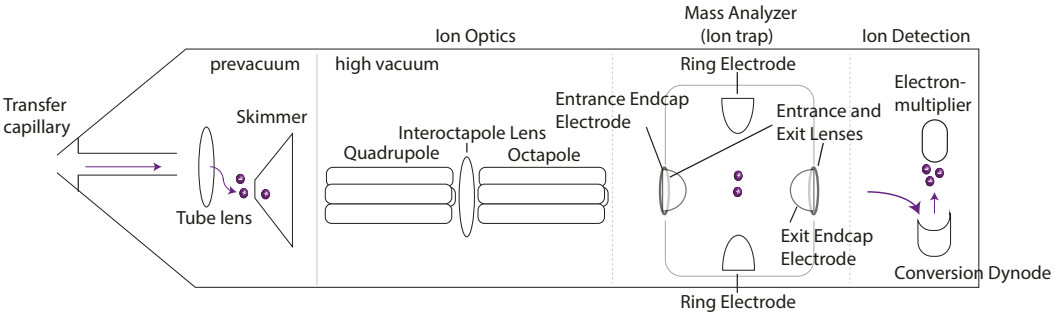

Figure 2.1: Simplified schematic of a Paul ion trap mass spectrometer with an ion transfer capillary, conceptually based on the contents of the manual[19].

within this thesis. The parameters of the LCQ are summarized in Table A.1 of the appendix.

The inlet of the mass spectrometer is a cylindrical transfer capillary that is heated to 250 °C and is set to a bias potential. The ions are inserted into the capillary at atmospheric pressure and guided by a pressure gradient to the tube lens and the skimmer region (1 mbar, prevacuum).

The tube lens focuses the ions on the sampling orifice of the skimmer, with a mass depended potential called tube lens voltage. The tube lens voltage is used to deflect one ion species of either positive or negative polarity. Therefore, neutrals are separated from the ions, as only ions are deflected through the s-shaped pathway. The skimmer is a cone with sampling orifice of a decreased diameter to reduce the gas load into the next section.

The ions are guided to the ion optics, consisting of numerous lenses, at 10^{-3} mbar (high vacuum). These lenses refocus the ions and are set on different potentials for the ion transmission, which are summarized in Table A.1 of the appendix. The ions are guided to the mass analyzer that stores, isolates and performs a scan on the collected ions.

The mass analyzer is set on a DC offset voltage and equipped with an entrance lens to inject ions from the ion optics. The automatic gain control (AGC) controls the amount of ions injected to the ion trap by a preliminary ion scan. This mass spectrometer includes a specialized design of an ion trap, called Paul ion trap. The ions are trapped by a centered ring electrode and two pairs of end cap electrodes, which have a hyperbolic surface on their insides. This geometry generates a quadrupole electric field. An RF potential generates an elliptic deformation of

the ion cloud on a single axis each phase, resulting in an effective ion oscillation in three dimensions. Additional RF potentials are applied to the ring and end cap electrodes for trapping, fragmentation or mass-selective ejection of the ions. A Helium damping gas is introduced through a nipple on the exit end cap electrode, maintaining a constant total pressure of 10^{-3} mbar. This enhances the sensitivity and the spectral resolution by reducing the oscillation amplitude of the ions by collisions with the background gas. Those ions are hence both trapped and ejected through the exit lens with a smaller ion beam that reduces the ion loss.

At a pressure of 10^{-5} mbar, the ions are guided from the mass analyzer to the conversion dynode. This dynode is formed as a concave metal electrode, which generates secondary particles and focuses them onto the multiplier by a voltage gradient. Residual negative ions are converted into electrons in the multiplier by wall collision. A gain factor influences the multiplication of electrons from a single particle. An electron current is measured on the anode that is proportional to the number of the total secondary particles. In a total ion chromatogram (TIC), the summed ion intensity is displayed in arbitrary units on the ordinate and the scan time on the abscissa. Likewise, the chromatogram gathered from a segment of the TIC is called extracted-ion chromatogram (XIC).

2.1.2 Quadrupole Mass Spectrometry

In contrast to ion trap mass spectrometers, quadrupole mass spectrometers do not include an ion trap. Instead, at least one quadrupule is used as a mass analyzer. The *TSQ Vantage* [20] is a triple quadrupole mass spectrometer, visualized in Figure 2.2.

From the heated ion transfer capillary, the ions propagate to the S-lens and the exit lens, which are similar to the tube lens and the skimmer of the LCQ mass spectrometer. The ions propagate to the ion optics at high vacuum through several lenses and the quadrupole Q0 towards the mass analyzer region. The first quadrupole in Figure 2.2 is usually discarded from the counting and hence labelled Q0. The vacuum conditions and ion paths are similar to the LCQ mass spectrometer, only varying in applied potentials and frequencies due to the different design of the mass spectrometer, which are addressed in Table A.2 of the appendix.

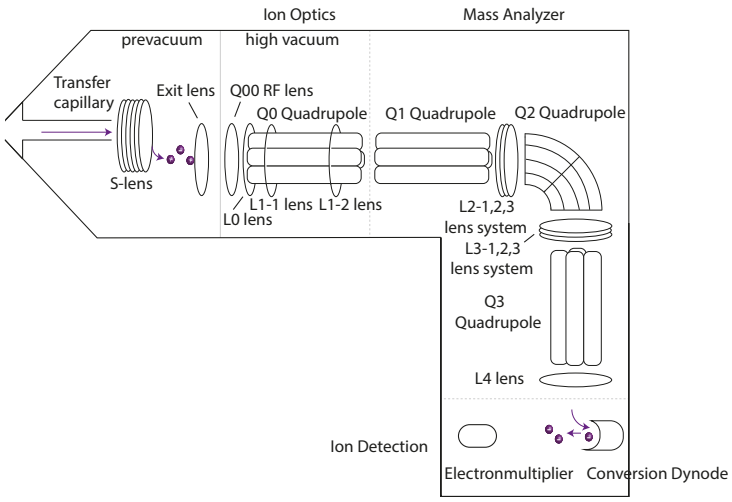

Figure 2.2: Simplified schematic of a triple quadrupole mass spectrometer with an ion transfer capillary, conceptually based on the contents of the manual [20].

The mass analyzer region contains three quadrupoles with numerous lenses. Depending on the scanning mode, either Q1 or the third quadrupole Q3 can perform mass analysis. The second quadrupole Q2 is formed through an arc of 90° to decrease the noise level by only deflecting ions but not neutrals. The second quadrupole Q2 can be used as a collision cell for controlled fragmentation of the ions. In this thesis, the first quadrupoles act as ion transmission and focusing devices and the last quadrupole is the mass analyzer. This mode is denoted as Q3MS. The RF potentials of the Q3 quadrupole are ramped up with opposing phase and a DC offset voltage applied to each pair of rods for mass-dependent ion separation and oscillation. For ion transmission, no DC offset is applied. In contrast to the ion trap, the ions in the quadrupole are scanned in feed-through. The time required for mass detection on the quadrupole is called cycle time. As a consequence, selected ion monitoring (SIM) with a limited m/z range is faster on the TSQ, whereas full spectrum acquisition is carried out faster on the LCQ.

Finally, the ion detection system consist of a conversion dynode perpendicular to the ion pathway and an electron multiplier, known from the LCQ mass spectrometer.

2.1.3 Calibration Curves in Mass Spectrometry

In mass spectrometry, the ion intensity is given in arbitrary units. One method to link this ion signal to the known concentration of the analyte is to construct a calibration curve based on linear regression analysis. This curve does not only

calibrate the ion signal to the concentration of the analyte, but also provides its quantification limits. These limits state at which concentration an ion peak cannot be safely identified anymore. Therefore, this curve assesses the analytical performance and the instrumental response of the mass spectrometer, depending on the purity of an analyte as well as the complexity of the sample.

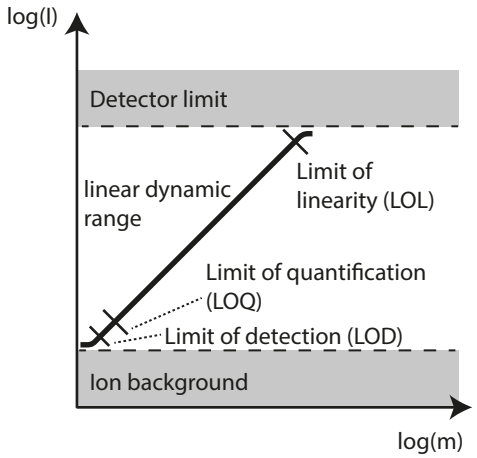

Figure 2.3: Sketch of a calibration curve.

In Figure 2.3, a calibration curve is sketched on a double-logarithmic scale of the ion signal I and the amount of the analyte m. The lower limit of the detectable ion intensity of an analyte is fixed by a constant ion background. An increase in the concentration of the analyte will also increase the ion signal. Close to the ion limit of the detector, a maximum signal is achieved. This limit depends on the injection time or the maximum amount of ions in the mass analyzer. The slope of the calibration curve yields the ratio of the instrumental response to the concentration of the analyte. As the relation is supposed to be linear, the slope gives the sensitivity of the method. The intercept with the ordinate describes a constant background signal.

The background ion signal is measured by an averaged ion intensity I with a standard deviation σ in an experiment without an analyte. The LOD is then calculated by the intercept of the calibration curve with the extracted ion signal of the background plus three standard deviations $I+3\sigma$. In contrast, the ion limit for the LOQ is taken as $I+10\sigma$. It is worth noting that this statistical approach assumes a Gaussian distribution of the background signal. The LOL is usually manually estimated at the point where the curve flattens. The limit of quantification (LOQ), slightly higher than the LOD, and the limit of linearity (LOL) define the linear dynamic range, in

which the calibration curve is measured.

2.2 Diode Lasers and Laser-Surface Interaction

Diode lasers are extensively used due to their low costs and easy-to-handle properties. A semiconductor diode is constructed by contacting two strongly doped semiconductor materials with opposing space charges (p-n junction). At the junction of the doped materials, a depletion region is formed by a gradient in the charge density, creating an electric field inside this region. From recombination of electron-hole pairs in the depletion region, light is emitted to the edge of the semiconductor. The emission wavelength correlates to the differences in the energy levels of the conduction and valence band, depending on the doping and the properties of the semiconductors themselves [21, 22]. Efficient blue lasers are constructed by combining a double hetero junction of Indium Gallium Nitride or Gallium(III)Nitride.

The refraction index of the semiconductor crystal is roughly tripled in comparison to the refractive index of air [23]. Therefore, the light is reflected on the edges of the semiconductor crystal and a resonator with an optical stationary wave is formed. The back facet of the resonator is coated to increase the reflectivity. Population inversion can be achieved by electronic pumping, providing coherent photons by induced emission of light.

Commercially available diode lasers have a spectral range from ultraviolet to infrared, with output powers from milli to kilo watts [18, 24–27]. The output power of a diode laser can be increased by stacking multiple emitters of the same laser diode. The working parameters for the output power of the diode are the injection current to the diode and temperature of the semiconductor material. While increasing one or both parameters, a shift in the dominant laser wavelength can be observed. This shift correlates to a change in the refractive index n as well as an expansion of the crystal with a length L. The constraint for the evolution of stationary waves with a wavelength λ inside the resonator is

$$nL = k\,\lambda/2, k \in \mathbb{N}.$$

The beam of the laser diverges on both the horizontal and the vertical axis. The vertical, greater spatially diverging axis is called “fast axis”, the less spatially

diverging, horizontal diverging axis “slow axis”. This terminology is visualized in Figure 2.4. The light is linearly polarized on the slow axis due to the dimensions of

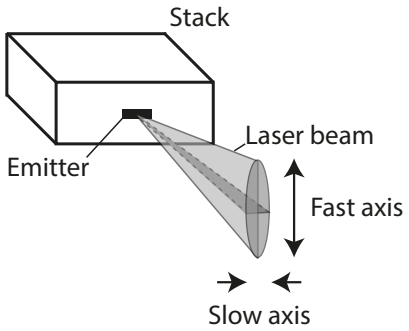

Figure 2.4: Simplified schematic of the slow and fast axis of a single emitter laser diode.

the emitter.

2.2.1 Laser-Surface Interaction

In this thesis, the laser is applied to a metal-isolator sandwich structure. By applying the laser to the surface, reflection and transmission of the laser light take place. The corresponding reflection coefficients R_s are well-described by Fresnel equations [28] and related to the transmission coefficients T_s by $T_s = 1 - R_s$.

For metals used throughout this thesis, the reflectivity is 50 % to 60 % at 450 nm [29]. The residual light is mostly absorbed on the surface, penetrating it about 10 nm to 20 nm [30]. Thermalization after laser application occurs within 10^{-12} s to 10^{-10} s [29]. The heat conduction is described by the conservation of energy and Fourier's law of thermal conduction. The lateral, thermal diffusion length l is given by

$$l \approx \sqrt{D\tau}.$$

$D = \frac{\lambda}{\rho c_p}$ is the thermal diffusion and τ is the laser dwell time [31]. The thermal conductivity λ, density ρ and specific heat capacity c_p are taken from Young and Sears [32], the National Center for Biotechnology Information [33] and Chase [34]. For a dwell time of 1 s to 30 s, the lateral diffusion length of Copper is 9 mm to 49 mm.

2.2.2 Laser-based Methods in Mass Spectrometry

In mass spectrometry, lasers are most frequently used for desorption and ionization of surface-adhered analytes, as in case of matrix-assisted laser desorption ionization (MALDI) [35]. To shield the analyte from direct laser application and hence fragmentation, the analyte is either doped with a thin crystalline layer called chemical matrix (matrix-assisted laser desorption ionization, MALDI) or nano particles (surface-assisted laser desorption ionization, SALDI). As SALDI branched from MALDI, both methods share a common basis, with one difference being the photosensitive dopant on the surface. In both methods, the dopant absorbs the laser, effectively resulting in heating the surface.

Both methods involve optical, mechanical, thermodynamic and physicochemical processes, with phase transitions [36]. Therefore, the desorption and ionization mechanisms are subject of current research, with multiple hypotheses proposed. All models are based upon the formation of ions via desolvation of the analyte from the matrix in different phases [37]. Depending on the complexity of a compound, the resulting mass spectrum may consist of several peaks.

The most valuable part of MALDI are the imaging capabilities. Commonly, the spatial distribution of the analyte is scanned with a focused laser beam. Each position on the cell or tissue is then mapped to the intensity of the ion signal in the mass spectrum. This enables analysis of single cells in micrometer range with parts per billion concentration [38–40]. SALDI is capable of performing imaging as well, but is often combined with a chemical matrix.

Ion-neutral-ratios yield around 10^{-5} for MALDI, demanding to increase the efficiency of ionization [41]. Commonly, an external potential is required for ion funneling to increase the ion yield [42]. Despite this tuning, one approach is to use a second laser for ionization of the desorbate. This method is named MALDI-2 [43]. The authors perform imaging in transmission-mode-geometry (t-MALDI-MS), mounting a microscope objective to the uncoated glass side of the substrate. By resonant two-photon absorption of the matrix, the ion yield is increased. However, the complexity of sample preparation and vacuum working conditions in MALDI still remain. Therefore, other ion generation methods and ambient (air) mass spectrometry (AIMS) came into focus in the past decade. One of such a method couples a plasma with the laser in mass-spectrometry for ionization after laser desorption.

2.3 Plasma-based Ionization in Mass Spectrometry

Formally, plasmas are described as a quasi-neutral, (partly) ionized gas of charged and uncharged particles that are dominated by electrostatic interaction of the particles and show collective behavior. Notably, not all discharges called plasma meet the aforementioned criteria. For instance, atmospheric plasmas are collisional driven due to the decreased mean free path of the particles, thus not matching the definition. Also, several parameters required for the criteria validation such as the electron density or the electron temperature require a valid model, linked to profound knowledge of the given discharge to validate the assumptions made. This complicates a proper plasma description.

There are inductively, capacitively or dielectrically coupled plasmas with different characteristics [44–46]. Dielectric barrier discharges (DBDs) are preferably used in mass spectrometry for several reasons. Constricted breakdowns to the inlet are reduced with these discharges, which allow them to be placed in front of the inlet of the mass spectrometer. Also, the energy transfer to the analyte decreases, making the ionization method less fragmentary (softer) and hence suitable for the analysis of molecules.

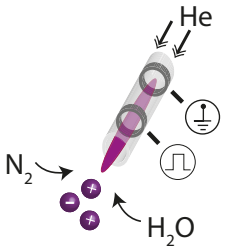

Figure 2.5: A dielectric barrier discharge (DBD) with two ring electrodes attached to the glass capillary. Helium is used as a carrier gas, nitrogen and water enter the capillary as impurities from the ambient air.

A dielectric barrier discharge (DBD) is a plasma inside a glass capillary, which is surrounded by two ring electodes. This is shown in Figure 2.5. The discharge is ignited by applying a square-wave voltage in multiples of 1000 V directly to one electrode, depending on the discharge dimensions. The applied frequencies range from very low frequencies (VLF) of 3 kHz to 30 kHz. The glass polarizes in accordance with the changing polarity of the externally applied, electric field. Inside the gas volume, the amplitude of the electric field is inversely proportional to the dielectric constant. The breakdown voltage, the voltage required for the ignition of

the plasma, can be derived by Paschen's law [13], and is linked to the ionization degree of the discharge. After the initial breakdown between the galvanically isolated, metal electrodes, the discharge is driven by a conductive channel. This generates a current with the polarity of the externally applied, electric field.

Noble gases such as Argon or Helium are usually used as carrier gases. These gases are chemically inert and are used to investigate the physical mechanisms in plasmas. However, air impurities such as nitrogen or water enter the capillary from the orifice of the capillary and the gas tank itself. These impurities play a key role in the plasma formation, as will be outlined in the following. The ionization process after reaching the breakdown of the discharge begins with electron collisions that form excited species such as metastables. By further collisions, more previously neutral atoms and molecules become ionized, if the energy transferred is above ionization level. In a simplistic image, Helium-driven DBDs are sustained by step-wise ionization of nitrogen molecules $N_2{}^+$ from Helium metastables and electron collision. From a reaction cascade, protonated water clusters H_2O^+ are formed.

The gas density at atmospheric pressure facilitates the formation of electrons that subsequently create an electric field comparably high to the external electric field. Hence, the discharge is driven by the charge carriers themselves and becomes self-sustainable. The electric field of the plasma is subsequently reduced by ion deposition on the glass.

The propagation of the charge carriers between the electrodes is called a positive or a negative streamer, depending on the direction of the electron and the ion avalanche movement. These streamers play an important role in the soft ionization process.

Klute *et al.* [47] and Schütz *et al.* [48] worked on the applicability of DBDs as a soft ionization tool for molecules in mass spectrometry, the DBDI. In a DBDI, there are multiple successive discharges, such as the early plasma and the coincident plasma. These plasmas occur on different time scales. The early plasma is driven by the displacement current, causing the propagation of a positive streamer. Due to their mass, ions are less mobile than electrons and fall behind within the propagation of the streamer. The electric field changes direction as soon as the electrons are drained by the electrode, leaving the coincidence plasma and a plasma current. The authors have proven that the coincident plasma can cause fragmentation and dissociation of an analyte. An adjustment of the duty cycle can help to suppress such coincident plasmas in Helium entirely. Hence, only the early plasma and

a homogeneous plasma jet remain. For Argon driven plasmas, Schütz *et al.* [49] presented a mixture of Argon and Propane that helped to avoid streamers and fragmentation. The inherent mechanism relates to penning ionization of propane molecules by argon metastables.

Despite the DBDI, there are several other electrode configurations of DBDs found in literature. Some of these are shown in Figure 2.6.

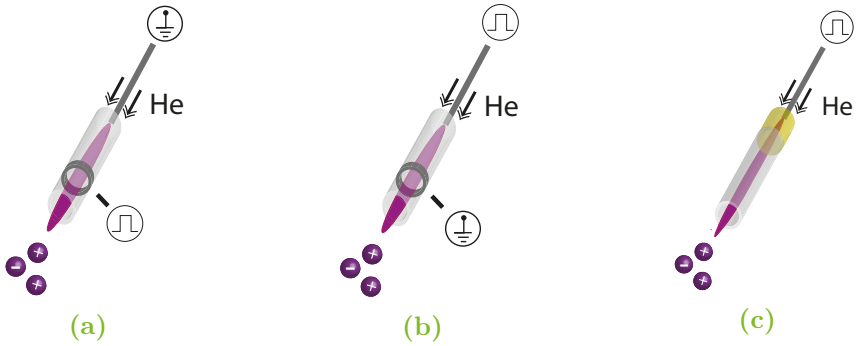

Figure 2.6: Common electrode configurations of capillary DBDs. Figure 2.6a low temperature-plasma (LTP), Figure 2.6b inverse low temperature-plasma (iLTP) and Figure 2.6c flexible microtube plasma (FμTP).

Such an electrode configuration is called low temperature plasma (LTP, Figure 2.6a). The term refers to the lower gas temperatures of the plasma, which enable analysis of molecules [50, 51]. However, the lower gas temperature also applies to DBDs. In fact, the gas temperature is a parameter controlled by others, such as geometry, dissipated power or frequency. Nevertheless, a difference between the DBDI and the LTP is the electrode configuration. The LTP consists of a pin electrode that is surrounded by the glass capillary, and a grounded ring electrode attached to the outside of the orifice of the capillary. In an inverse low temperature-plasma (iLTP), the high voltage pin electrode and ground electodes are permuted, as shown in Figure 2.6b.

A flexible, look-alike iLTP without physically grounded electrode was recently designed by Brandt *et al.* [17] and named flexible microtube plasma (FμTP). The FμTP is shown in Figure 2.6c. In contrast to the DBDI, no duty cycle intervention or gas manipulation is needed for soft ionization. The FμTP consists of a wire put on high voltage inside a 250 µm coated, fused glass capillary. With the robust, compact and flexible design of the FμTP, it is well suited for miniaturized arrangements.

3 Apparatus of Laser Desorption, Plasma Ionization and Mass Spectrometry

As stated in the fundamentals, a laser is coupled with a plasma to increase the desorption and ionization efficiency in mass spectrometry. This chapter will describe the apparatus used for this method. First, different setups of the method will be presented. Second, the details of the required tools will be described. A short section outlining the preparation of the analytical compounds and the biological samples will finish this chapter.

3.1 Experimental Setups

The setup shown in Figure 3.1 will be initially used for laser desorption and plasma ionization in mass spectrometry. For laser desorption, a blue diode laser is used. The emitted beam is guided through a mechanical shutter (shutter: *SH05*, Controller: *SC10*, both *Thorlabs*, USA) and a beam splitter. It is focused on a surface using a 5× magnifying, plan-achromatic objective (*Plan5x/0.11*, *Kern*, Germany) mounted on a revolver. Both optical components are dismounted from a microscope (*OKM173*, *Kern*, Germany). The surface-reflected light is transmitted through the beam splitter on a camera (*UK-1158*, *ABS-Jena*, Germany).

The substrate is mounted horizontally, centered below the inlet of the mass spectrometer, with the laser focused to the substrate. It is moved on the indicated axes using an electrical stage (*T-LS28M*, *Zaber Technologies*, Canada). The desorption substrate consists of a metal-isolator sandwich structure and defined cavities for the droplet deposition of the analytical standards. The analyte droplet is placed inside the cavity and centralized on-axis of the MS with the electronic stage and the camera. However, only a single cavity line of the substrate can be analyzed at once due to limited space in front of the inlet of the mass spectrometer. Therefore,

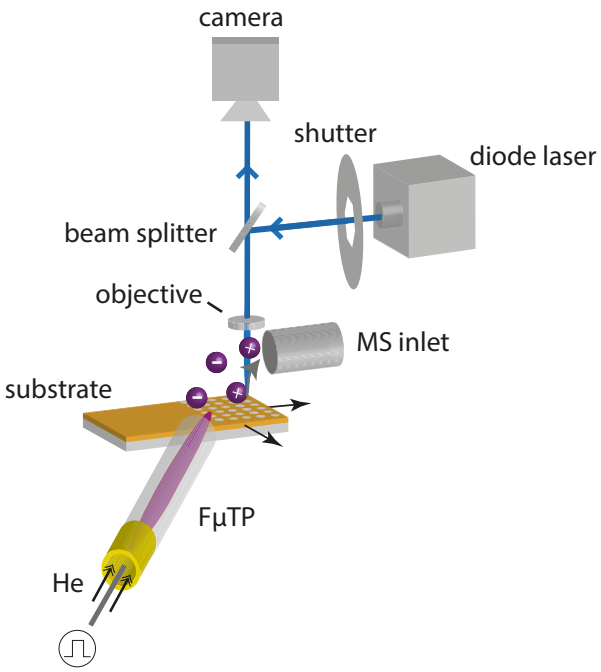

Figure 3.1: Initial experimental setup for laser desorption and plasma ionization in mass spectrometry for the initial studies (chapter 4).

the substrate is cut with a wafer saw after each experiment to solve this issue. The FμTP is placed in a 45° angle to the MS axis above the substrate.

An improved experimental design allows full screening of the substrate without the need to cut it, as it is vertically mounted. The corresponding experimental setup is shown in Figure 3.2. The laser rail with the laser, shutter, beam splitter and

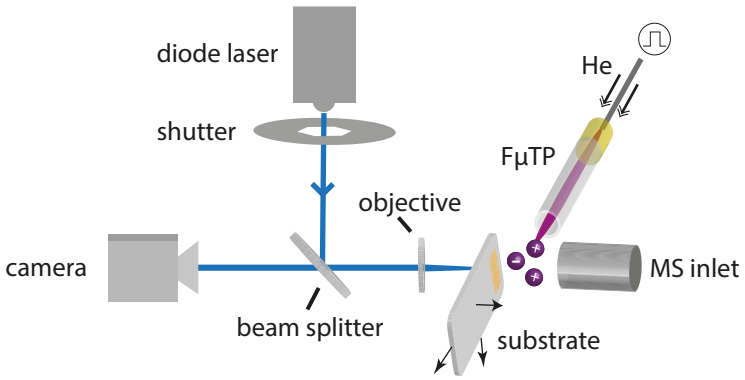

Figure 3.2: Improved experimental setup for laser desorption and plasma ionization in mass spectrometry (chapters 5 to 7) [52, 53].

camera can be mounted on both home-built setups. In contrast to the initial setup, the laser is mounted in a transmission geometry on-axis to the inlet of the mass

spectrometer. With this setup, the substrate and the FμTP can be placed closer to the inlet of the mass spectrometer as well. The FμTP is positioned in a 90° angle to the inlet of the mass spectrometer, parallel to the substrate. Depending on the application, a 40x magnifying objective (LPL 40x / 0.65, *OKM173*, *Kern*, Germany) may be used for laser focusing. The change of the objective will be indicated in the respective chapters.

3.2 Mass Spectrometer

For ion detection, the LCQ (*LCQ Deca XP*, *Thermo Fisher Scientific*, USA) mass spectrometer is used. The mass range of the MS spans from $\delta m/z$ 50 - 4000. Commonly, a full scan acquisition is performed with $\delta m/z$ 100 - 1000. The automatic gain control (AGC) is fixed at a maximum number of ions of 5×10^7. The cut-off injection time, the maximum time period if the number of ions injected into the ion trap and as selected in AGC is not reached, is usually kept at 20 ms to 30 ms. Selected ion monitoring (SIM) is performed as well. For mass calibration, a nanoelectrospray ionization source with a calibration mix solution is used. Working parameters for the mass spectrometer are summarized in Table A.1 of the appendix. For data processing, *Xcalibur* software is used (*Xcalibur version 2.0, Thermo Fisher Scientific*, USA).

For imaging applications, the LCQ Paul ion trap can be used as well. However, triple quadrupole mass spectrometers without the ion trap offer higher sampling rates in SIM. Therefore, the triple quadrupole mass spectrometer (*TSQ Vantage, Thermo Fisher Scientific*, USA) is chosen. SIM is carried out with a sampling rate of 60 Hz and a cycle time of 10 ms on the third quadrupole (Q3MS). The mass range in this mode is $\delta m/z$ 1.5. The mass and resolution calibration is performed with a commercial available calibration solution (*PierceTM Triple Quadrupole Calibration Solution, number 88325, Thermo Fisher Scientific*, USA). The mass accuracy of both MS is $\Delta m/z$ 0.5. The parameters used for the TSQ are summarized in Table A.2 of the appendix.

A data acquisition (DAQ) interface (*USB-6341 BNC DAQ, National Instruments*, USA) is used to translate analogous signals from the shutter, stage and the MS to the controlling software. Neither the ion trap, nor the quadrupoles can be triggered. However, a start pulse can be sent to both MS, which initiates a measurement.

This is realized by a signal of the DAQ interface to the start-in socket of the mass spectrometer (5 V, 16 mA over a 390 Ω resistor to an opto-isolator, Type *SFH601-2*, *Mouser Electronics*, Germany). By default, the MS sets a TTL signal to the start-in socket. If this pin is electronically pulled down to mass, the MS begins with the measurement for a user-defined time interval.

3.3 Diode Laser

The blue laser diode (*LDM-450-1600-C* or *LDM-448-3500-C*, both *Lasertack GmbH*, Germany, Controller: *ITC540*, formerly *Profile*, Germany) is a 450 nm continuous emitting, multimode diode. It is a horizontally, triple-stacked diode with a maximum output power of 1.6 W. The beam divergence is 0.8 mrad. The slow axis diverges with typically 7°, the fast axis with 23° [54]. A more intense blue laser diode (*LDM-448-3500-C*, *Lasertack GmbH*, Germany) [55] at 448 nm is employed to achieve higher laser intensities. It achieves a maximum output power of 3.5 W and a beam divergence of 1.2 mrad. The slow axis of the more intense blue diode diverges with 14°, the fast axis with 46°. Both laser beams are collimated with a *M9x0.5* collimation lens after the horizontally-oriented, stacked emitters. The orientation of the emitters of the laser diodes relate to the incident angle of the laser light to the optics, as it must match to the Brewster angle. The slow axis is expanded using an anamorphotic prism pair and matched to the divergence of the fast axis. The slow axis is linearly polarized. The collimated laser beam is focused to a surface. Images of the laser spot will be shown in chapter 4 and chapter 6.

The laser beam profile is a quality factor of a laser. In this sense, the laser beam profile is measured by the voltage amplitude U of a photo diode and the distance d. The slow and fast axes of the unfocused 1.6 W blue diode lasers are shown in Figure 3.3. A home-made Galilean telescope is used to expand the beam. A super position of Gaussian-like beam profiles is observed on the fast axis, which emerge from the stacking of the three emitters. The highlighted distances between the maxima in the profile equal the distances between the emitters whose laser beam is expanded. In theory, the beam profile along the slow axis on a single emitter should be Gaussian. Practically, a super position of Gaussian-like profiles is observed as well. This effect relates to the anamorphotic prism pair, which expands the slow axis. Also, errors from offsets between the emitters propagate in beam expansion. This further causes the flanks of the profile to appear flattened. As a consequence

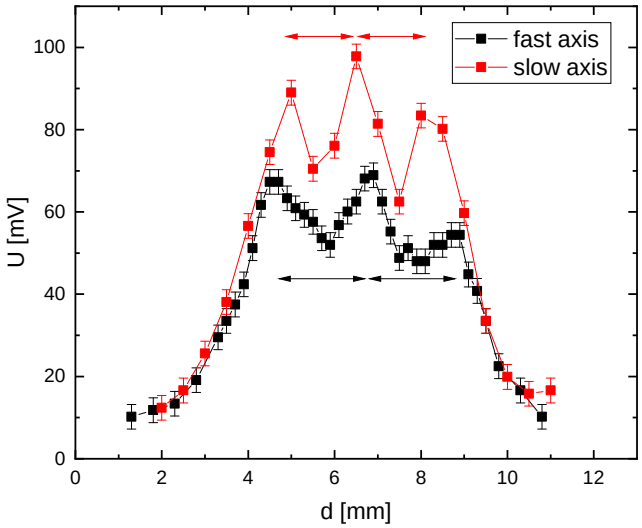

Figure 3.3: Slow and fast axis of the 1.6 W blue diode laser measured with a digital phosphor oscilloscope (*DPO2012*, *Tektronix*, USA). Focal lengths of the concave L_1 and convex lens L_2 are $f_{L1} = 100\,\text{mm}$ and $f_{L2} = 30\,\text{mm}$. Besides, a 150 µm aperture as well as a silicon photo diode are used.

of these effects, the distance between the maxima on the slow axis is smaller than the distance of the maxima on the fast axis. The temperature of the materials of the diodes is constantly held at 20 °C using a Peltier element. The properties of the diode lasers are summarized in Table 3.1.

Table 3.1: Diode lasers used with dominant wavelength λ_0, maximum output power P_{max}, slow and fast axis (S./F.A.) and beam divergence (BD).

λ_0 / nm	P_{max} / W	S.A. / °	F.A. / °	BD / mrad
450	1.6	7	23	0.8
448	3.5	14	46	1.2

For comparison of the blue to an infrared laser, a continuous wave infrared diode laser (*OTF 30P-40*, formerly *Optotools GmbH*, Germany [56]) is presented. It is set at a dominant wavelength of 808 nm and a maximum output power of 16 W through a supplied 400 µm optical fiber (fiber connector, Type *SMA 905*, *Thorlabs*, USA). Its numerical aperture is 0.22.

In chapter 6, a waveform generator (*HM8150, Rohde & Schwarz Value Instruments, formerly Hameg*, Germany) is used to externally pulse the diode laser with a user-defined pulse frequency and pulse width. The waveform generator offers a rise time of 8 ns, whereas the diode laser controller supplies a rise time of $(15 \pm 3)\,\mu\text{s}$. The

electronic stage is remotely controlled using the RS-232 protocol and LabVIEW-based software by the manufacturer (version 1.4.0, *Zaber Technologies*, Canada).

The laser pulses are measured with a silicon photo diode and a house-made amplifier coupled with an oscilloscope (*DPO2012, Tektronix*, USA). The pulses are attenuated by 99.7 % using neutral density filters in a wheel attenuator (*10CWA168, Standa*, Lithuania).

3.4 Plasma Ionization Source

The DBDI [16] is used as an ionization source within the initial studies. The FμTP was developed by Brandt *et al.* [17, 57] and is not only smaller, but flexible and designed with a single high voltage electrode far away from the inlet of the mass spectrometer. The DBDI is easy to construct by attaching two ring electrodes to a glass capillary with a gas supply. In contrast, the FμTP is more complex to build.

The FμTP uses a tungsten pin electrode of 100 µm diameter, which is put on high voltage. The pin electrode is surrounded by a coated fused silica glass capillary with an inner diameter of 250 µm and an outer diameter of 350 µm. While the inside of the capillary is plain glass, the outside is coated with polyimide, making the glass more flexible. The glass capillary is further shielded by a polytetrafluoroethylene (PTFE), fluorethylenpropylen (FEP) tube.

The FμTP is attached to a mass flow controller using a polyetheretherketone (PEEK) T-piece with two banjo screws and polymer fittings (*Type P728* and *Type F300*, both *Chromatographie Service GmbH*, Germany). Two sleeves are used for sealing the plasma air-tight (*Type F237* and *Type F242*, both *Chromatographie Service GmbH*, Germany).

An uncoated glass tip of 5 mm to 10 mm is attached to the end of the electrode of the FμTP. The discharge ignites from the end of the electrode to the orifice of the attached, uncoated glass capillary. The complete FμTP is 570 mm long. The ion source is mounted with a 3D-printed holder (black polylactic acid filament, *EaseFil PLA, Formfutura B.V.*, The Netherlands).

The conditional parameters of both ion sources are summarized in Table 3.2. Helium with a purity of 99.999 % is used as a carrier gas for both ionization sources. The gas is injected using a mass flow controller (*AnalytMTC*, Germany) with a maximum

Table 3.2: Operating voltage U, Helium gas flows ϕ_{He}, generator frequencies f and inner diameter of the DBDI and the FμTP.

Ion source	U / kV	ϕ_{He}	f / kHz	Inner diameter / μm
DBDI	3.5	(400 ± 40) sccm	20	1000
		(200 ± 20) mL/min		
FμTP	1.8 ± 0.4	(40 ± 5) sccm	20	250
		(20 ± 2) mL/min		

flow of 500 sccm. The DBDI uses a gas flow of (400 ± 40) sccm, which equals (200 ± 20) ml/min. In contrast, the reported gas flow of the FμTP ranges from 4 sccm to 150 sccm or 2 ml/min to 75 ml/min due to the decreased inner diameter [17]. A gas flow of (40 ± 5) sccm or (20 ± 2) ml/min is used for this FμTP.

A home-built square wave voltage generator is used for the voltage generation. The DBDI needs 3.5 kV of operating voltage, whereas a voltage amplitude of 1.8 kV is required for the FμTP. A lower voltage is required for the ignition of the FμTP due to the decreased discharge dimensions. The voltage amplitude required for the FμTP increases with wear of the coated capillary due to increasing gas diffusion of the ambient air into the capillary. Therefore, the applied voltages vary for the FμTP. Both plasmas are operated at a frequency of 20 kHz. The applied voltage and the gas flow are correlated the plasma discharge length for both sources [58].

3.5 Chemicals and Sample Preparation

All chemicals used in chapter 5 have pro analysi purity. The chemicals and their solvents are listed in Table A.3 of the appendix. All solutions are prepared in high concentration (c = 1 g/l to 10 g/l), are vortexed and diluted subsequently. The solutions are kept at −30 °C until analysis.

In chapter 6, animal tissue of mice is used. Housing temperatures of the mice (*FVB mouse, Janvier Labs*, France) are (22 ± 2) °C with (55 ± 10) % humidity and a 12/12 hours light/dark cycle. Chow and water are offered ad libitum. Mouse liver, kidney and brain are flash-frozen in liquid nitrogen and stored at −80 °C. The organs are heated to −20 °C for two hours before sample preparation. Section medium (*NEG 50, Thermo Scientific Richard-Allan Scientific*, USA) is used to mount the sample on a plate and the plate with the medium is frozen at −60 °C for 10 minutes. The tissue is cut at a thickness of (10.0 ± 0.5) μm at −20 °C using a cryomicrotome

cutter (*CryoStar NX70, Thermo Fisher Scientific*, USA). These microtome cuts are applied to the desorption substrate. A vacuum desiccator (*Concentrator Plus, Eppendorf*, Germany) is used for approximately 2 min to heat the tissue to room temperature and avoid formation of water on the tissue.

4 Study on Laser Desorption of Analytical Standards

In 2013, Gilbert-López *et al.* [18] reported on the coupling of a continuous wave (cw), near-infrared diode laser to a dielectric barrier discharge that were used for the analysis of non-volatile chemicals in mass spectrometry. Laser desorption was carried out on black-ink dotted glass substrates that absorbed the laser light and caused surface heating. Those results were compared to substrate heating using thermal couples and showed not only an increase in ion yield, but also less fragmentation. As desorption and ionization can be separated, an ambient air ionization source was introduced. Despite the aforementioned results, the authors outlined several difficulties with their experimental setup. They state that their substrate is not optimal for desorption, as the desorbed area is a factor of 6.25 smaller than the dried sample spot. Further, the dried ink spot depends on the manufacturers ink composition, such as used solvents. Also, the sample spot distribution depends on the drying process of the liquid sample, such as the coffee ring effect.

This was the starting point for a systematic study of this thesis, which aims at two main issues. First, the study focuses on reproducible laser-surface interaction with an efficient desorption from the constructed surface. Second, the surface must limit the droplet propagation in a way that the desorbed area matches the dried sample spot. As a result, drying characteristics can be neglected. In conclusion, the shared goal is to improve analytical performance for a broad range of analytes.

4.1 Surface Material Studies and Substrate Production

The initial, preliminary studies of this thesis are performed on a set of materials with a continuous wave, blue diode laser and the same DBDI [58] used by Gilbert-López *et al.* [18]. In general, the laser is used for thermal desorption and the plasma for

ionization of the desorbate. In this sense, a laser application to the surface does not provide an ion signal. On the other hand, the ionization source without the laser does not desorb the compound.

Cholesterol is selected as a model compound, as it is structurally stable without chemical buffer. The compound is placed on different surfaces, such as metals, isolators, semiconductors and mixed structures. These are listed in Table 4.1.

Table 4.1: Materials used for the study. The italic-written structures are not providing a stable signal. The bold-written structure is chosen for laser desorption and plasma ionization in mass spectrometry.

Material	Signal? (y) / (n)
Metal blocks	
Copper	(n)
Semiconductors	
Silicon	(n)
Silicon dioxide	(n)
Isolators	
Glass	(n)
Rugged glass	(y)
Polymers	(y)
Sandwich Structures	
Gold-PMMA	(y)
Copper-PMMA	(y)
Copper-ceramic	(y)
Chromium-brass	(n)
Copper-brass	(n)
Gold-glass	(y)
Copper-glass	(y)
Chromium-glass	(y)
Chromium-oxide-glass	(y)
Copper-Chromium-glass	(y)

As a first result, blocks of metals, semiconductors and transparent isolators are not able to trigger thermal desorption. However, this does not apply to mixed structures such as metal and glass. This observation fits to the results by Gilbert-López *et al.* [18] in which a mixed structure of ink dotted on glass was presented. A reasonable hypothesis of these results is that two layers with different heat transfer coefficients are needed for laser desorption. The first layer hit by the laser needs to absorb the laser and needs to be as thermally stable as possible to keep structural integrity. The second layer needs to be thermally isolating to trap the heat on the first layer. The latter hypothesis is justified by the observation that metal blocks such as Copper

do not trigger desorption, probably by a rapid heat distribution inside the block. In other words, a possible way to increase the desorption efficiency is to use a sandwich structure of thermally conductive and non-conductive materials with different heat transfer coefficients. In this sense, two layers of just metals or isolators such as Copper-brass or different stacked polymers are not feasible for desorption.

Different metals such as Gold, Chromium oxide or Copper are candidates for the first layer. Basically, the key element is the efficient absorption of the laser light by the surface. For mass production, Copper is the metal of choice. The other metals are either more expensive or, as in case of Chromium oxide, more complex to construct as different oxides are present on the surface, decreasing the reproducibility of the layer. Also, some of these oxides such as Chromium trioxide are hazardous [33]. The choice of the second layer is also not straight forward. While polymers are generally not a good choice in mass spectrometry due to a higher ion background, ceramics and glass are promising candidates for the second layer. Conventional microscope slides are made of borosilicate glass and are thus well-suited for biomedical research. Also, glass is known to show interesting properties at high surface temperatures [59]. In this sense, the softening point of glass will play a crucial role to evaluate the surface modifications after laser application, which will be addressed in detail in the next section. The metal layer must be significantly thinner than the insulating layer to efficiently trap the heat. In this sense, several hundred nanometers are sufficient for laser desorption. For comparison, conventional microscope slides are approximately 1 mm thick, yielding $d_{\text{metal}} \ll d_{\text{glass}}$.

There is one more property of the substrate that has not been discussed, yet. In the article by Gilbert-López *et al.* [18], the sample is placed on the plain glass. The sample volume spreads on the glass, which reduces the reproducibility of the results. One solution to this issue is the construction of cavities similar to well plates, which will confine the sample spread. For the construction of the cavities, photo-resistive coating is used. The smallest surface-to-volume ratio of the sample droplet is achieved using commercial hydrophobic chemicals, which will reduce the impact of the coffee ring effect.

The following paragraph will deal with the details of the construction of the substrate. These steps are summarized in Figure 4.1 and will be discussed in the upcoming paragraphs. The lithography process is split into three steps: First, the surface preparation, then the application of the coating and third stabilizing the coating by

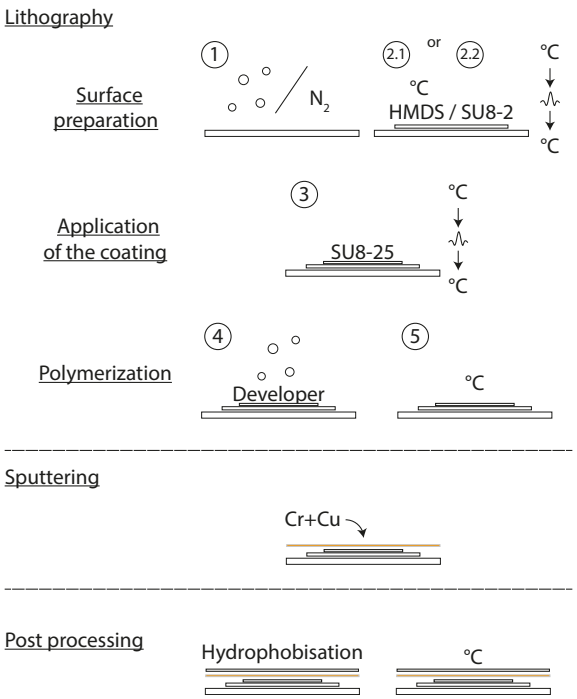

Figure 4.1: Schematic of the substrate preparation. The different steps are discussed in the text.

polymerization. A substrate-matched holder is needed to avoid pile up of the coating on the edges of the substrate. This pile up would cause inefficient polymerization. Other important experimental parameters are the angular acceleration in spin coating as well as the cool down time of the slides to avoid flaws in the coating. The angular acceleration in spin coating depends on the viscosity and thus the degradation of the resist. These parameters are summarized in Table A.4 of the appendix [60].

Plain microscope glass slides (45 % rounded edges, 26 mm×76 mm×1 mm) are cleaned with peroxymonosulfuric acid and dried with nitrogen. An adhesive layer of either Hexamethyldisilazan (HMDS) or a negative tone photo-resist (*SU8-2*, *Kayakuam Advanced Materials*, formally *MicroChem*, USA) is placed on the microscope slides, which improves the stability of the next layers. In the case of HMDS, the substrate is pre-heated and put in a closed chamber with a gaseous mixture of nitrogen and HMDS. In the latter case, the resist is applied via spin coating (*Polos, Semiconductor Production Systems Europe*, United Kingdom). After application of the coating, three standardized sub steps are required: Soft baking, light exposure and post exposure baking. The underlying concept is that the illuminated part will

polymerize, whereas the residual resist is removed by organic solvents. The resist includes a light-sensitive salt, which emits an acid by light exposure and causes cross-linking of the coating. In total, this layer is 1.5 µm to 2 µm thick.

A second structural layer is used to form cavities. These cavities are built for controlled droplet deposition. Therefore, another negative tone photo-resist (*SU8-25*, *Kayakuam Advanced Materials*, formally *MicroChem*, USA) is used, following a similar recipe of application. Again, three sub steps are required after the application of the varnish via spin coating. First, the microscope slide is soft baked. After cool down, the microscope slide is fixed on a chuck in a mask aligner (*MA6*, *SÜSS MicroTec*, Germany). A mask is used in hard contact to cover the regions for the cavities on the microscope slide. This mask includes a Chromium layer of 7×7 circular cavities with an 1 mm inner diameter and a 2.25 mm center to center gap. Second, the substrate is exposed to light ($\lambda = 365$ nm, using a Mercury-vapor lamp with a band-elimination filter). Third, the structural layer is strengthened using a post exposure baking, which triggers complete polymerization. The substrate is subsequently bathed to develop the structure, rinsed and hard baked with a temperature gradient. The height of the layer on the substrate is (23 ± 2) µm.

The generation of thin metal layers is achieved by sputtering metal atoms from a target. Briefly, energetic noble gas ions are fired at a solid plate, which ablates metal atoms from the solid plate to the gas phase. To form a sandwich-structure, Copper is sputtered (*LS500*, *Von Ardenne*, Germany) on the glass surface, with Chromium serving as an adhesion agent to increase layer adhesion [60]. The substrate is sputtered with Chromium and Copper with the parameters listed in Table A.4 of the appendix [60]. As a result, 20 nm of Chromium and 200 nm of Copper are added to the glass. The reason for the order of the coating and metal layers is that the Copper and Chromium protect the sensitive coating and reduce the ion background to the mass spectrometer.

In post processing, a hydrophobic layer of fluorinated orthosilic acid (*HP310*, *SurA Chemicals*, Germany) [60] is added. The final substrate is heated at 160 °C for another two hours. The final substrate design is shown in Figure 4.2.

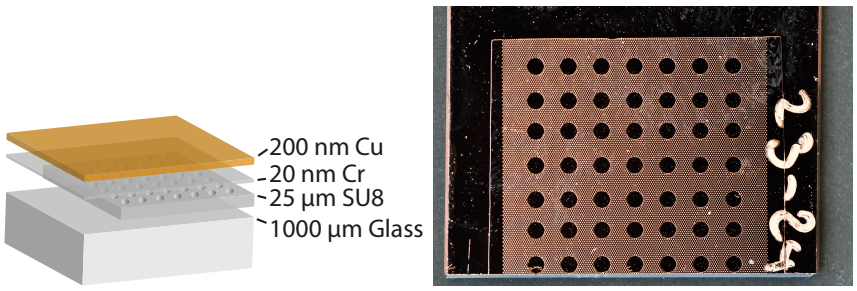

(a) (b)

Figure 4.2: Final substrate design. Figure 4.2a sketch and Figure 4.2b image of the desorption substrate. The thickness of each layer is not scaled to exact values.

4.2 Derivation of the Laser Intensity using different Spot Areas

The intensity of the laser light is the most important parameter to quantize the energy transferred to the surface. It is defined by the laser power applied to a fixed area. Thus, the current of the diode laser is firstly translated into the laser power. A 5× magnifying objective is used for the blue diode laser, while a 20× magnifying objective is used for the infrared laser to focus the laser beam efficiently. However, as the power meter is slightly off-focus to the optics, the laser power difference caused by the different objectives is neglectable.

In Figure 4.3, the calibration curve from the diode laser current to the laser power through optics is shown for both blue and the infrared diode lasers. Approximately 1 A is required for the blue diode laser to achieve a laser power of 550 mW. In contrast, a diode current of >30 A would be required for the IR diode laser to achieve the same laser power as the blue diodes. In conclusion, the blue diode laser is beneficial over the IR diode laser, especially combined with an absorptive Copper surface [61]. The second parameter required to calculate the laser intensity is the laser spot size.

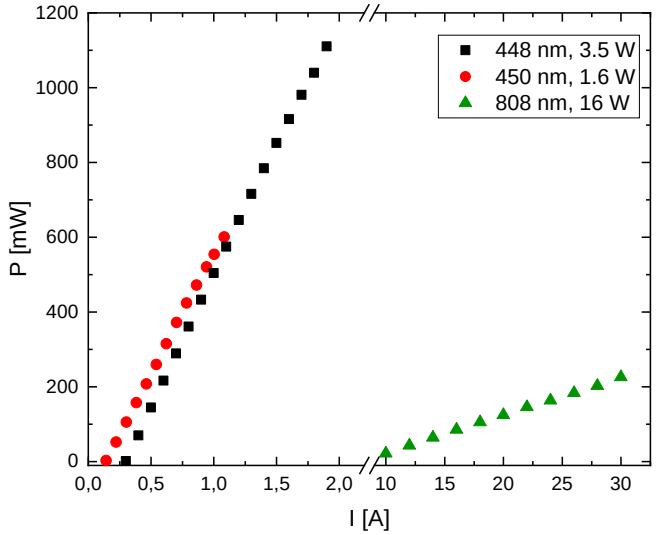

Figure 4.3: Calibration curves of the diode laser current to the laser power of two blue diodes ($\lambda_0 = 450\,\text{nm}$, $\lambda_0 = 448\,\text{nm}$) and an infrared diode ($\lambda_0 = 808\,\text{nm}$), all operated in continuous-wave mode. [60] Gauge: *LMP2*, power meter: *FieldMaster GS*, both by *Coherent*, USA

4.2.1 Laser Intensity using the Laser Spot Area

The spot size is measured with a CCD camera. In Figure 4.4, focused laser spots

(a) **(b)**

Figure 4.4: Spots of the focused laser beam. Figure 4.4a shows the spot of the ($\lambda_0 = 450\,\text{nm}$, $P = 1.6\,\text{W}$) diode [60] and Figure 4.4b the spot of the ($\lambda_0 = 448\,\text{nm}$, $P = 3.5\,\text{W}$) diode laser [52]. CCD Camera: 1/3 in *S/W A1-Pro*, *Conrad Electronics*, Germany

of both blue diodes are shown. Five neutral density filters (*NG9*, thickness 2 mm, *Schott AG*, Germany) are stacked, each filtering 98.1 % of the emitted light. A chip with a format of 1/3 in is 6 mm long on the diagonal and includes 510 Px×492 Px (PAL encoding system) on this chip. The size of a pixel is thus given by the edge length divided by the amount of pixels on the corresponding axis. Thus, a single quadratic pixel equals approximately 8 µm per side. For the 1.6 W diode, the spot

size is about 56 µm × 32 µm, whereas the laser spot size of the 3.5 W diode laser is about 128 µm × 32 µm.

On basis of these results, the laser intensity can be calculated. For cw diode lasers, the terminology of laser fluence and laser intensity I_L are often equally used. I_L is a working parameter, which depends on the laser irradiation power P_L and the area of the focused laser beam spot A_s. The average laser intensity can be estimated with

$$I_L = \frac{P_L}{A_s} = \frac{P_L}{\pi\,(d_a/2) \times (d_b/2)}$$

with d_i being the length of the axes a and b of the ellipse.

Therefore, I_L yields

$$I_{L,i} = \begin{cases} 459\,\mathrm{W/mm^2} \text{ for } i = 1.6\,\mathrm{W} \\ 348\,\mathrm{W/mm^2} \text{ for } i = 3.5\,\mathrm{W} \end{cases}$$

On basis of this calculation, the laser intensities of both diodes are similar, as the spot of the high-power diode laser is bigger, which is squared within the calculation.

4.2.2 Laser Intensity using the Desorption Area

In terms of laser desorption, the desorption diameter on a surface is usually taken for the laser intensity estimation [18]. The desorption diameter is the region in which the laser application can be verified. This diameter is larger than the laser spot. This effect origins from the heat conduction on the surface which causes an offset between the laser spot measured with a CCD and the desorption diameter. Therefore, the laser spot is technically not a parameter feasible in analytical means. More precisely, the laser intensity should be considered in a time-balanced frame including the inherent thermal processes. In this sense, it should be comparable to the experiments time scale to properly portray its mechanisms. This is especially important with respect to imaging applications and thermally-conductive tissue, as the thermal drift on the animal tissue would result in undersized spatial resolution. It is important to highlight that these assumptions are only valid within the analytical application. Therefore, this intensity will be considered as desorption laser intensity ψ throughout this thesis to separate it from the laser intensity on the surface.

In Figure 4.5, the cavities with different applied experimental laser powers P_L are shown in which the transition from a solid to a molten Copper surface can be confirmed visually. In Figure 4.5a, a blank surface is shown. From Figure 4.5b

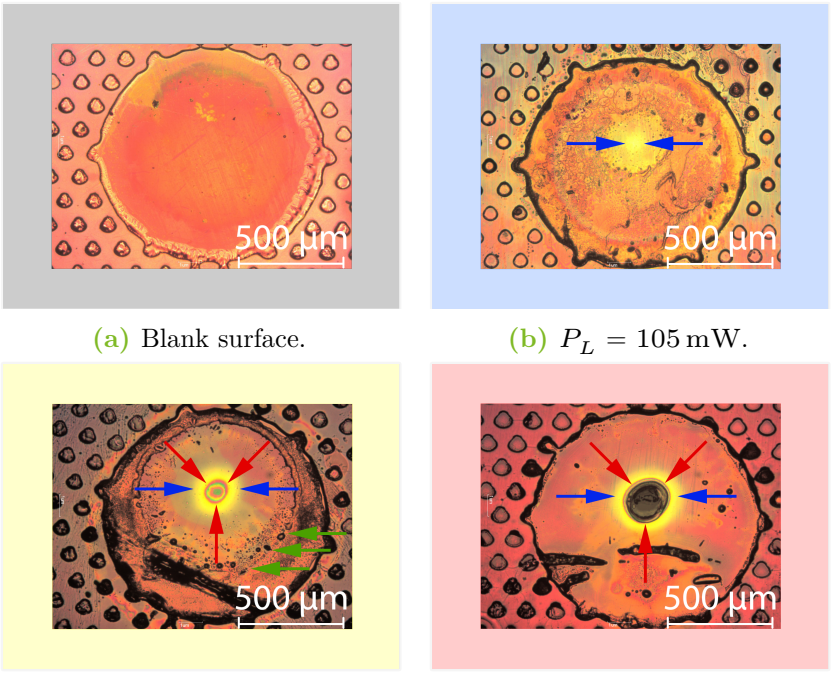

(a) Blank surface.

(b) $P_L = 105\,\mathrm{mW}$.

(c) $P_L = 234\,\mathrm{mW}$.

(d) $P_L = 492\,\mathrm{mW}$.

Figure 4.5: Microscope images of the Copper-glass surface with cavities of 1 mm diameter. Figure 4.5a blank surface; $m = 1.4\,\mu\mathrm{g}$ of cholesterol (m/z 369.8 inside the cavity after laser application with a laser power of Figure 4.5b $P_L = 105\,\mathrm{mW}$; Figure 4.5c $P_L = 234\,\mathrm{mW}$ and Figure 4.5d $P_L = 492\,\mathrm{mW}$. Arrows are added to guide the eye. Microscope: *DMRM Type 301-371.010*, Leica, Germany; objective: *567030*, Leitz Wetzlar, Germany; *10X/0.20 D* magnification. [60]

to Figure 4.5d, different laser powers are applied to the surface, with the analyte cholesterol placed inside the cavities. In Figure 4.5b, a circular color-shifted area, as marked by the blue arrows, can be seen at 105 mW. This is an effect related to surface oxidation. However, the surface remains intact.

In Figure 4.5c, Newton diffraction rings can be observed, marked by red arrows. These rings show that the surface begins to melt. Also, the ring diameter, as marked by the blue arrows, increases with a laser intensity of 234 mW. Black residuals of cholesterol can be identified on the boundary, as indicated by the green arrows. These are dried cholesterol residuals diffused from the center to the outer regions. Irregularities can be observed in the cavities, such as black stripes in Figure 4.5c,

which are defects in the lithography processing.

In Figure 4.5d, the area marked by the red arrows increases and blends into a black area and the Copper sinks into the glass. There are still residuals on the walls of the cavity which contribute to an ion signal. However, the cholesterol from the wall of the cavity is desorbed temporally-delayed as the surface temperature on this position does not reach the desorption temperature threshold. As a consequence, this small ion signal can be neglected. As already seen in Figure 4.5c, defects in the lithography processing can be observed.

The diameters of the marked areas are summarized in Table 4.2. The full width half

Table 4.2: Diameters and calculated power density of the marked areas in Figure 4.5 using the power meter experiment from Figure 4.3. [60]

	Figure 4.5b	Figure 4.5c	Figure 4.5d
$d_{\text{surface oxidation, blue arrows}}$ / µm	90	200	270
$d_{\text{surface melting, red arrows}}$ / µm	0	90	200

maximum (FWHM) value of a Gaussian Laser profile only depends on the standard deviation and constants. It is assumed that the blue arrows in Figure 4.5b and the red arrows in Figure 4.5c indicate the center of the laser spot, as the metals are beginning to melt on the surface as part of a phase transformation. The blue arrows in Figure 4.5c and the red arrows in Figure 4.5d are assumed to highlight the FWHM of the laser spot, being constant throughout the different used laser powers. Thus, the desorption diameter is $d_{S,\text{FWHM}} = 200\,\mu\text{m}$, taken as an estimation for the minimum desorption spot.

In comparison to the laser spot size in Figure 4.4, this diameter differs to the laser spot diameter due to the aforementioned reasons. The laser intensity for desorption is finally given by

$$\psi = \frac{P_L}{A_s} = \frac{P_L}{\pi \left(d_{S,\text{FWHM}}/2\right)^2}.$$

Thus, the maximum ψ_i yields for both blue diode lasers of 1.6 W and 3.5 W

$$\psi_i = \begin{cases} 22\,\text{W/mm}^2 \text{ for } i = 1.6\,\text{W} \\ 36\,\text{W/mm}^2 \text{ for } i = 3.5\,\text{W} \end{cases}$$

As a minimum desorption diameter was chosen, these laser intensities are considered an upper-limit that will be used throughout this thesis. If not stated otherwise, a laser intensity of $\psi = 16\,\mathrm{W/mm^2}$ will be used for the laser application.

The surface material melts and diffuses into the glass. The glass will hence exceed its softening point and the local surface temperature will be around $T \approx 1000\,^{\circ}\mathrm{C}$ [33, 60]. These surface effects can be traced back to a phase transformation of the metals from solid to liquid, interacting with the underlying isolator. The phase transformation is connected to the surface temperature and the temporal temperature gradient. The metal diffusion into the glass was first noted by applying a mixture of perchloric acid and ceric ammonium nitrate (*TechniEtch Cr01*, also known as *Chromium Etchant, MicroChemicals GmbH*, Germany [62]) to the surface, which removes the metal layers. Residuals of surface material are observed on the laser-applied spot, which could not be removed with these acids [60].

4.3 Laser-Surface Interaction

As outlined in the last section, residuals of the metals are trapped inside the glass of the sandwich structure after laser application. Therefore, the laser-surface interaction of the blue diode laser to the substrate will be investigated by white-light interferometry, mass spectrometry and optical emission spectroscopy.

4.3.1 White-light Interferometry

White-light interferometry is carried out to investigate the propagation of the melted metals inside the glass. In interferometry, light is split into a reference and a sample beam with a difference in the optical path. By interference of light, bright and dark circles (fringes) can be identified. In this interferometer, the reflections from a reference and the substrate surface are used to generate the fringes by constructive and destructive interference. A bipolar scan is performed on the substrate from the fringe of the highest intensity (zeroth order fringe) 10 µm upwards and 10 µm downwards. This scanning gives a sequence of interferograms that are transformed and Fourier-analyzed for phase information. Briefly, the surface map is calculated from the phase by the least square method. The parameters used for interferometry are summarized in Table A.6 of the appendix.

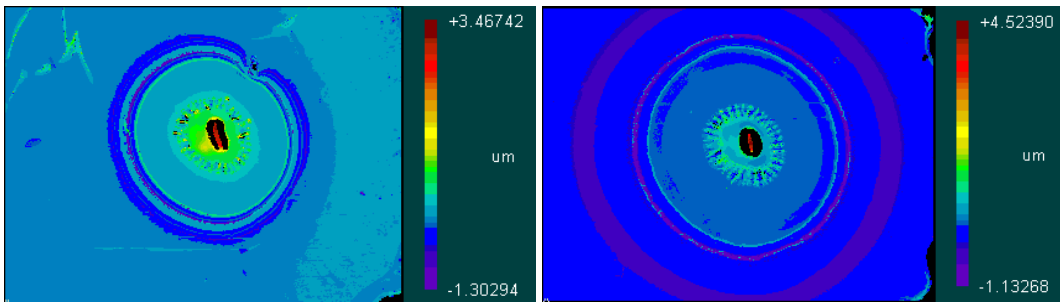

(a) (b)

Figure 4.6: White-light interferometry after laser application to the Copper-glass surface with a laser intensity of $\psi = 16\,\mathrm{W/mm^2}$ for $t = 10\,\mathrm{s}$ Figure 4.6a once and Figure 4.6b ten times, White-light interferometer: *Zygo NewView 5000*, USA [60].

In Figure 4.6, white-light interferometric images of a single laser application (Figure 4.6a) and ten laser applications (Figure 4.6b) to the Copper-glass surface are shown. The intensity of the diode laser is $\psi = 16\,\mathrm{W/mm^2}$, applied to the surface for $t = 10\,\mathrm{s}$ each shot. In Figure 4.6a, the metals sink roughly 3 µm into the glass, with surface wrinkles formed in the center of the laser application. The surface wrinkles are formed by gradients of the surface tension after cool down of the substrate. These are linked to a phase transformation of the metals from solid to liquid. For ten laser applications, the depth slightly increases to 4.5 µm, with the same surface modifications previously observed. Therefore, the melted metals are close to a stationary condition after the first laser application. In that manner, it is worthwhile to focus on different laser intensities applied to the surface to narrow the point of the phase transformation.

4.3.2 Mass Spectrometry

The trapped metals absorb the laser light and heat the substrate. This heating triggers desorption and will be verified by mass spectrometry. The FµTP [17] will be used for the rest of this thesis, as justified in the last two chapters. In order to account for the signal background, the extracted-ion chromatogram (XIC) is evaluated with the plasma turned on, but the laser turned off and vice versa. No significant and compound-relevant ion signal is detected. Therefore, the laser is taken for desorption, the plasma for ionization.

Figure 4.7 shows the XICs of cholesterol (m/z 369.8) for a single laser application and ten laser applications with a laser intensity of $\psi = 16\,\mathrm{W/mm^2}$, ten seconds each.

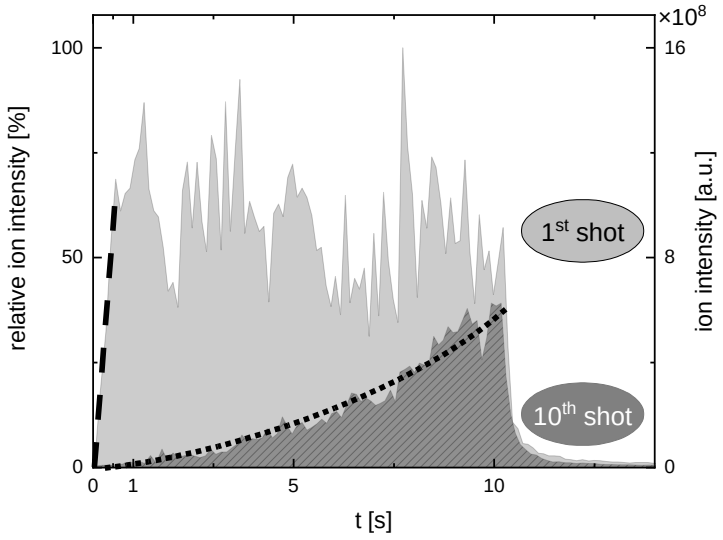

Figure 4.7: Comparison of the XICs from the first and the tenth laser application on a Copper-Chromium surface for $t = 10\,\mathrm{s}$ [60] ($\psi = 16\,\mathrm{W/mm^2}$, $m = 1.4\,\mu\mathrm{g}$).

In the first shot, the maximum signal response is reached immediately, limited by the sampling rate of the mass spectrometer and fluctuations of the FµTP . For the tenth shot, at least ten seconds are required to match the minimum signal intensity of the first laser application. Comparing the relative intensity from the first and the tenth shot, the ion intensity decreases by 40 % to 50 %. This means that the substrate is less efficiently heated due to the glass barrier, but still sufficient enough to trigger desorption of the analyte. As a high amount of $m = 1.4\,\mu\mathrm{g}$ is taken in this experiment, the decreased ion intensity is not correlated to an insufficient amount of cholesterol. A single shot with this amount provides a stable ion signal for more than two minutes. As the desorption is triggered rapidly, it is assumed that a significant amount of the analyte is not trapped with the metal in the glass. The continuous desorption signal allows for a calibration of the arbitrary unit ion current to the compounds amount in a later section of this thesis.

The phase transformation on the surface correlates to a sudden increase of the ion current. As previously mentioned, the local glass temperature is around $T \approx 1000\,^{\circ}\mathrm{C}$ [33, 60]. At those temperatures most analytes will fragment excessively, if the heat is directly applied the analyte. This is not the case for cholesterol or other tested non-volatile chemicals. A possible interpretation is the Leidenfrost effect known from water droplets on a hot plate, which will buffer the analyte from direct surface heating [60]. The maximum desorption time scale is dictated by the propagation of the melted metals through the glass. This time scale is directly linked to the

laser stabilization in the realm of microseconds and will be discussed in the next section. Therefore, it seems reasonable to propose that the desorption step occurs on a similar time scale.

4.3.3 Optical Emission Spectroscopy

If surface material was removed from the substrate, a laser-induced plasma would emit characteristic and discrete light [63]. Therefore, optical emission spectroscopy will be used to cross-check for plasma emission from the surface. An intensified charge-coupled device (ICCD) and a diode laser controller are triggered by a function generator (*FG300*, *Yokogawa Denki*, Japan) at a square wave pulse frequency of 10 kHz. The gate delay of 13 µs origins from the laser stabilization. The settings for the ICCD and the diode laser operation as well as the trigger signal are listed in Table A.7 of the appendix.

A 5× magnifying objective is mounted below the diode laser to focus the laser beam. A long pass filter (*RG610*, thickness 2 mm, *Schott AG*, Germany) is used to filter the dominant wavelength of the diode laser. The laser intensity to the surface is 16 $\mathrm{W/mm^2}$. A collimator lens (*F220 SMA-A*, *Thorlabs*, USA) connected to an optical fiber (spectral range from 200 nm to 1100 nm, *P600-2-SR*, *Ocean Optics*, USA) is used for light transmission to the ICCD. The substrate is placed in a gas chamber with a quartz window for laser transmission.

Air, Helium and Argon are used with ranging gas pressures from vacuum conditions to atmospheric pressure ($p = 10$ mbar to 1000 mbar), yielding similar results. According to the law of Paschen, the gas pressure is correlated to the plasma expansion. Therefore, a decreasing gas pressure causes plasma expansion at a fixed breakdown voltage. However, the emission spectrum recorded from the surface does not qualitatively change with gas pressure or composition. Therefore, only Helium at atmospheric pressure is exemplarily shown in the emission spectrum taken by an ICCD camera in Figure 4.8.

Continuously emitted light can be detected immediately on the full spectral range, without any significant spectral lines known from plasmas. The most intense peaks are multiples of the laser wavelength, that is $\frac{1}{2}\lambda_0 = 225$ nm, $\frac{3}{2}\lambda_0 \approx 670$ nm and $2\lambda_0 \approx 888$ nm possibly coming from optical interferences in the spectrometer. If

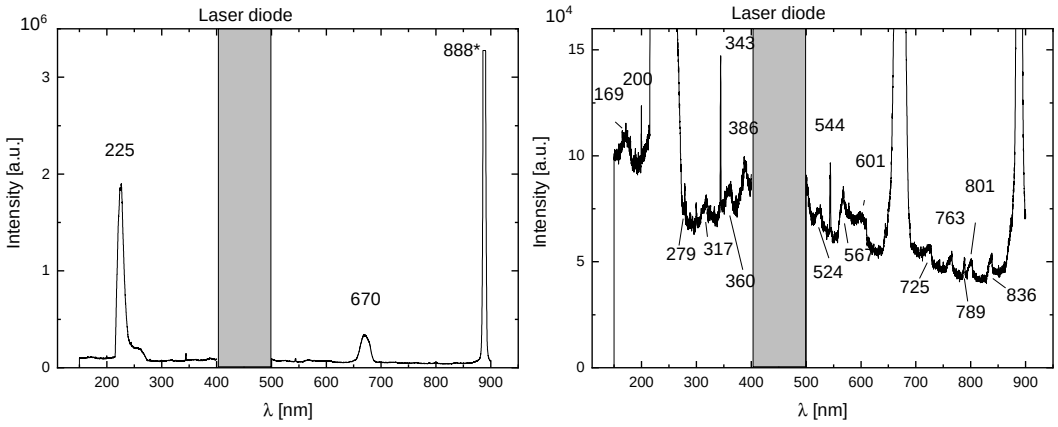

(a) (b)

Figure 4.8: Emission spectra taken by an ICCD camera, with the diode laser applied to the substrate ($\psi = 16\,\mathrm{W/mm^2}$, $f_{\text{diode laser}} = 10\,\mathrm{kHz}$, $p_{\text{Helium}} = 1\,\mathrm{bar}$). Figure 4.8a full emission spectrum of the surface-reflected light. The emission line at 888 nm is marked, as the signal is capped. Figure 4.8b zoomed-in view on the less intense light of the emission spectrum. ICCD: *Andor iStar DH 720 18F-03, Oxford Instruments*, Great Britain.

there was a plasma on the surface, different gas compositions would show characteristic emission lines, such as $\lambda = 706\,\mathrm{nm}$ in Helium discharges or $\lambda = 696\,\mathrm{nm}$ for Argon discharges [64]. The less intense peaks are thus not related to any emission lines known from plasmas. It is thus assumed that the light emitted from the surface is not a plasma, but glowing metal. In terms of surface modification, these experiments indicate that the surface is heated within microseconds. In this sense, the desorbate must be desorbed on a similar time scale to avoid excessive fragmentation, as outlined previously. With 200 ms sampling time of the MS and a generator frequency of 20 kHz, $^{200\,\mathrm{ms}}/_{50\,\mu\mathrm{s}} = 4000$ full voltage cycles pass each mass spectrum. In this sense, synchronization of the laser and the plasma source is not feasible, as the MS is the bottle-neck of the method.

4.4 Analyte-depended Laser Intensity Thresholds

In Figure 4.9, an extracted ion mass chromatogram (m/z 230.4) of the non-volatile herbicide propazine is shown for two different applied laser intensities. First, the laser is applied to the surface with an intensity of $3\,\mathrm{W/mm^2}$ for five minutes and then abruptly increased to $16\,\mathrm{W/mm^2}$ until no signal is detected any further. The increase in laser power from $3\,\mathrm{W/mm^2}$ to $16\,\mathrm{W/mm^2}$ leads to an increase in the ion

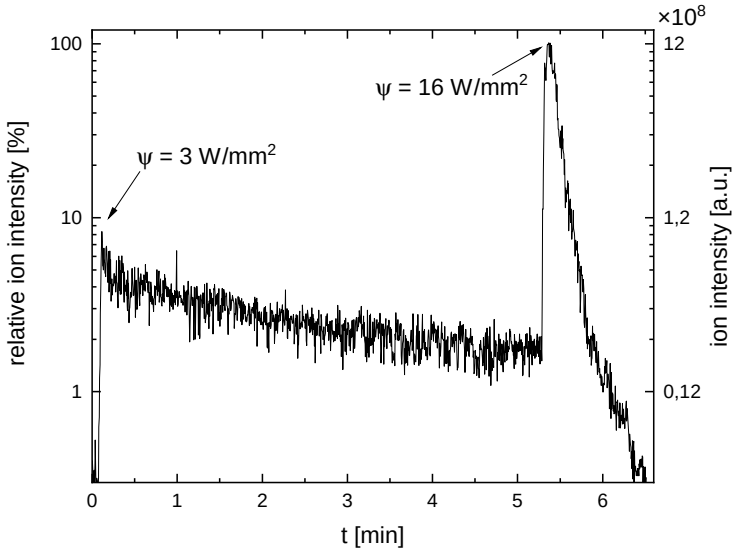

Figure 4.9: Extracted ion mass chromatogram for propazine with different laser intensities applied to the surface ($m = 50\,\mathrm{ng}$). [60]

intensity from 1×10^8 a.u. to 1.2×10^9 a.u. Furthermore, only roughly 17 % of the injection time into the ion trap is required for the higher laser intensity. This means that if both ion signals were measured with identical injection times, the signals would be roughly two orders of magnitude apart. A key element in the desorption is the change of phase of the metals on the surface. This experiment further suggests that there are different desorption levels.

In Figure 4.10, the integrated area of the XICs of cholesterol (m/z 369.8) is measured with constant laser fluences E, which is realized with increasing laser intensities (or laser powers P) but decreasing laser application times t to the surface. Each XIC is integrated and averaged for triplicates, which is three measurements for each point. The AGC is turned off up to $7\,\mathrm{W/mm^2}$ to match injection times of 5 ms into the ion trap for each measurement. For the other measurements, the maximum amount of charges aims at 5×10^7, controlled by the AGC. Interestingly, the area increases by roughly two orders of magnitude from 2×10^6 a.u. up to 9×10^7 a.u. with decreasing laser application times from 30 s down to 4.6 s, written next to each point. At $3\,\mathrm{W/mm^2}$ to $7\,\mathrm{W/mm^2}$, less than 10 % of the maximum ion signal are detected. Over $12\,\mathrm{W/mm^2}$, the signal area remains constant. In this sense, it is assumed that the cholesterol is fully desorbed from the surface, achieving the maximum possible efficiency for laser desorption at roughly $12\,\mathrm{W/mm^2}$. The different, highlighted experimental data can be correlated from Figure 4.10

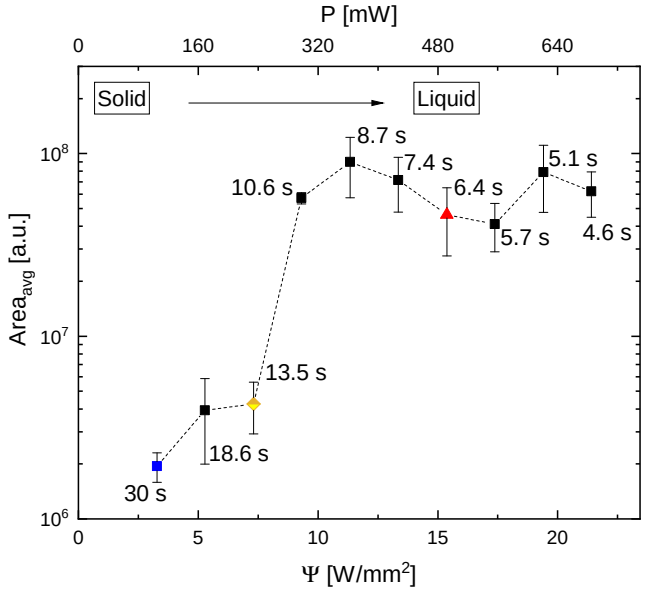

Figure 4.10: Integrated area of the XICs of cholesterol for different laser intensities and laser application times, but a constant laser fluence to the surface ($m = 1.4\,\mu g$). [60]

to the surface modifications of Figure 4.5b to Figure 4.5d. In this sense, the ($3\,W/mm^2$, $30\,s$) point is linked to Figure 4.5b, the ($7\,W/mm^2$, $13.5\,s$) point is linked to Figure 4.5c and the ($16\,W/mm^2$, $6.4\,s$) point is linked to Figure 4.5d.

On the one hand, the increase in the ion intensity relates to the change of phase on the surface from solid to liquid. On the other hand, the desorption is strictly connected to the surface temperature. The surface reaches an equilibrium temperature on the surface due to conduction and thermal radiation. Therefore, two conclusions can be drawn from this experiment. First, for an efficient desorption, a critical temperature on the surface is required. Second, the heating must take place in a thermodynamical disequilibrium with a change from the solid to the liquid phase on the surface with a temporal temperature gradient of less than seconds. It is worth noting that recent publications have shown that lipids and non-volatile chemicals cannot be efficiently desorbed and ionized using an LTP and a heated substrate [18, 65]. In contrast, these results indicate that there is an analyte-depended laser intensity threshold.

The following experiments of this chapter are carried out with the vertically mounted substrate, as seen in Figure 3.2. In Figure 4.11, different integrated ion intensities are shown for different compounds and increasing laser intensities. The mass range for all compounds is $\delta m/z$ 20 centered around their base peak with an injection time

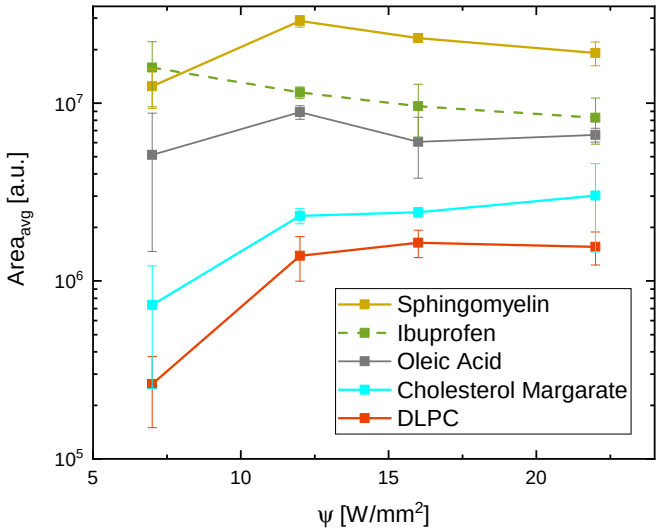

Figure 4.11: Integrated area of the XICs of sphingomyelin, ibuprofen, oleic acid, cholesterol margarate and 1,2-dilauroyl-sn-glycero-3-phosphocholine (DLPC) for different laser intensities. The amount taken for the compounds are summarized in Table 4.3. [52]

fixed at 5 ms. The amounts taken for the compounds are summarized in Table 4.3. With an increasing laser intensity, a sudden increase in the slope of the individual curves indicates a more efficient desorption. Higher amount of the compounds only shift the signal on the ordinate to higher values. Compounds such as ibuprofen efficiently desorb at lower intensities of 7 W/mm^2, being constant in desorption even for higher laser intensities. This is the surface oxidation limit known from Figure 4.10. Other compounds such as sphingomyelin, oleic acid or cholesterol efficiently desorb at 12 W/mm^2, which is the surface melting limit known from Figure 4.10. The other three lipids first increase from 7 W/mm^2 to 12 W/mm^2 within the first oxidation and melting limits, but also show another increase in ion response up to 36 W/mm^2. This threshold will be discussed on the basis of a liver extract in the following.

In Figure 4.12, the different laser intensity thresholds in laser desorption are shown for several lipid classes of a complex sample. In Figure 4.12a, the desorption signal is integrated for triplicates, separately for cholesterol (m/z 369.8) and the lipid classes of phospholipids and glycerophospholipids ($\delta m/z$ 560-680). In Figure 4.12b, the mass spectra with laser intensities of 22 W/mm^2 and 36 W/mm^2 are directly compared. Both spectra are normalized for the base peak of the spectrum. While the base peak shows roughly equal heights for both laser intensities, the ion intensity for the phospholipids and glycerophospholipids increases with higher laser intensities.

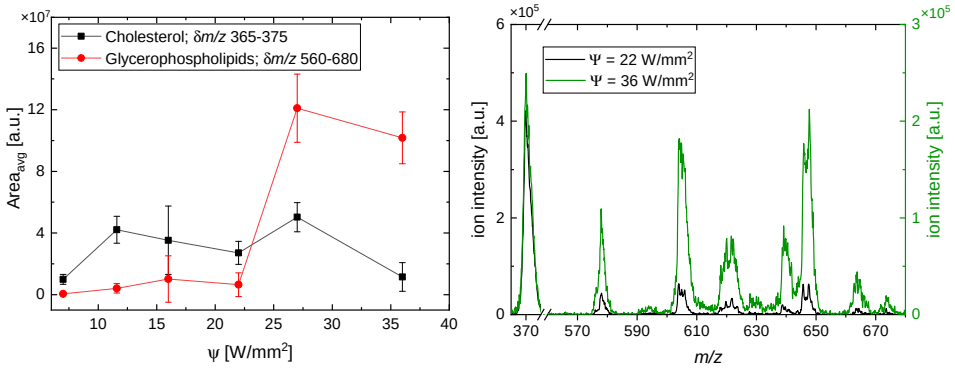

Figure 4.12: Figure 4.12a: Signal areas of cholesterol (m/z 369.8) and phospholipids as well as glycerophospholipids ($\delta m/z$ 560-680) for different laser intensities, Figure 4.12b: A mass spectrum ($\delta m/z$ 370-680) of bovine liver extract with laser intensities of $\psi = 22\,\mathrm{W/mm^2}$ and $\psi = 36\,\mathrm{W/mm^2}$ applied to the surface ($m = 1.3\,\mu\mathrm{g}$). [52]

With a laser intensity of $36\,\mathrm{W/mm^2}$, the ion intensity of the phospholipids and glycerophospholipids reaches almost the same height as the base peak. Therefore, these lipids require $36\,\mathrm{W/mm^2}$ of laser intensity for efficient laser desorption. It is worth noting that this threshold is valid for the direct application of $36\,\mathrm{W/mm^2}$ as well as an abrupt increase from $22\,\mathrm{W/mm^2}$ to $36\,\mathrm{W/mm^2}$ within the same experiment on a single spot. The ion intensities of all peaks in Figure 4.12b are limited by the defined amount of ions in the trap. In this sense, the higher the diversity of ion species, the smaller the ion intensity for single ion species becomes.

The laser intensity threshold is linked to several parameters such as the topological area, the absorption efficiency of the compound and the heat conduction of the surface. The laser intensities for efficient laser desorption of all discussed compounds are summarized in Table 4.3.

Table 4.3: Laser intensities required for efficient laser desorption, listed for several compounds and their amount taken in the experiment.

Compound	ψ / W/mm^2	Amount / µg
Ibuprofen	7	0.25
Sphingomyelin	12	0.50
Oleic Acid	12	0.05
Cholesterol	12	1.4
Propazine	16	0.05
Cholesterol Margarate	36	0.50
DLPC	36	0.25
Phospholipids & Glycerophospholipids	36	1.3

The different amounts of the analytes emerge from the response factor of each compound. The response factor is the ratio between the amount of the analyte and the ion response on the MS. This factor includes the efficiencies of desorption, ionization and the detection. Another explanation are the different binding energies of the compounds to the surface. In this sense, the Copper may act as a catalyzer for oxidation or reduction of the compounds.

5 Analytical Perspective

Apart from the physical mechanisms, the analytical point of view has not been intensively discussed, yet. However, the characterization of standards and the soft ionization capability of the method are mandatory to describe complex and unknown samples. All standards used in this chapter are listed in Table A.8 of the appendix.

First, a mass calibration solution will be used to evaluate if the laser desorption is limited by a certain mass of the analyte. Second, cholesterol will be presented as a standard with high biological significance. This standard is subsequently mixed with human blood plasma to investigate matrix effects from this mixture. In this sense, the analytical performance of the pure and mixed analytical standard will be compared to one another. Next, the ionization mechanisms of different hydrophobic compounds as well as their ionization mechanisms will be discussed. This section also presents a complex sample, which consists of several different analytes. Moreover, positive and negative ionization will be compared. Finally, the analytical performance and progress of a previous study to this thesis is intensively studied.

For the following experiments, the substrate is set perpendicular to the inlet of the MS, the plasma is aligned parallel to the substrate, as shown previously in Figure 3.2.

5.1 Mass-dependency of Laser Desorption

Initially, a well-known mass calibration solution of mass spectrometry is used. For this reason, the results allow fast comparison to well-known spectra. On the other hand, the detection of the compounds in the mixture shows that the laser desorption is not limited by the mass of a compound, at least up to m/z 2000. In Figure 5.1, a mass spectrum of the calibration solution is presented. This solution is a commercially available mixture of caffeine (mono-isotopic mass 194.1 u),

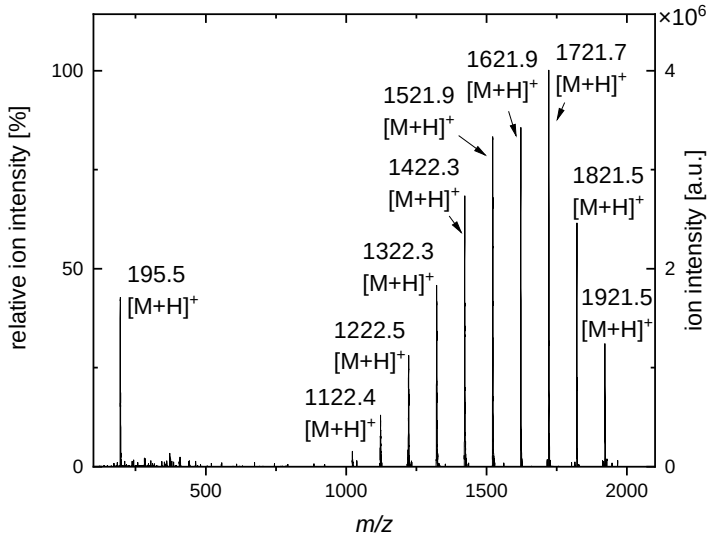

Figure 5.1: Mass spectrum of the calibration solution ($m_{\text{Caffeine}} = 10\,\text{ng}$, $m_{\text{MRFA}} = 0.5\,\text{ng}$, $m_{\text{Ultramark}} = 5\,\text{ng}$). [52]

Methionin-Arginin-Phenylalanin-Alanin (MRFA, mono-isotopic mass 523.7 u) and fluorinated phosphazenes called Ultramark (most abundant mono-isotopic mass 1721.0 u). MRFA does not seem to be ionized by the plasma. Caffeine and the fluorinated phosphazenes are detected as quasi-molecular ions. Thus, the desorption process is generally able to cover molecules up to m/z 2000. Further, the mass spectrum matches to electrospray-based methods [66].

5.2 Cholesterol

Cholesterol is found almost everywhere in the human body, as it is required for cell formation and is synthesized by the body. On the other hand, disturbances in cholesterol levels are known to cause numerous diseases [67–71] or neurodegeneration [72] and thus have a high biomedical significance. Cholesterol standard is taken to estimate the analytical performance of the method.

5.2.1 Mass spectrum and Calibration Curve of the Compound

In Figure 5.2, an averaged mass spectrum of cholesterol is shown. Cholesterol (mono-isotopic mass 386.4 u) is detected in the gas phase as a protonated fragment by a neutral loss of water ($[\text{M} - \text{H}_2\text{O} + \text{H}]$, m/z 369.8). No other signals with more

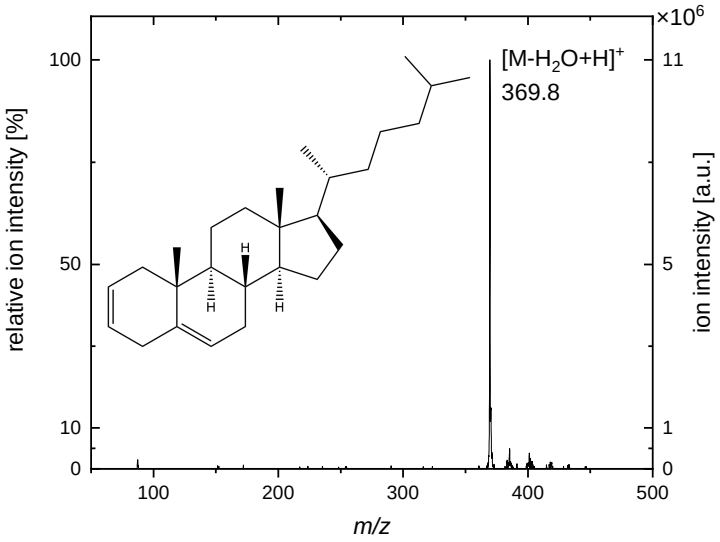

Figure 5.2: Mass spectrum of cholesterol ($m = 0.2\,\mu g$). [60]

than 5 % of the ion intensity of this fragment are observed, including minor oxygen adducts up to m/z 400. On the one hand, single fragments can be used to track chemical reactions and can help to identify chemical compounds. On the other hand, excessive fragmentation is unwanted as the fragmentation pattern cannot be tracked anymore on the used mass spectrometers.

A calibration curve for cholesterol can be seen in Figure 5.3. The XICs of cholesterol

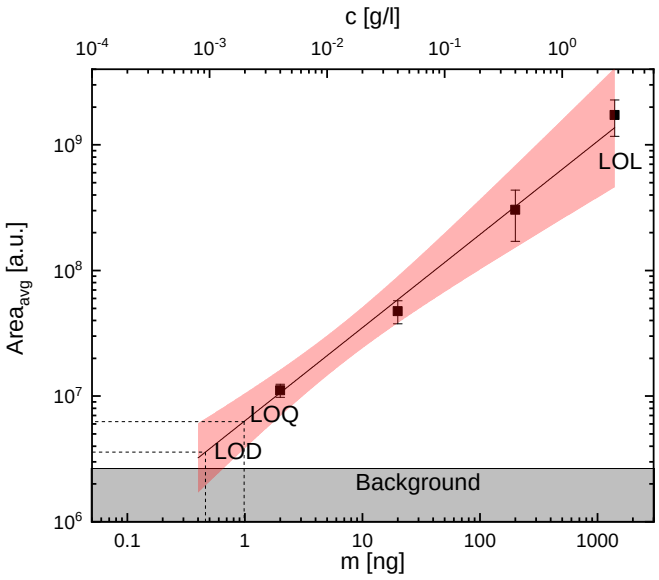

Figure 5.3: Calibration curve of cholesterol. [60]

(m/z 369.8) are time-integrated for each amount and averaged over triplicates.

The ion signal after laser desorption from a blank cavity is taken to calculate the background level. The LOD is calculated on the basis of this level plus 3σ and the intercept with the linear fit, as mentioned in the fundamentals. Likewise, the limit of quantification (LOQ) is calculated from the intercept of the fit with background level plus 10σ. The LOD for cholesterol is 460 fg, the LOQ is 1 ng. The LOL is above 1 µg, yielding a linear dynamic range of at least three orders of magnitude.

It is worth noting that the linear regression coefficients are only precise if the standard deviation is constant for all amounts of the analyte, thus for homoscedastic data. However, this is not the case for this method. A different calibration method presented by Hubaux and Vos [73] addressed this issue. The authors introduced another Gaussian distribution of the measurement points in addition to the Gaussian distribution of the background signal. The advantage of this approach is that a false-positive, false-non-detect declaration is established, estimated by the overlap of these two Gaussian distributions. This declaration thus reduces the error in the LOD given by the probability of a false-positive background and false non-detect signals. However, the detection limit shifts to higher values. A more detailed discussion is given by Voigtman [74].

Practically, a confidence interval with a rather arbitrary error rate of 5 % or a confidence level of 95 % is added to the linear fit of the calibration curve. The LOD previously calculated can be converted in two steps. First, the intercept of the background signal plus 3σ limit with the linear fit is vertically projected to the upper limit of the confidence interval. Second, a horizontal projection to the other end of the confidence interval marks the LOD using the method by Hubeaux and Vos. Hence, the extrapolated LOD is roughly two times higher.

The detection of cholesterol without any sample modification is not self-evident, as other AIMS methods reported on sample preparation. For instance, DESI used betaine aldehyde to form a hemiacetal salt with the hydroxyl group of cholesterol [75]. Without the help of betaine aldehyde, the authors reported an LOD of 200 ng. DART [76] used an internal standard for calibration with a concentration of 20 mg/l. The authors used an amount of 1 µl in total, which translates into an LOD of 20 ng. In contrast, laser desorption coupled with plasma ionization both increases the LOD for the detection of cholesterol and simplifies the experiment as no sample preparation is required. However, human serum cholesterol as used in DART is a much more complex sample than the cholesterol standard as it is not as pure as the

standard due to triglycerides, proteins and other ingredients present in the sample. Also, the filament of the paper surface in DART traps the liquid inside and thus reduces the desorption efficiency.

5.2.2 Cholesterol Mixed with Blood Plasma as a Biological Matrix

For analytical performance, only pure compounds were considered so far. In contrast, real-life samples often come with biological matrices, such as tissue, which contain more than a single analyte. Therefore, it is worth testing standards in more complex environments and mediums. These matrices are linked to inherent matrix effects, which will be described on the basis of blood plasma. Blood plasma, which is acquired by centrifugation of human blood, is mixed with cholesterol. The residuals in blood plasma are proteins, lipids, glucose, hormones and many more components. 55 ng of cholesterol is added (spiked) to both pure and chloroform-diluted plasma.

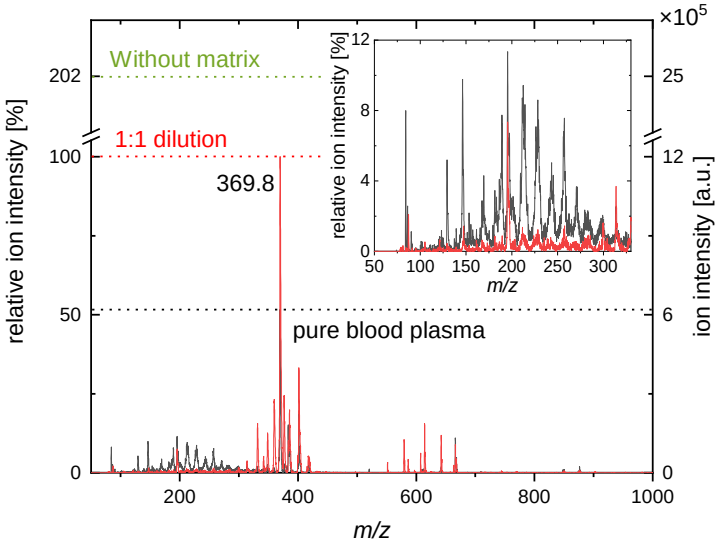

Figure 5.4: Mass spectra of pure and diluted blood plasma with $m_{\text{Cholesterol}} = 55$ ng of cholesterol spiked in both matrices. The levels indicated in the figure describe the maximum intensity of cholesterol in pure and diluted plasma as well as without a matrix. [60]

In Figure 5.4, mass spectra of cholesterol in blood plasma, both pure (black line) and 1:1 diluted in chloroform (red line), are shown. The cholesterol levels in pure as well as in diluted plasma and without any matrix are indicated. A major difference between the pure and diluted form is the amount of ions in the low mass range from m/z 75 to m/z 300, commonly denoted as chemical ion background or chemical noise

from the matrix. Those ions are related to the formation of a salty, crystallized layer, which desorbs the analyte less efficiently. The same layer also forms in high amounts of pure standards without a matrix. Hence, this effect is not a conventional matrix effect, but a concentration effect, which is minimized by dilution. This chemical background of the pure plasma causes a decrease in the ion intensity of cholesterol (m/z 369.8) from approximately 2.5×10^6 a.u. without a matrix to 6×10^5 a.u. in pure plasma. A 1:1 dilution increases the ion intensity of cholesterol by 50 % already. The crystallized layer continues to decrease with further dilution of the blood plasma.

In a 1:100 dilution of the blood plasma in chloroform, the presence of the layer becomes neglectable, with similar ion intensities of cholesterol without a matrix. A

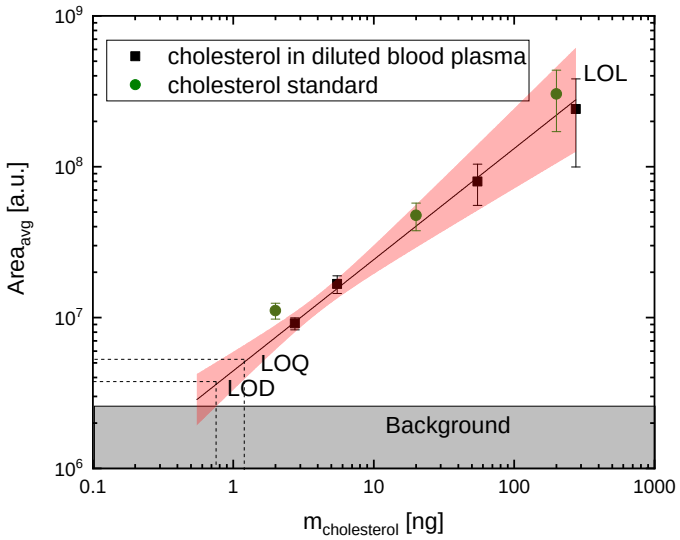

Figure 5.5: Calibration curve of cholesterol as a standard and in diluted blood plasma. [60]

calibration curve of cholesterol in 1:100 diluted blood plasma is shown in Figure 5.5. For comparison, the data from Figure 5.3 is added to the figure. The calibration curves of cholesterol with diluted (black data) and without the plasma (green data) are very similar in slope, with a constant shift on the ordinate. This means that the biological matrix does not decrease the sensitivity of the cholesterol detection in a 1:100 dilution, but only shows an increase in the chemical ion background. The LOD is 800 fg and the LOQ is roughly 1 ng. Hence, these quantification limits are shifted by a constant factor as well, causing the LOD to be approximately doubled, whereas the LOQ remains almost constant. The LOL is at least 300 ng, being lower due to the presence of the blood plasma.

5.3 Other Lipids and Hydrophobic Compounds

In the following section, different lipid classes will be tested. These lipids are known to show a characteristic fragmentation pattern [77], making them more susceptible to environmental conditions. In this sense, it is worthwhile to evaluate their analytical performance.

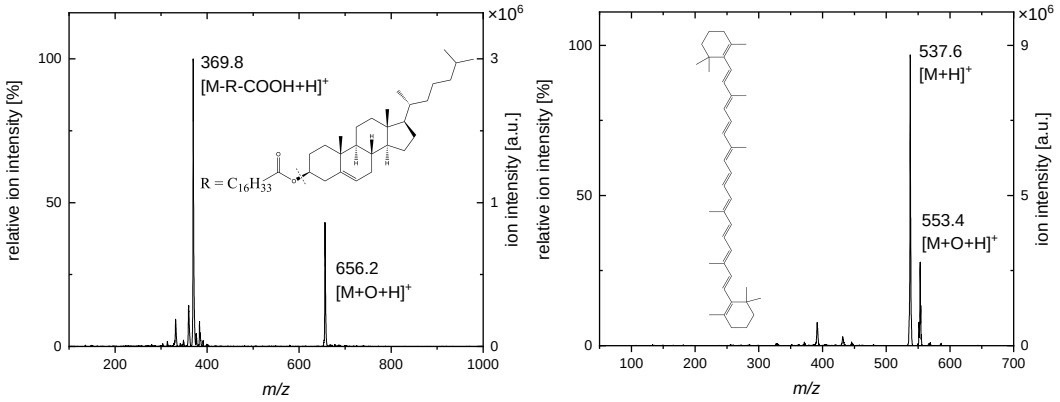

Figure 5.6: Mass spectra of Figure 5.6a cholesterol margarate ($m = 0.5\,\mu g$) and Figure 5.6b beta carotene ($m = 50\,ng$). [52]

In Figure 5.6a, a mass spectrum of cholesterol margarate (mono-isotopic mass 638.6 u) is shown. Cholesterol margarate is a fatty ester of cholesterol. A fragment of dehydrated cholesterol ($[M - R - COOH + H]$, m/z 369.8) and a protonated oxygen adduct of the molecule ($[M + O + H]$, m/z 656.2) are detected. The protonated oxygen adduct of the molecule is measured with 50 % of the base peak ion intensity. The fragment origins from cleavage of the carbon chains. In this sense, this lipid can be detected at the same mass as the cholesterol standard, which is detected after the loss of the hydroxyl group. For complex samples, this fragmentation path plays an important role, as it may decrease the sensitivity in cholesterol detection.

The mechanism of the fragmentation remains unknown. It is assumed that the standard is fragmented either in the drying process or in the gas phase. Laser desorption does not generally cause fragmentation with increasing mass of the compound. Also, it is not inherently linked to the accumulated energy fluence deposited on the surface, as seen in section 4.4. The fragmentation mostly depends on the stability of a compound in the gas phase, especially when exposed to ozone, highly reactive species and UV light produced by the plasma.

The effect of oxygen addition is known from other compounds, such as the addition of oxygen atoms in polyunsaturated molecules, for example polycyclic aromatic hydrocarbons [78]. In this sense, the oxygen addition to double-bonded molecules is tested, with beta carotene as a representative. In Figure 5.6b, a mass spectrum of beta carotene (pro-vitamin A, mono-isotopic mass 536.4 u) is shown. The base peak of the spectrum is linked to the quasi-molecular ion ($[M + H]$, m/z 537.6). A single oxygen adduct to the polyunsaturated molecule ($[M + O + H]$, m/z 553.4) is observed with 25 % of the base peak ion intensity, without any fragments being detected.

In contrast to cholesterol, calibration curves for cholesterol margarate and other lipids do not show a linear correlation between the ion intensity and the amount of the analyte. One reason is that the sensitivity of desorption and ionization of certain lipid classes is lower than for cholesterol, even with high amounts. Also, lipid signals commonly last several seconds, whereas cholesterol signals can be detected over minutes.

Further, laser desorption is a thermally driven process, with distinct laser intensity thresholds for different compounds, as seen in the previous chapter. If this threshold is not met, the compound will tend to fragment, as the surface is slowly heated. Therefore, only qualitative effects were analyzed.

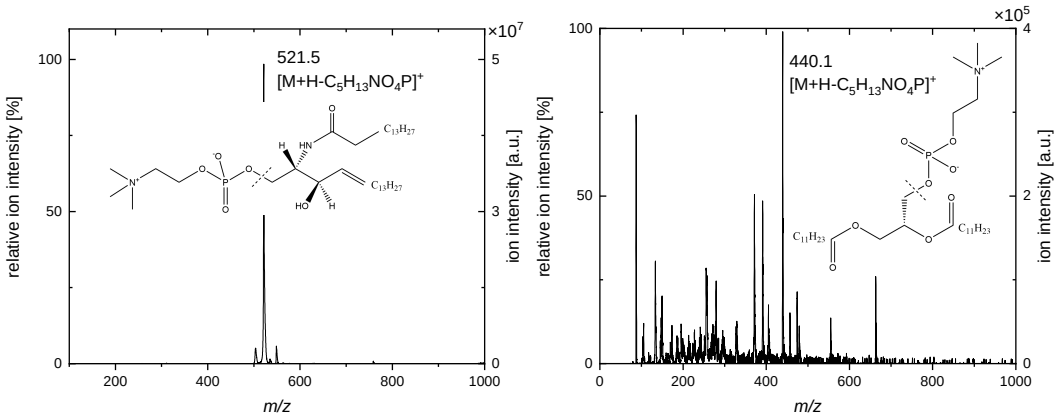

Figure 5.7: Mass spectra of two lipid classes. Figure 5.7a sphingomyelin (SPM, $m = 250$ ng) as a representative from the group of sphingolipids and Figure 5.7b 1,2-dilauroyl-sn-glycero-3-phosphocholine (DLPC) from the group of glycerophospholipids ($m = 50$ ng) [52]

In Figure 5.7a, a mass spectrum of sphingomyelin (SPM, mono-isotopic mass 702.6 u)

is presented. SPM is taken as a representative from the group of sphingolipids. It is detected by a neutral loss of the phosphocholine head group ($C_5\,H_{13}\,NO_4\,P$, m/z 182), resulting in the detected signal of m/z 521.5 ($[M + H - C_5\,H_{13}\,NO_4\,P]$).

In Figure 5.7b, a mass spectrum of 1,2-dilauroyl-sn-glycero-3-phosphocholine (DLPC, mono-isotopic mass 621.4 u) is shown. DLPC belongs to the group of glycerophospholipids. As with sphingomyelin, the ionized molecule is detected by a neutral loss of the phosphocholine head group, resulting in m/z 440.1 ($[M + H - C_5\,H_{13}\,NO_4\,P]$). In literature, this fragmentation pattern has been reported by Peng *et al.* [77] using a Laser-APCI-system. It is not well known what causes the fragmentation [79, 80].

5.3.1 Bovine Liver Extract as a Complex Sample

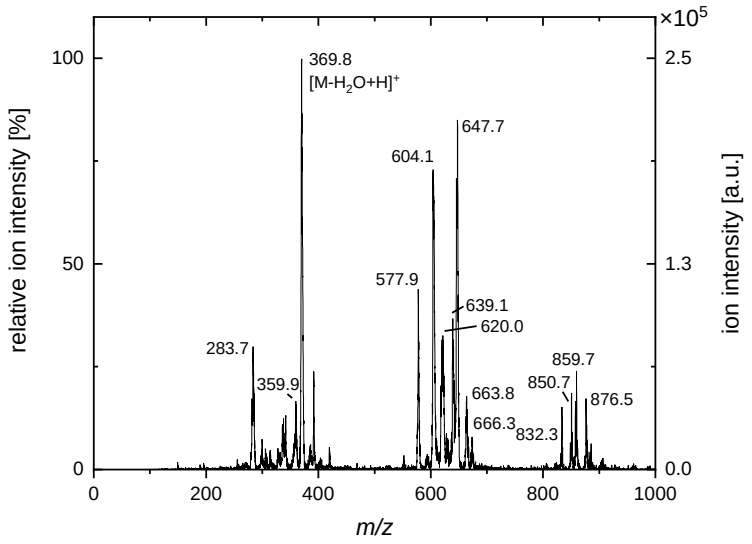

Figure 5.8: Mass spectrum of bovine liver extract ($m = 1.25\,\mu g$). [52]

In Figure 5.8, a mass spectrum of bovine liver extract is shown. The lipid profile given by the manufacturer [81] includes 42 % phosphatidylcholines, 22 % phosphatidylethanolamines, 8 % phosphatidylinositols, 7 % cholesterol, 1 % lysophosphatidylinositols and 20 % others [81]. Fatty acids and sterols are detected in the mass range of $\delta m/z$ 200-400, phospholipids and glycerophospholipids in the mass range of $\delta m/z$ 500-700 and triacylglycerols in the mass range of $\delta m/z$ 800-900.

The lipid profile given by the manufacturer lists cholesterol only by 7 % of the total extract. In contrast, cholesterol is detected with the highest ion intensity in Figure 5.8. This effect is partly due to the laser intensity threshold of different

analyte classes, known from section 4.4, and their fragmentation patterns resulting in the same detected masses, known from the analyte cholesterol margarate in Figure 5.6a. Even though the identification requires validation by tandem mass spectrometry using fragment ions and higher mass accuracy, the simultaneously detected, different lipid classes prove the ability of the method for lipid profiling.

5.4 Comparison of Positive and Negative Ionization

So far, only positive ionization has been considered. This section deals with the comparison of compounds that can be detected in both ion modes. Also, these compounds share an ionization mechanism, that will be discussed in the following.

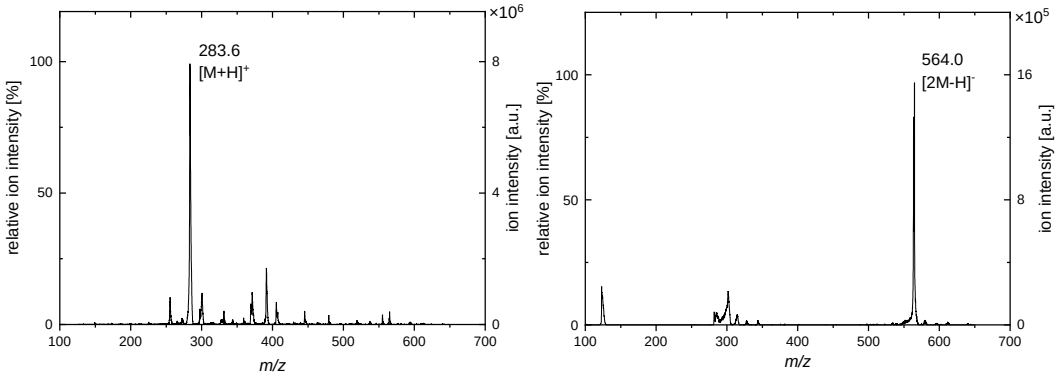

Figure 5.9: Mass spectra of oleic acid in Figure 5.9a positive ion mode and Figure 5.9b negative ion mode ($m = 50\,\mathrm{ng}$). [52]

Oleic acid is well-known as the mono-unsaturated omega-9 fatty acid. In Figure 5.9, mass spectra of oleic acid (mono-isotopic mass 282.3 u) are shown. The compound is detected in positive (Figure 5.9a) and negative (Figure 5.9b) ion mode. While in positive ion mode, a quasi-molecular ion ($[\mathrm{M}+\mathrm{H}]$, m/z 283.6) is observed, dimers ($[2\,\mathrm{M}-\mathrm{H}]$, m/z 564.0) are detected in negative ion mode, using the same amount of the analyte. The ion intensity of the quasi-molecular ion in positive ion mode is slightly higher than the ion intensity of the dimer in the negative ion mode. The underlying ionization mechanism was first discovered using non-steroidal anti-inflammatory drugs (NSAIDs). The NSAIDs are mostly known by ibuprofen and ketoprofen [82–84].

In Figure 5.10, mass spectra of ibuprofen in positive (Figure 5.10a) and negative

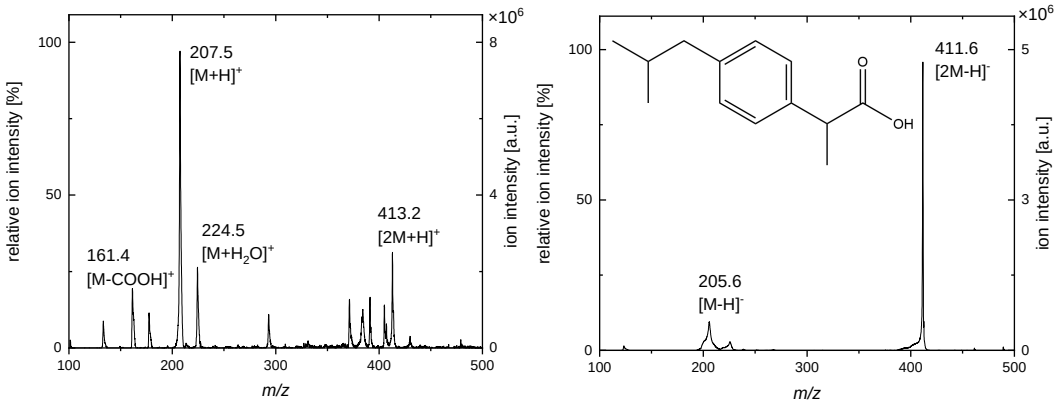

Figure 5.10: Mass spectra of ibuprofen, Figure 5.10a positive ion mode, Figure 5.10b negative ion mode ($m = 250\,\mathrm{ng}$). [52]

(Figure 5.10b) ion modes are shown. Ibuprofen (mono-isotopic mass 206.3 u) is detected as a fragment by the loss of the carbolyxic group ($[\mathrm{M} - \mathrm{COOH}]$, m/z 161.4), as a quasi-molecular ion ($[\mathrm{M} + \mathrm{H}]$, m/z 207.5) and as an adduct by addition of water ($[\mathrm{M} + \mathrm{H_2O}]$, m/z 224.5). In flowing atmospheric-pressure afterglow (FAPA) ionization, these adducts were observed as well [85]. Also, its dimer is observed ($[2\,\mathrm{M} + \mathrm{H}]$, m/z 413.2). In negative ion mode, the dimer ($[2\,\mathrm{M} - \mathrm{H}]$, m/z 411.6) is presented as the base peak of the spectrum, with the quasi-molecular ion playing a minor role ($[\mathrm{M} - \mathrm{H}]$, m/z 205.6). This fits to the experiments of Figure 5.9 and to the observation in DESI experiments [86]. The authors state that the dimerization is linked to the concentration of the analyte. However, dimers are mostly formed in negative ion mode. Hence, this effect cannot be explained by the concentration only. Other studies [87] conclude that this effect is caused by the liquid-gas phase transition of these compounds, by the formation of hydrogen bonds and dispersion forces.

In Figure 5.11, mass spectra of ketoprofen (mono-isotopic mass 254.3 u) are displayed. The compound is detected in positive ion mode (Figure 5.11a) and negative ion mode (Figure 5.11b). Although both ibuprofen and ketoprofen belong to the profen family and the NSAIDs, their identified masses in the spectrum differ. As with ibuprofen, the quasi-molecular ion ($[\mathrm{M} + \mathrm{H}]$, m/z 255.5), water adducts ($[\mathrm{M} + \mathrm{H_2O}]$, m/z 272.5) and a dimer ($[2\,\mathrm{M} + \mathrm{H}]$, m/z 508.8) are observed. However, for ketoprofen, a carboxylic group is released from the dimer rather than the quasi-molecular ion ($[2\,\mathrm{M} - \mathrm{COOH}]$, m/z 463.6). In negative ion mode, the quasi-

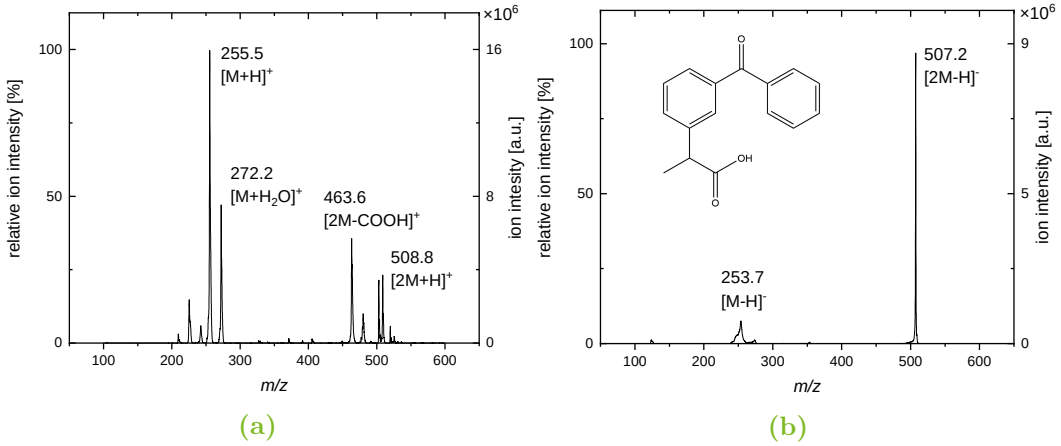

Figure 5.11: Mass spectra of ketoprofen, Figure 5.11a positive ion mode, Figure 5.11b negative ion mode ($m = 250\,\mathrm{ng}$). [52]

molecular ion ([M − H], *m/z* 253.7) is of minor relative abundance compared to the dimer ([2 M − H], *m/z* 507.2), matching the observation of ibuprofen. All in all, this set of analytes proofs the soft ionization capabilities for the FμTP without excessive fragmentation of the analytes.

5.5 Propazine for Method Comparison

In the beginning of this thesis, preliminary studies by Gilbert-López *et al.* [18] were presented as the motivation for more reproducible desorption substrates. Propazine will be finally taken as a model compound from these studies to evaluate the progress in this thesis and to compare previous laser desorption coupled with plasma ionization to this method. In Figure 5.12, a mass spectrum of propazine (monoisotopic mass 229.7 u) is shown. The molecule is present as a quasi-molecular ion ([M + H], *m/z* 230.4). Minor, unidentified fragments at *m/z* 146.3 and *m/z* 188.3, below 2 % of the base peak ion intensity, are detected. A dimer [2M + H] of the molecule is formed at *m/z* 460.4, below 4 % of the beak peak intensity. Comparing Figure 5.12 to the measurements carried out by Gilbert-López *et al.* [18], the relative abundance of fragments to the quasi-molecular ion peak has significantly decreased from 40 % with a desorbed amount of 200 ng in their studies to less than 1 % with a higher desorbed amount of 500 ng in this thesis. Therefore, less fragments are produced by this method. The mechanism may be related to the suppression of the coincident plasma in the DBD by modification of the duty cycle, as addressed

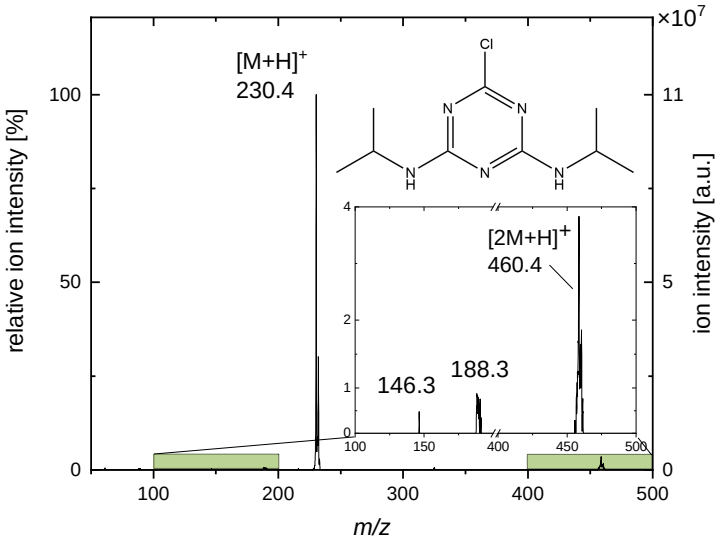

Figure 5.12: Mass spectrum of propazine ($m = 500\,\text{ng}$. [60])

in the fundamentals and in the works by Klute [58] as well as a more effective thermal desorption. In Figure 5.13, a calibration curve for propazine is shown. The

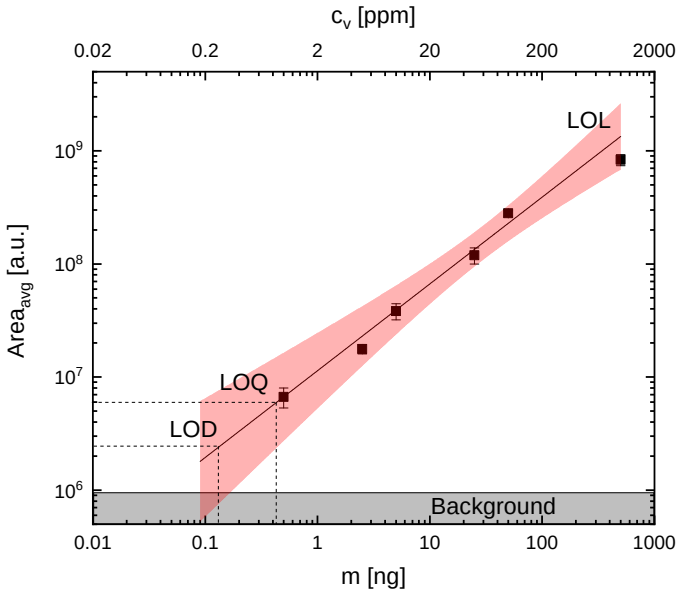

Figure 5.13: Calibration curve of propazine. [60]

limit of detection for propazine is 140 fg [60]. The method by Hubaux and Vos gives an extrapolated LOD that is approximately eight times higher. The LOQ of propazine is roughly 400 fg, the LOL is above 1 µg. Thus, the linear dynamic range is three orders of magnitude. In this sense, propazine can be detected as efficient as cholesterol. It is worth noting that Gilbert-López *et al.* [18] did not provide an

LOD, since there was no calibration performed. Instead, the authors reported a desorbed amount of 200 ng out of 1.23 µg of propazine applied to the surface. One reason for this was the spread of the sample fluid and the lack of reproducibility using black ink dots. This sample spread was limited in the method presented in this thesis by constructing cavities and a sandwich structure rather than ink dots for desorption.

6 Study on Laser Desorption from Tissue

Imaging of biological tissue is one of the most attractive applications of laser-based mass spectrometry. In previous conducted studies, fluorometric assays [88–90] were considered the gold standard technique to determine the spatial distribution of molecules in animal tissue. However, their applicability was bounded to fluorescent tags, thus limiting the method to low mass molecules and extracts. This demand has spurred molecular imaging in mass spectrometry. The most prominent methods are secondary ion mass spectrometry (SIMS) [91] and matrix-assisted laser desorption ionization (MALDI) [92]. SIMS uses a focused ion beam of a defined kinetic energy to sputter secondary particles from the tissue that are subsequently detected by the MS. MALDI sublimates vapor of a photosensitive dopant (a chemical matrix) on tissue placed on a microscope slide for thermal laser desorption and ionization, as stated in the fundamentals. The sample preparation requires vacuum conditions and profound knowledge in the matrix application to maintain the spatial resolution of the analyte on the tissue. In both methods, mostly neutral desorbate is ejected, which demands for a more efficient ionization.

In an attempt to improve imaging capabilities of MALDI, several branches have emerged. Two of them are the previously mentioned two-laser transmission mode MALDI (t-MALDI-2) [43] or atmospheric pressure MALDI (AP-MALDI) [93, 94]. In the former method, two lasers are used to increase the neutral-ion-yield. As a result, the spatial resolution can be improved to a subcellular level. In the latter, vacuum conditions are limited to the sample prepation only, and the experiment is carried out at atmospheric pressure. However, closed gas chambers are used for those experiments. As a result, the sucking property of the MS with flows of roughly 1 L/min may decrease the effective pressure level below atmospheric pressure again.

Commercially available imaging probes are the *SICRIT* device [95], the *AP-SMALDI10* MSI source [40, 96] or the *AP/MALDI(ng)UHR* source (*Mass Tech*,

USA) [97]. These sources are commonly used in AP-MALDI experiments and require fast mass spectrometers. In conclusion, MALDI remains a time-consuming and complex method: With a state-of-the-art high resolution ion trap mass spectrometer [43] several days are needed to fully screen a single image step-by-step with high spatial resolution.

In the following chapter, the results gained from the two previous chapters will be applied to the imaging of biological samples. Previously, compound droplets were placed in cavities of custom-made Copper-glass microscope slides for the desorption of analytical standards. This design was optimized for a free heat propagation on the Copper surface. In this sense, the thermal propagation is an advantageous property for standards, but not for imaging of tissue with the aim to achieve high spatial resolution. For that reason, a grid of Copper spots will be used on the glass slides, which will be discussed in the first section. Similar to the first chapter, the laser and tissue heating effects will be characterized for this application.

One reason that imaging on regular low-resolution mass spectrometers is not possible is that the mapping of each laser application to the ion signal requires initialization of individually recorded files. Further, each of this file usually takes several seconds for the initialization as the data is created and shifted from the internal computer of the MS to an external computer. This experimental time is particularly problematic for samples that are screened at ambient air, since room temperature and humidity facilitate the degradation of the biological sample. For this reason, the imaging process will be simplified by self-made software, which allows to screen the tissue in shorter time. As a result, this method works even on older and slower mass spectrometers, as long as the MS can be externally controlled.

In the final sections, different imaging modes as well as an image of cholesterol in mouse liver tissue will be shown and compared the morphology of the tissue. In contrast to MALDI, no matrix is needed for the desorption of the molecules, hence the sample preparation is simplified to the tissue cuts. All in all, no matrices, vacuum conditions or other tuning is needed in this method.

6.1 Design of the Desorption Substrates

A grid of Copper spots is placed on the glass slides known from section 4.1 (45 % rounded edges, 26 mm×76 mm×1 mm). The substrate preparation can be split

into three main processes. First, the Copper is sputtered on the glass. Second, lithography is used to produce circular spots. In contrast to the design for the analytical standards, the sputtering process is carried out before the lithography. The key element of this processing is to etch the Copper outside the spots, which are protected by the photo resist. Finally, the substrate is prepared for the tissue application by removing the residual coating from the substrate. The production steps for the substrate are shown in Figure 6.1 and will be described in the following.

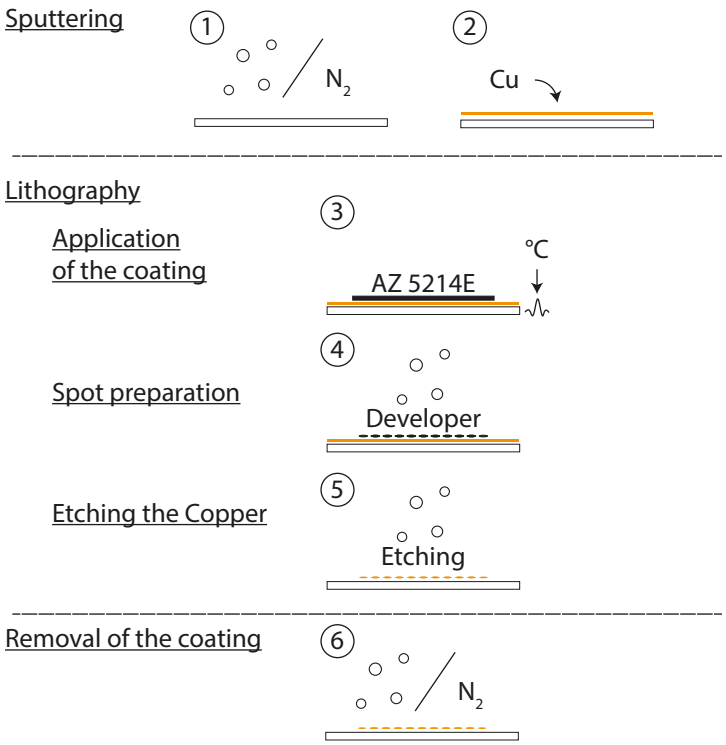

Figure 6.1: Schematic of the substrate preparation for a grid of Copper spots. The different steps are discussed in the text.

At first, the slides are bathed in peroxymonosulfuric acid at 80 °C for one hour, which increases the adhesion of the upcoming coating. Due to the improved substrate preparation, the Copper can be used both as an adherent and a structural layer using the same parameters as before. The rest of the sputtering process is identical to section 4.1. The resulting layer thickness of the Copper is (200 ± 20) nm.

The lithography steps are different from the previous design of the substrates. A positive tone photo-resist (*AZ 5214E, MicroChemicals GmbH*, Germany) is applied via spin coating. After spin coating, several seconds of cool down are required. The

substrate is subsequently soft-baked. After that, a mask is fixed in hard contact using the mask aligner. Finally, the substrate is exposed to light ($\lambda = 365\,\text{nm}$, using a Mercury-vapor lamp with a band-elimination filter). This light exposure increases the solubility in a developer in the next step. In contrast to the standard design, the substrate is finally developed without a post-exposure bake using diluted, metal-ion containing developer (*AZ 351B, MicroChemicals GmbH*, Germany), which removes the light-exposed regions. No post exposure bake is required as the positive tone photo-resist is removed with the developer. Finally, the spots are etched by removing the Copper that is not protected by the photo resist. For that purpose, sodium persulfate is used. However, a high concentration of the acid causes over-etching of the spots. In other words, the diameter of the Copper spots would decrease and the gap between the spots would grow. A hard bake is also not carried out to ensure sharp spot edges after development.

As stated, the residual coating is removed using organic solvents before tissue application. The settings used for the sputtering process and the lithography are summarized together with the substrate recipe for the standards in Table A.5 of the appendix.

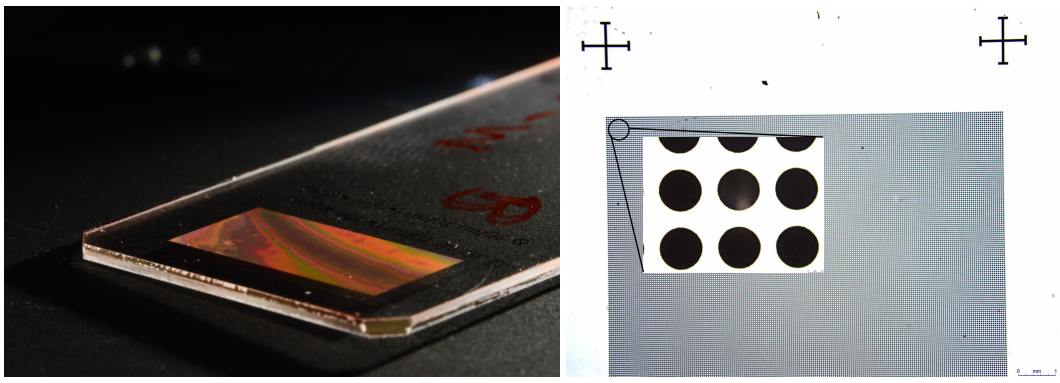

(a) (b)

Figure 6.2: Photos of the Figure 6.2a final substrate [53] and Figure 6.2b a detailed view of the Copper spots on the grid. Figure 6.2b is taken with transmitted light and a 1.25×/0.04 as well as a 100×/1.32 magnifying objective on a microscope *DM6 B, Leica Microsystems*, Germany. Exposure time 61 ms, Gain 2.8.

In Figure 6.2, the final substrate design and a detailed view of the Copper spots on the grid are shown. The calibration markers are used for a 3D offset correction with custom-made software. This correction accounts for tilts from the setup and fixes the laser focus as well as the 2D mapping and will be discussed in section 6.4. The dimensions of the Copper spots on the grid will be discussed in the next section.

The following two sections will deal with the laser-induced heating effects on the surface, first on plain Copper spots and then on tissue. A key element of these sections is the transition from cw to pulsed laser operation in an attempt to decrease the diameter of desorption.

The substrate will be vertically mounted to allow full screening, as seen in Figure 3.2. Therefore, the laser is applied from the glass side of the substrate that avoids laser focus correction for topological inhomogeneities of the tissue. Also, the 5× magnifying objective is used for the alignment of the laser, but a 40x magnifying objective is used to focus the laser on a single Copper spot.

6.2 Characterization of Laser Heating Effects

In general, the spatial resolution is linked to the spot size of the Copper spots on the grid. The following calculation estimates the radius of the Copper spots on the grid on the basis of the calibration curve of cholesterol from the cavities in Figure 5.3. The linear dynamic range from the limit of quantification (LOQ) to the limit of linearity (LOL) is three orders of magnitude [60], or

$$\frac{I_{\mathrm{LOQ}}}{I_{\mathrm{LOL}}} = \frac{1}{1000}.$$

The desorption radius can be estimated if the ion signal I linearly correlates to the area A, that is that their ratio is constant. This is a plausible assumption, as the desorption process is thermally-driven and the heat flow linearly correlates to the area.

If the area of the cavities is considered an upper limit and the area of the spots is considered a lower limit for desorption, similar to the ion intensities at the LOL and the LOQ of the calibration curve, their ratio is likewise given by

$$\frac{A_{\mathrm{Spot}}}{A_{\mathrm{Cavity}}} \approx \frac{I_{\mathrm{Spot}}}{I_{\mathrm{Cavity}}} = \frac{1}{1000}.$$

Together with the known inner radius $r_{\mathrm{Cavity}} = 0.5\,\mathrm{mm}$ of the cavities, the radius of

the spots r_{Spot} can be estimated by

$$\begin{aligned}
\frac{I}{A} &= \text{const.} \\
\frac{I_{\text{Cavity}}}{A_{\text{Cavity}}} &= \frac{I_{\text{Spot}}}{A_{\text{Spot}}} \\
\frac{I_{\text{Cavity}}}{A_{\text{Cavity}}} &= \frac{1}{1000}\,\frac{I_{\text{Cavity}}}{A_{\text{Spot}}} \\
\frac{1}{r^2_{\text{Cavity}}} &= \frac{1}{1000}\,\frac{1}{r^2_{\text{spot}}} \\
r_{\text{spot}} &= \frac{r_{\text{Cavity}}}{\sqrt{1000}}.
\end{aligned}$$

Hence, Copper spot diameters of roughly $d_{\text{spot}} = 2 \cdot r_{\text{spot}} \approx 30\,\mu\text{m}$ can be achieved. However, the laser spot also limits the Copper spot diameter. If smaller Copper spots than the laser spot were chosen, the laser would simply heat neighbored spots and thus artificially decrease the spatial resolution.

The laser spot using a 40x magnifying objective is shown in Figure 6.3. The spot

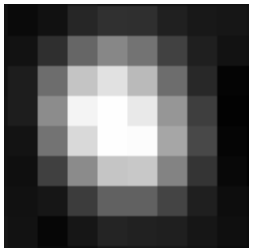

Figure 6.3: Spot of the focused laser beam of the ($\lambda_0 = 448\,\text{nm}$, $P = 3.5\,\text{W}$) diode laser using a 40x magnifying objective. [53]. CCD Camera: 1/3 in *S/W A1-Pro*, *Conrad Electronics*, Germany

diameter is identically calculated as in subsection 4.2.1 and equals $d_L \approx 48\,\mu\text{m}$. These two diameters can be matched by introducing a defined gap g between two Copper spots. This is shown in Figure 6.4. The comparison of these two diameters yields 48/2 µm-30/2 µm $\approx 10\,\mu\text{m}$ for the gap g_1 between the edges of the Copper spots. Copper spots with a diameter of $d_1 = 30\,\mu\text{m}$ and a gap of $g_2 = 5\,\mu\text{m}$ cannot be used, as the laser beam would cover two Copper spots on the substrate.

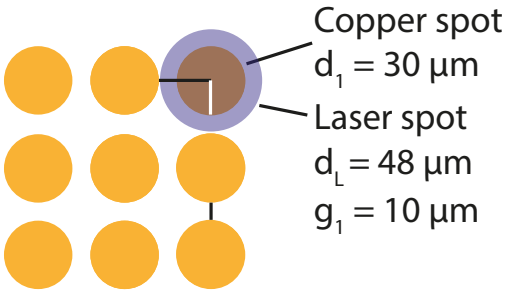

Figure 6.4: Schematic of the gap calculation using the diameter of the focused laser beam and the diameter of the Copper spot.

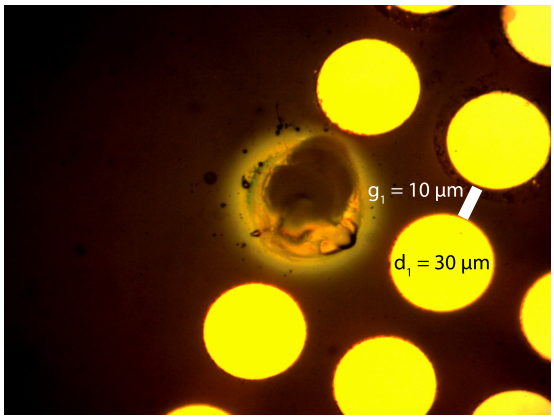

Figure 6.5: Microscope images of Copper spots with spot diameters $d_1 = 30\,\mu\text{m}$ and a gap $g_1 = 10\,\mu\text{m}$ on microscope glass slides after laser application for $t = 10\,\text{s}$. [53]

In Figure 6.5, a grid of Copper spots with a diameter of $d_1 = (30 \pm 1)\,\mu\text{m}$ and a gap of $g_1 = (10.0 \pm 0.4)\,\mu\text{m}$ are shown. The laser is applied to the center of a single Copper spot for $t = 10\,\text{s}$. In fact, laser application times per spot in imaging will be around $t = 1\,\text{s}$. Therefore, this application time is considered a worst-case-scenario to prove that the neighbored spots are not heated by the laser. No neighbored spots are visibly modified by the laser-induced heat. The thermal spread can be estimated from the faded ring around the spot, fitting to the previously carried out calculations. Inside the Copper spot, the black area relates to the laser application, similar to the cavities in chapter 4. Diffraction rings cannot be identified, as the spot is completely covered by the laser. The glass structure seems intact.

As the distance between two Copper spots is fixed by the laser spot diameter, smaller Copper spots are connected to larger gaps, thus desorb smaller amounts of the tissue without gaining better spatial resolution. Smaller gaps are linked to larger Copper spots likewise. However, even these larger Copper spots cannot be used

with a smaller gap, despite the sufficient diameter of the Copper spots. This will be shown in the following. Copper spots with a diameter of $d_2 = 50\,\mu m$ and gaps of

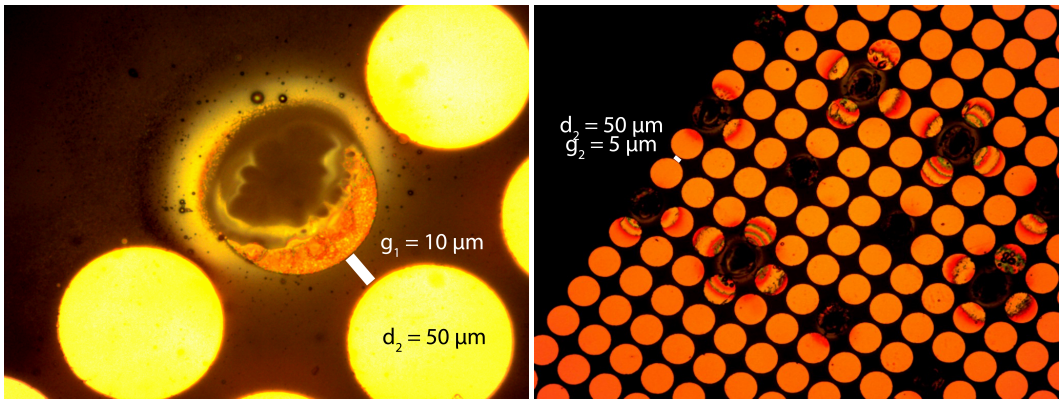

(a) (b)

Figure 6.6: Microscope images of Copper spots with spot diameters $d_2 = 50\,\mu m$ and different gaps g_i on microscope glass slides after laser application for $t = 10\,s$. Figure 6.6a $g_1 = 10\,\mu m$ and Figure 6.6b $g_2 = 5\,\mu m$. [53]

$g_1 = 10\,\mu m$ and $g_2 = 5\,\mu m$ are shown in Figure 6.6a, respectively Figure 6.6b. The laser is applied to the Copper spot for $t = 10\,s$, equal to the experimental conditions of Figure 6.5. Neighbored spots with a gap of $g_1 = 10\,\mu m$ should not show any surface modification. In Figure 6.6a, no surface modifications such as diffraction rings can be observed on the neighbored spots, matching to the previous results. However, the red area inside the laser-applied Copper spot indicates that these rings coincide on the laser-applied spot.

In Figure 6.6b, Copper spots with a diameter of $d_2 = 50\,\mu m$ and a gap of $g_1 = 5\,\mu m$ are shown. This configuration should not show surface modifications on neighbored Copper spots either. Despite this assumption, the neighbored spots show diffraction rings next to the heated Copper spot. These rings emerge from heat propagation through the glass to the next Copper spot. Diagonally neighbored spots with a gap of $g_3 = \sqrt{2} \cdot (d_2 + g_2) - d_2 \approx 28\,\mu m$ show no surface modification. In conclusion, the gap of $g_1 = 10\,\mu m$ is optimal to limit the thermal propagation and to support the thermal confinement. The $d_1 = 30\,\mu m$ spots are considered to provide the best possible spatial resolution.

6.3 Characterization of Tissue Heating Effects

The heat transfer coefficient of the tissue is assumingly lower than the thermally isolating glass. Thus, the heat will propagate through the tissue rather than the glass due to the lower thermal resistance. As a consequence, the desorption area increases again. As the thermal resistances of the tissue, glass and Copper are constant, there are only two ways to minimize the thermal spread. Either the gap between two Copper spots is increased or the laser application time is reduced. The former case was discussed already and results in a lower spatial resolution. In the latter, the application time can be controlled by changing from continuous to pulsed laser operation. In fact, this type of thermal confinement is used in MALDI as well, as nanosecond or femtosecond pulsed lasers are used. That way, each laser pulse is applied on a similar time scale as the thermal propagation. In other words, the heat propagation is pushed towards thermal disequilibrium. However, the pulsed operation of diode lasers comes with some drawbacks, which will be discussed in the following. On the basis of these results, the optimal pulsing conditions will be derived.

A laser pulse of a 3.5 W blue diode laser is shown in Figure 6.7. The laser pulse

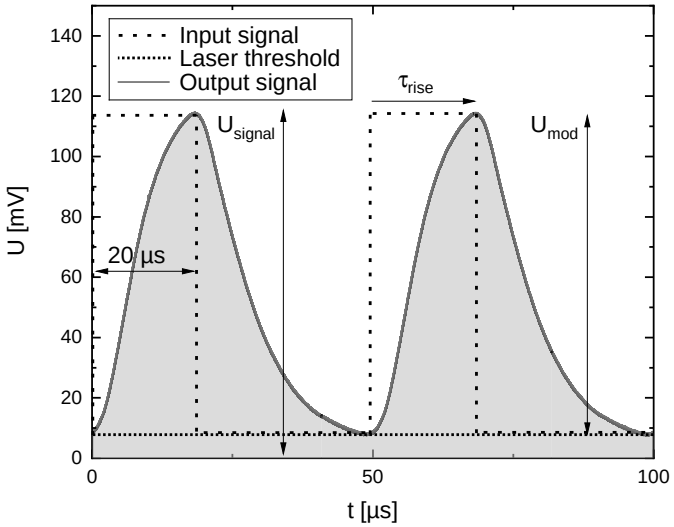

Figure 6.7: Signal course of the pulsed, blue diode laser ($\lambda_0 = 448\,\mathrm{nm}$, $P = 3.5\,\mathrm{W}$) at $f = 20\,\mathrm{kHz}$ input pulse frequency with a pulse width of $w_{20\,\mathrm{kHz}} = 20\,\mu\mathrm{s}$ (dotted). The signal amplitude U_{signal}, the modulation amplitude U_{mod} and the rise time τ_{rise} are highlighted. An average of 32 signals is taken with a digital phosphor oscilloscope (*DPO2012, Tektronix*, USA). [53]

output signal is shown at an input pulse frequency of $f = 20\,\mathrm{kHz}$ with pulse widths

of $w_{20\,\mathrm{kHz}} = 20\,\mu\mathrm{s}$ (duty cycle of 40 : 60). The choice of these working parameters in imaging will be justified by the end of this section. The modulation amplitude U_{mod} rises from the laser threshold to the maximum signal amplitude U_{signal}. The rise time of the pulse is $\tau_{\mathrm{rise}} = (15 \pm 3)\,\mu\mathrm{s}$, measured from 10 % to 90 % of the signal amplitude U_{signal}. The input pulse signals are indicated as well, proving that the diode laser and its controller cause a delay to the output signal.

The maximum signal amplitude of a laser pulse roughly matches to the modulation amplitude for pulse frequencies up to 20 kHz. With higher pulse frequencies or smaller pulse widths, the modulation amplitude of this diode laser decreases, as both the rise and the fall time of each output pulse are longer than the total length of the input pulse. This limitation is related to the diode laser controller and the diode laser itself. As a result, the signal does not fall down to the noise level, but is intercepted by the next input pulse. In extreme cases, high frequencies of pulsed diode lasers basically coalesce into a cw operation. In conclusion, high pulse frequencies of the diode lasers are linked to a decrease in the output power. In terms of imaging, this effect translates into a constant heating of the surface. This result is unwanted, as a constant heating increases the fragmentation of the desorbate.

The bandwidth of diode lasers is marked by the 3 dB or 70.7 % level. This bandwidth of the signal amplitude is measured in cw laser operation. In Figure 6.8a, the signal

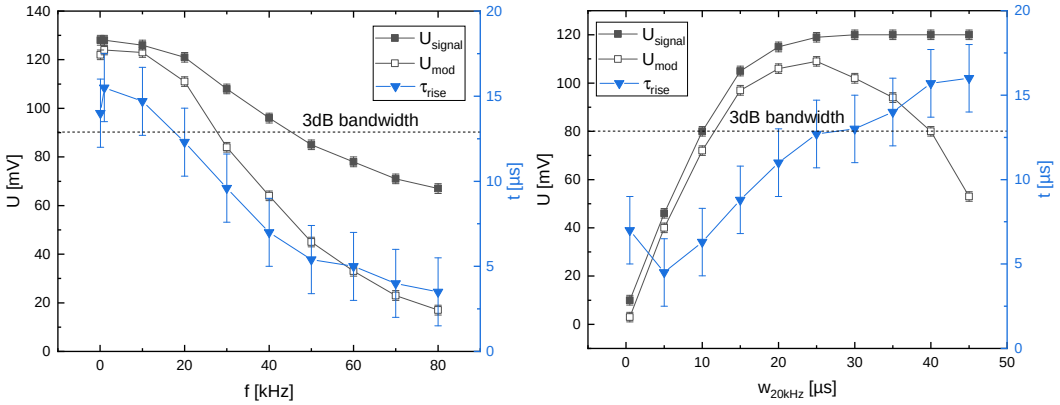

Figure 6.8: The signal amplitude U_{signal}, modulation amplitude U_{mod} and signal rise time τ_{rise} of the pulsed diode laser ($\lambda_0 = 448\,\mathrm{nm}$, $P = 3.5\,\mathrm{W}$) Figure 6.8a with increasing pulse frequency at a constant duty cycle of 50:50 and Figure 6.8b increasing pulse width (duty cycle). The signal is averaged over 32 signals. [53]

U_{signal} and the modulation amplitude U_{mod} as well as the rise time τ_{rise} of each laser

pulse are shown for an increasing laser pulse frequency, but a constant duty cycle of 50 : 50. The signal amplitude is taken peak-to-peak.

The 3 dB level is reached at approximately 30 kHz. Below 30 kHz, the rise time of the diode laser is shorter than the input pulse width, which results in a high modulation amplitude. Above 30 kHz, the modulation amplitude of the diode laser significantly decreases, as the rise time of each output pulse is longer than the input pulse. As a consequence, both the modulation amplitude and the signal amplitude further decrease, as the output pulse is cut before reaching the maximum amplitude of the signal. However, the baseline of the signal also increases, as the fall time of the output pulse is cut as well. As a result, the modulation amplitude and signal amplitude do not fall with the same slope.

In Figure 6.8b, the pulse width (or duty cycle) is varied at a pulse frequency of 20 kHz. The 3 dB level is indicated by a dashed line, which crosses the modulation amplitude at 12 µs pulse width and 40 µs pulse width for the same reasons as before. In the former case, a significant decrease in the rise time and both amplitudes is observed. In the latter case, this effect results in a continuous-wave operation. This is the reason why the signal amplitude is constant, whereas the modulation amplitude decreases. The rise time is relatively constant, considering the error and the scale above the 3 dB level.

Megahertz-pulsed diode lasers with a wavelength in the UV-Vis are commercially available [98], but only offer laser output powers in the milliwatt range and fixed pulse widths. Therefore, these diode lasers as well as diode-pumped Nd:YAG lasers suffer from the same issues as the used blue diode laser. Other diode lasers with similar output powers to the blue diode lasers can be pulsed up to 50 kHz.

These results are now linked to the desorption area on pure Copper-glass slides with biological tissue. These slides allow to evaluate the impact of the laser pulse frequency and width, which influence the laser-induced heat propagation and thus the desorption area on the tissue.

In Figure 6.9, the diameter of desorption d_{spot} is measured with a microscope for different pulse frequencies and pulse widths. Close to continuous-wave operation at 2 Hz, a diameter of (95 ± 5) µm is recorded. The diameter decreases linearly with increasing pulse frequency for several hundreds of hertz, but stagnates above 2 kHz at a diameter of 50 µm. It is therefore assumed that the pulse width, which influences the total application time, may decrease the desorption diameter.

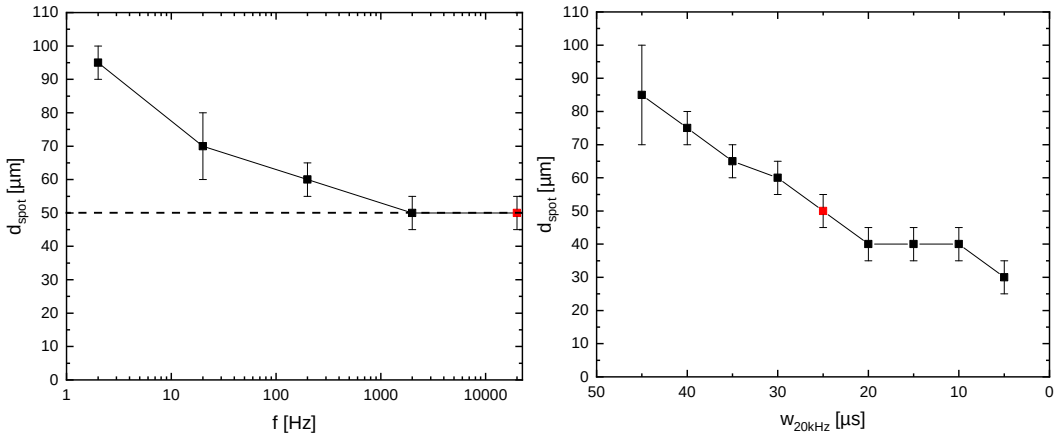

Figure 6.9: Diameter of desorption d_{spot} Figure 6.9a with increasing pulse frequencies f (duty cycle 50:50) and Figure 6.9b increasing pulse widths $w_{20\,\text{kHz}}$ at a fixed frequency of 20 kHz. The highlighted point marks the same experimental conditions. Both figures are directed from near-cw to pulsed operation. [53]

Therefore, laser pulses shorter than 50 µs at a pulse frequency of 20 kHz are evaluated. For that reason, the pulse width is varied from 46 µs down to 5 µs at a fixed pulse frequency of 20 kHz. With shorter pulses, the desorption diameter decreases linearly from (85 ± 15) µm down to (30 ± 5) µm.

The final experimental parameters are a pulse frequency of 20 kHz with a pulse width of 20 µs (duty cycle 40 : 60). Shorter pulse widths than 20 µs decrease the desorption diameter, but are related to a decreased modulation amplitude and thus a drift towards cw laser operation, as discussed in Figure 6.7 and Figure 6.8.

In imaging, the laser will be applied to each Copper spot for 1 s. However, the effective laser application time is only $0.4 \cdot 1\,\text{s} = 0.4\,\text{s}$ in which $\frac{0.4\,\text{s}}{20\,\mu\text{s}} = 20000$ pulses are applied to each spot. Based on the previously shown cw-power meter measurements in Figure 4.3 and the spot seen in Figure 6.3, the cw laser intensity is $500\,\text{W/mm}^2$. Considering the pulses with a duty cycle of 40:60, the pulsed laser intensity is only $0.4 \times 500\,\text{W/mm}^2 = 200\,\text{W/mm}^2$.

6.4 Imaging and Post Processing Software

This section will deal with the concepts and ideas of the screening and post processing scripts that are required to screen the tissue. These scripts are shared on GitHub

(`https://github.com/alexk93/imaging`) as part of a publication [53] and this thesis. A flow chart of the concepts and ideas of the LabVIEW-based software is shown in Figure 6.10.

After initialization of the program and the electronical stage, every image requires to set a starting point and to read calibration markers. These calibration markers are used for a substrate leveling, similar to 3D printing. This leveling is necessary, as the grid of Copper spots is not perfectly aligned to the substrate. Also, the setup includes tilts, whose dimensions are similar to the diameter of a Copper spot. Before beginning a measurement, other experimental parameters such as the step width need to be adjusted to the configuration of the Copper grid.

In order to start a measurement, the laser shutter needs to be closed and the laser needs to be set to the aforementioned experimental conditions. The MS begins with the measurement after receiving a start pulse through the start-in socket, as stated in section 3.2. Its *XCalibur* software performs the data handling with a defined instrument method and experimental duration. The sample on the Copper grid is screened in lines, either spot-by-spot or by moving the stage at a constant speed. Each of such a line is recorded in a single file.

The presented algorithm requires precise synchronization of the MS and the screening software. The following considerations need to fit to the settings in the *XCalibur* software for synchronization of the MS to the proposed *LabVIEW* software. With a region of interest (ROI) of 5 mm · 5 mm, 5000 µm / ([30 + 10] µm) = 125 lines need to be screened per image. With a laser application time of 1 s, a wait time of 0.5 s between spots and 4 s tolerance for the MS to settle, an experimental duration of (125 spots · 1.5 s/spot + 4 s) ≈ 3.2 min per line are needed.

After receiving the start pulse, the current position of the stage is stored into a mapping table, as the data of the MS needs to be allocated to the absolute position of the Copper spots on the grid after the experiment. For that reason, these positions are stored into the local memory of the stage and afterwards read from its memory buffer, as an online read-out is not directly possible.

The laser is subsequently applied to these Copper spots, whose shutter is opened with a TTL signal. The steps from the spot allocation to the laser application iterate for each point on a defined ROI. If the stage moves to the next spot or a new line, a linear offset correction will be performed on all three axis to level the

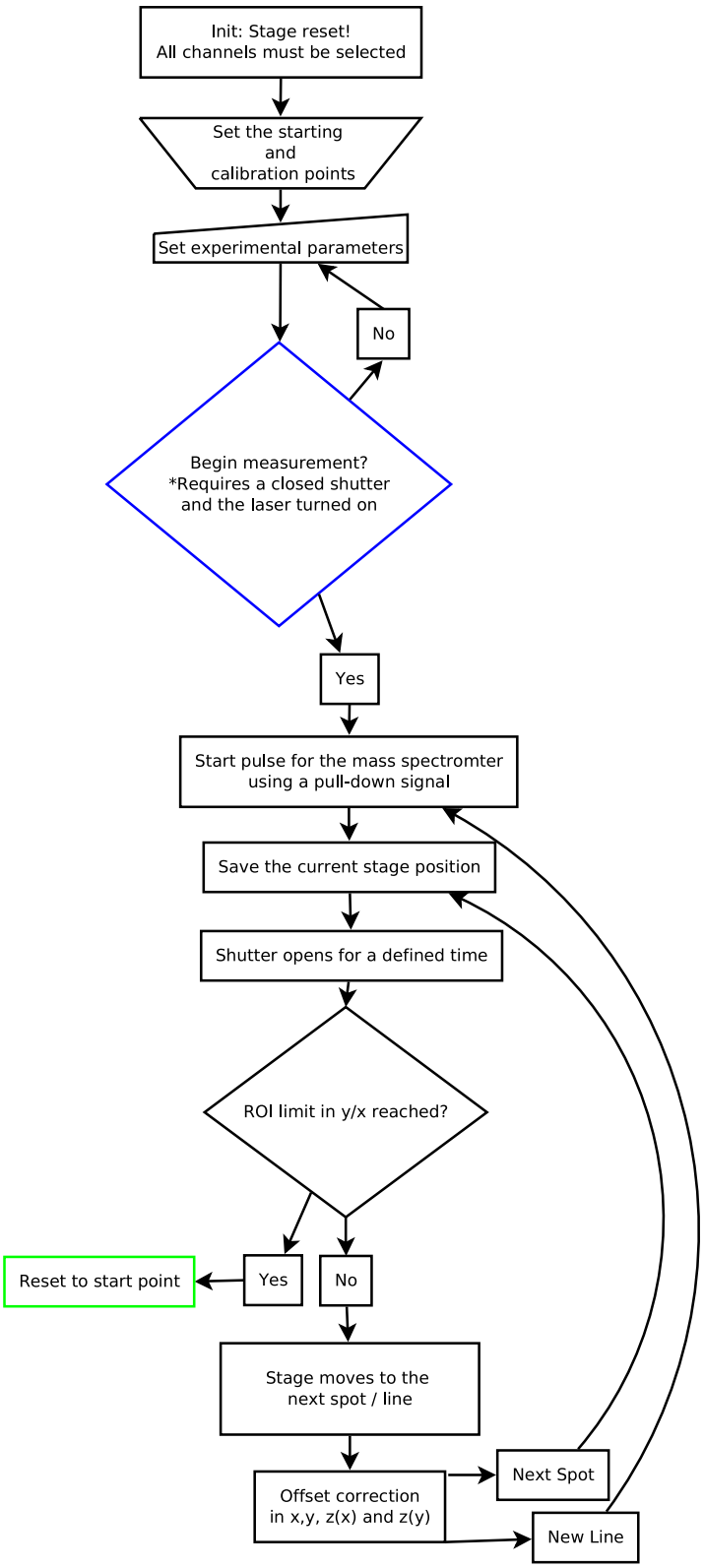

Figure 6.10: Flow chart of the screening procedure (based on Dia Portable, vers. 0.97.2). [53]

substrate, including the stabilization of the laser focus. A typical offset correction on the complete screened tissue is about $(32 \pm 6)\,\mu m$ per axis.

If a new line begins, another start pulse is send to the MS. Each axis is screened unidirectional to avoid hysteresis effects from the stage movement. As a consequence, the total positioning error is reduced by the unidirectional movement and the offset correction to 0.5 % positioning error on the scanning axis. The positioning error for the perpendicular axis is estimated below 0.04 %. Thus, the propagated positioning error at a traveling distance of 5 mm on the scanning axis is 25 µm, the error on the axis perpendicular to the scanning axis is 10 µm.

In total, the experiment takes $(3.2\,\text{min/line} \cdot 125\ \text{lines}) \approx 6.7\,\text{h}$. The benefit of the algorithm is proven by comparing this duration to traditional imaging methods, in which each laser application is linked to a single output file. In traditional imaging, 6 s are required for file processing of each file and each measurement must be at least 6 s long. Thus, for the same amount of spots without the presented algorithm, more than two days would be required for the same experiment. As a consequence, the degradation of the biological sample would significantly increase.

After the screening of the ROI is finished, the stage resets to the starting position. Finally, the MS automatically shuts down after the complete experiment has ended. The points of a single line need to be unfolded as part of data post processing.

In post processing, the data is handled by an algorithm, whose flow chart is shown in Figure 6.11.

Initially, the vendor-specific *.RAW*-files from the MS are translated into ASCII files (*.tsv*) using the *MSFileReader* (both *Thermo Fisher Scientific*, USA) combined with a python-based script named *pymsfilereader*, which is available online (`https://github.com/frallain/pymsfilereader`). Such a *.RAW*-file for a single line contains commonly more than 10000 spectra. The *pymsfilereader* is further adapted in a way that it reads the masses from each spectrum in the file. The given intensities are then summed into the total ion current. The output file thus includes total ion chromatograms (TICs) for more than 1.3 million spectra of a single image.

These spectra are automatically interpreted by an integration tool. This tool requires four main parameters: The gap between spots, the total signal time including the gap, the uncertainty of the method, given in number of spectra, and the signal threshold given as ion intensity in arbitrary units. For this experiment, the MS

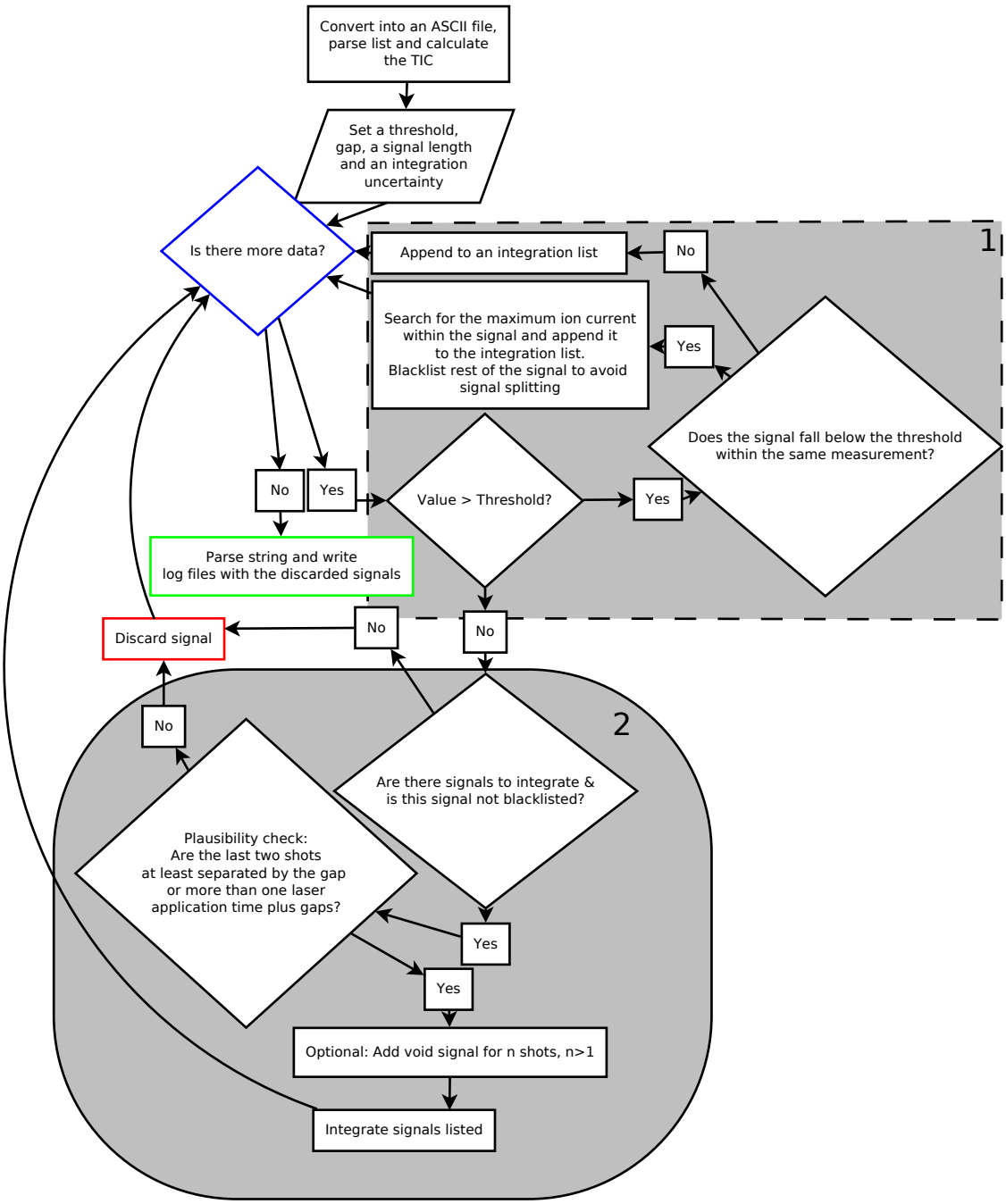

Figure 6.11: Flow chart of the data post processing (based on Dia Portable, vers. 0.97.2). [53]

achieves a sampling rate of roughly 60 Hz. In spot-by-spot scanning, a gap of 27 spectra, a total signal time including the gap of 60+27=87 spectra, and a deviation of 3 spectra is taken. The ion intensity threshold is commonly higher than the plasma noise, but lower than the minimum signal in the experiment. The ion intensity threshold for this experiment is 60000 a.u. The integration tool can identify signals, which are four times higher than the plasma noise.

The tool uses these four parameters in two main if-statements to decide if the current value can be considered a valid signal. First, the value needs to constantly exceed the aforementioned threshold. All intensities that constantly exceed the threshold are stored into an integration list. If the signal falls below the defined threshold within the same laser application to a single Copper spot, it is considered ambiguous and processed in another sub step. In that case, the maximum ion current measured on this spot is taken as a representative intensity for the specific spot and stored into the integration list as well. The other ion intensities are blacklisted to avoid that a single signal is considered as two separate signals. This approach usually causes a neglectable deviation between the integrated ion intensity and the maximum ion intensity taken for these ambiguous signals. For that reason, the edges of the image are slightly blurred. A disadvantage of the mandatory blacklisting is that the algorithm tends to use the aforementioned maximum ion current rather than properly integrating every valid signal that constantly exceeds the threshold. For that reason, the reconstructed image may be shifted towards lower ion intensities.

The second if-statement of the algorithm will be applied if the threshold is not reached in the next iteration. This statement checks if the listed signal is plausible. For that reason, the algorithm initially compares the integration list with the blacklist. Further, every signal needs to be separated at least by the gap between two spots. If two signals are more than a single laser application plus the gaps apart, the intensity at this position is filled with a void signal. Finally, the script integrates the signal and stores all results into a single file.

The discarded signals are also stored into a file. A simple batch script is sufficient to iterate through all the files in a folder.

6.5 Comparison of Two Imaging Modes: Spot-by-Spot and Line Scanning

The functionality of the integration tool will be shown practically on data in the following. The Copper spots are screened spot-by-spot and in line scanning at a constant speed. Cholesterol is measured in selected ion monitoring (SIM) on the quadrupole mass spectrometer with a mass range of $\delta m/z$ 368.6 - 370.1 and a sampling rate of 60 Hz (cycle time 10 ms). The experiment is taken on the third quadrupole (Q3MS) with a peak width of 0.6 (FWHM) at m/z 369. No internal averaging or micro scans are carried out. The diode laser is pulsed at a frequency of 20 kHz with a duty cycle of 40:60 and an estimated laser intensity of 200 W/mm^2. The laser is applied to the surface for 1 s each spot.

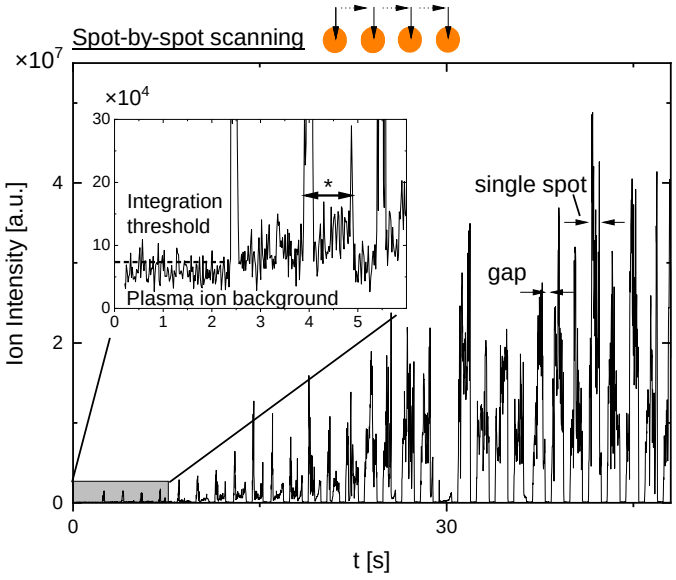

Figure 6.12: Extracted ion mass chromatograms (m/z 368.6 to m/z 370.1) of cholesterol using spot-by-spot scanning. The application time on a single spot, the gap between two spots, the integration threshold and the plasma ion background are indicated as well. [53]

In Figure 6.12, the chromatogram of a single line on the Copper grid is shown for spot-by-spot scanning. A single laser application on a Copper spot as well as the gap between two spots can be identified. The integration threshold used for the integration tool is indicated as well that highlights the issue with ambiguous signals (marked with an asterisk) falling below the threshold within a single application. All signals undergo the plausibility test to validate if the signal is indeed separated

by the gap.

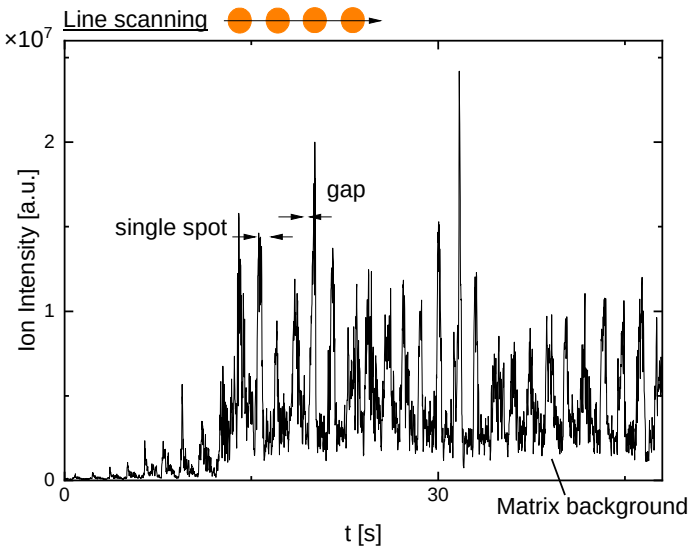

Figure 6.13: Extracted ion mass chromatograms (m/z 368.6 to m/z 370.1) of cholesterol using line scanning. The application time on a single spot, the gap between two spots and the matrix backgrounds are indicated as well. [53]

In Figure 6.13, the chromatogram of a different line on the Copper grid is shown for line scanning. The scan speed is 30 µm/s, matching to the dwell time on each Copper spot. The laser application and the gap between two spots are highlighted again. In contrast to Figure 6.12, a matrix background is observed in between two Copper spots. This matrix background is linked to the absorption of laser light by the tissue, as the laser shutter is not closed as the stage moves the substrate.

The ion current in spot-by-spot scanning is higher than in line scanning. This difference relates to the dwell time and the thermal propagation on a Copper spot, as the laser position is fixed in spot-by-spot scanning, whereas the laser is applied to different parts of the same Copper spot in line scanning. For the same reason, the spot-by-spot scanning sometimes reveals an initial peak and a second lower peak within the same spot application. The initial peak emerges from the desorption of the molecules from the center of the laser application. However, the second lower peak relates to the desorption from the outer regions of the laser application. In line scanning, the laser is constantly applied to a new part of the tissue and thus provides a more constant signal. It is further worth noting that if a Copper spot is not fully covered by the tissue, the edge of the tissue will appear faded in the reconstructed image, regardless of the scanning mode.

The sampling rate of the MS is 60 Hz. Thus, with a scan speed of 30 µm/s, $30\,\mu m/(30\,\mu m/s \times \frac{1}{60\,Hz}) = 60$ spectra are recorded per Copper spot. In this sense, a higher scan speed decreases the total experimental duration, but also the amount of recorded spectra for a single spot and therefore the accuracy of the imaging. At scan speeds below 30 µm/s, the number of spectra recorded per spot would increase, but the experiment would take longer as well without increasing the spatial resolution or the accuracy of the image. All in all, the measurement time, the sampling rate, the spatial resolution and the ion intensity are parameters that are cross-correlated and impact the results.

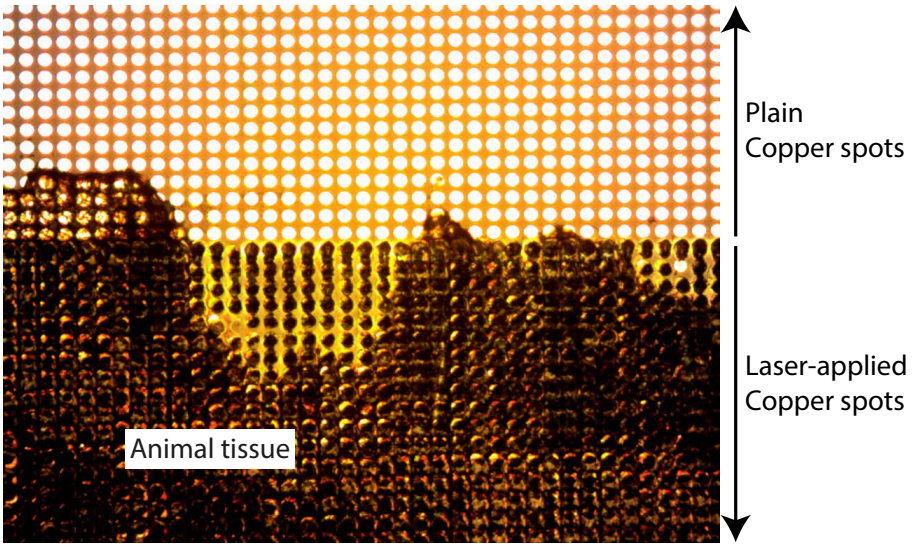

Figure 6.14: Microscope image of a screened substrate. The image shows plain Copper spots, tissue on Copper spots and Copper spots with and without tissue after laser application. [53]

In Figure 6.14, a microscope image of the spot-by-spot screened tissue is shown. Each row provides an extracted ion mass chromatogram similar to Figure 6.12 with identical settings of the experiment. The upper part of the image shows plain, intact Copper spots. The edges of the tissue can be seen as well. Copper spots after laser application with and without tissue can be identified from the picture.

6.6 Imaging of Cholesterol in Mouse Liver Tissue

In general, almost every imaging of molecules in biological tissue is interesting for the scientific community. Within the scope of this thesis, proteins [99] and sphingolipids [100, 101] have been intensively studied in previous works. In contrast,

sterols such as free cholesterol [102, 103] have not been intensively monitored, especially not at ambient air. Monitoring of free cholesterol is a complex, yet important topic, as the compound is assumed to take a predominant role in the evolution of several diseases, as outlined in the previous chapter. Furthermore, a target analysis of cholesterol was recently demanded by Cologna [104]. The author presented MALDI and DESI as the only methods for the imaging of cholesterol.

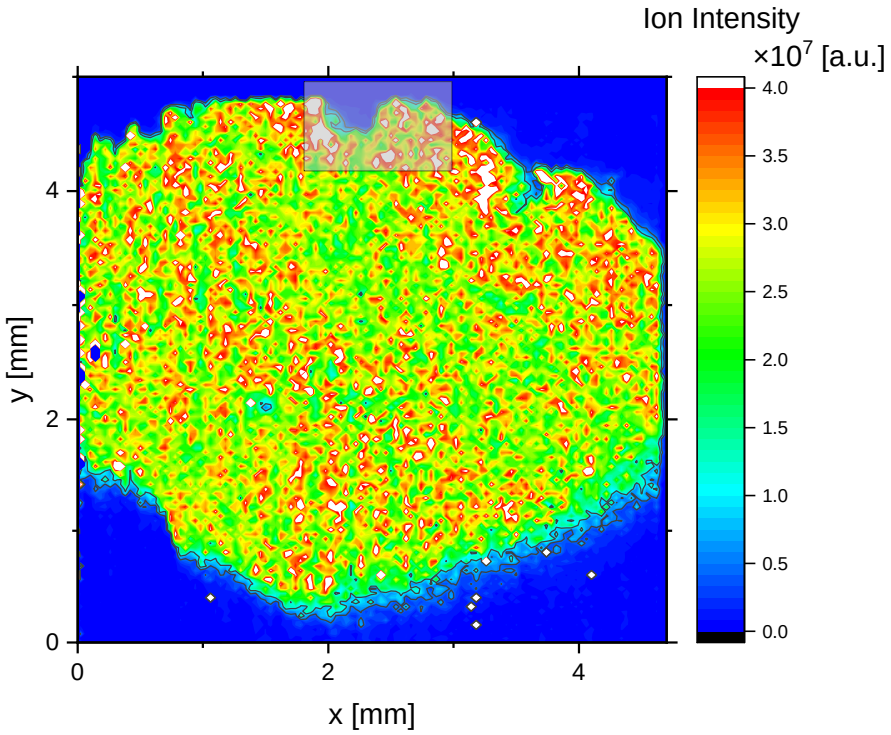

Figure 6.15: Reconstructed image of mouse liver tissue scanned spot-by-spot. [53]

In Figure 6.15, a spot-by-spot scanned image of cholesterol on mouse liver tissue is shown. As the cell membrane includes cholesterol and every cell synthesizes cholesterol, the reconstructed image is homogeneous. Several regions of low cholesterol intensities (blue) and high intensities (white) can be nevertheless identified. The low intensities are either related to the anatomy of the organ or rips in the tissue. The high intensities are either aggregations of cholesterol or artifacts outside the tissue. In the lower right part of the image, a faded edge of the tissue can be observed. This part of the tissue is thinner and thus provides less ion signal. The grey area in the reconstructed image can be allocated to Figure 6.14. The morphology is further validated from a microscope image of the screened tissue, as seen in Figure 6.16, which proves the accuracy of the processing algorithm.

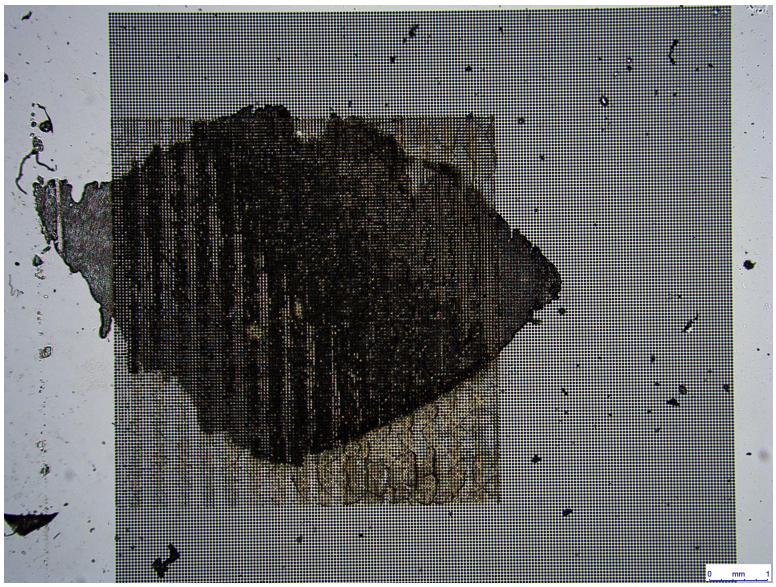

Figure 6.16: Screened image of mouse liver tissue. *DM6 B, Leica Microsystems*, Germany. Taken with transmitted light and a 1.25× magnifying objective. Exposure time 61 ms, Gain 2.8. [53]

Imaging in mass spectrometry resolves from subcellular level of 100 nm in NanoSIMS [105] to 500 µm [94, 106] using DESI. This large range partly relates to the working pressure of these methods. In general, vacuum conditions allow imaging on cellular level.

In ambient air laser desorption, better spatial resolution is achieved with a bigger numerical aperture of the optical elements or shorter laser pulses, which decrease the laser spot diameter. Another option is using a controlled atmosphere, which decreases the ion background. Other techniques at ambient air use chemical matrices, external heating or bias potentials. Several ambient air mass spectrometry imaging methods as well as this method, which is called diode laser desorption, plasma ionization mass spectrometry Imaging (DLD-PI MSI), are summarized in Table 6.1.

Early DESI results resolved below 500 µm×500 µm [94]. One reason for the low spatial resolution are the sprayed ions, which are hard to focus. More recent publications [108] estimate the spatial resolution by cross-correlating the scan speed in imaging and the sampling rate of the mass spectrometer. Together with concentric solvent sprays and smaller emitters of the electrosprays, the authors state to resolve 40 µm to 60 µm.

AP-MALDI uses a chemical matrix, external heating and a bias potential on the

Table 6.1: Comparison of ambient air imaging methods in mass spectrometry. Matrix and heat are abbreviated terms for a chemical matrix and an external heating on the substrate. [53]

Method	Desorption	Ionization	Matrix	Heat	Commercialized	Desorption area / (µm×µm)	Reference
DESI	Spray	ESI	No	No	No	<500×500	[94]
AP-MALDI	UV laser ablation	MALDI	Yes	Yes	Yes	1.4×1.4	[40]
LTP	Plasma	Plasma	No	No	No	250×250	[4]
LD-LTP	UV laser	Plasma	Yes	Yes	No	25×25	[107]
DLD-PI MSI	Blue laser diode	Plasma	No	No	No	40×40	this work

substrate and is often placed in a closed gas chamber. As stated at the beginning of this chapter, this closed gas chamber together with the sucking property of the MS may decrease the working pressure to a prevacuum, which can explain the better spatial resolution.

Other ambient air methods, either spray- or plasma-based, share the aforementioned drawback that their resolution decreases by the focusing ability of the ions, both on the sample and the inlet of the MS. Therefore, these methods were coupled with either cw or pulsed UV lasers, resulting in recently published LD-LTP variants used for the detection of plant metabolites [109] or lipids [107].

DLD-PI MSI uses laser desorption and plasma ionization that does not depend on any external sources and can be used with slower and older ion trap or quadrupole mass spectrometers in combination with the presented algorithms. However, the simplified operation at atmospheric pressure and ambient air comes with an increased ion background, which worsens the spatial resolution. This method was used and optimized for the target analysis of cholesterol on liver tissue. Nevertheless, the applicability of this method is not limited to this compound and will be used on different analytes in future experiments.

7 Limits of the Method

This chapter will compare both experimental configurations as seen in Figures 3.1 and 3.2 with respect to the correlation of the decrease rates and the particle densities of cholesterol and propazine in laser desorption. In these configurations, the substrate was set perpendicular and parallel to the inlet of the MS.

In ambient air, the robustness of a method is a quality factor. Therefore, the limits of the method for the desorption and the ionization are evaluated separately. This will prove on the one hand whether guided transport of the particles is required, for instance by using a heated transfer capillary. On the other hand, the need of external ion focusing will be discussed. In that manner, inherent electric fields from the ion source to the inlet of the MS and to the substrate will be addressed. In addition, a bias potential will be used on the substrate to tune these electric fields. The results will be compared to MALDI, in which this tuning is mandatory. Related experiments will also cover charge effects on the substrate caused by the ejected ions, which help to estimate the ion loss to the substrate.

For the following sections, substrates with cavities are used, as well as the 5× magnifying objective.

7.1 Correlation of Physical Parameters in both Experimental Setups

The signal course is investigated by comparing two model analytes, cholesterol and propazine, using the initial experimental setup of Figure 3.1 in which the substrate is parallel to the inlet of the MS. The chromatograms are taken with the AGC targeted at maximum number of ions at 5×10^7 and a cut-off injection time of 20 ms. The mass windows are $\delta m/z$ 220-240 for propazine and $\delta m/z$ 367-371 for cholesterol.

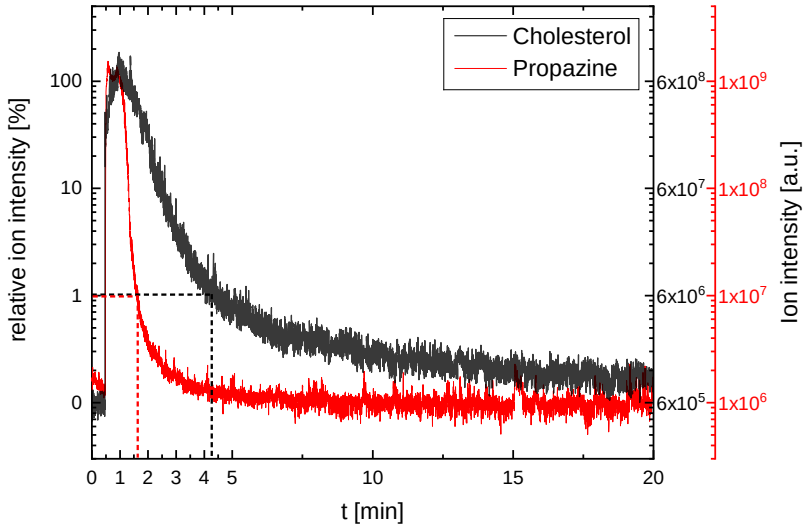

Figure 7.1: Extracted-ion chromatograms (XICs) of cholesterol and propazine, normalized for the maximum intensity of the respective compounds ($m_{\text{propazine}} = 0.5\,\mu\text{g}$, $m_{\text{cholesterol}} = 0.55\,\mu\text{g}$). [60]

In Figure 7.1, the XICs of cholesterol (m/z 369.8) and propazine (m/z 230.4) are shown, normalized for the beginning of the respective falling edges with roughly the same amount of both analytes. As known from section 4.4, both compounds efficiently desorb at $12\,\text{W/mm}^2$, respectively $16\,\text{W/mm}^2$ on the same time scale. Cholesterol, however, is detected in the spectrum for at least 15 min, while propazine is only detected up to three minutes. The loss of ions on the falling edge is taken as an estimation for the decrease rate of the desorbate. The fixed amount of ions $\delta N = 100$ detected over a time interval δt can be read for both compounds from the dashed lines of Figure 7.1:

$$\frac{\delta N}{\delta t} \approx \begin{cases} \frac{100}{50\,\text{s}} & = 2.0\,\text{s}^{-1} \text{ for propazine} \\ \frac{100}{200\,\text{s}} & = 0.5\,\text{s}^{-1} \text{ for cholesterol.} \end{cases}$$

For simplification, it is assumed that the particles are normally distributed in front of the inlet and the particle flow to the inlet equally depends on thermal effects, collisions and ionization as well as detection efficiencies for both compounds. Also, it is assumed that the ion current linearly correlates to the mass concentration, as justified by calibration curves, and thus to the particle density.

By comparing cholesterol to propazine, propazine is approximately four times more transient in ambient air conditions than cholesterol. However, this effect does not

change the LOD of a compound, as cholesterol and propazine have shown similar LODs (see subsection 5.2.1 and section 5.5).

These decrease rates are compared to the particle densities of cholesterol and propazine in the following. To estimate the particle density of a desorbate, it is assumed that the particles are ejected in a sphere above the cavity with a radius of $r = 500\,\mu\text{m}$. It is also assumed that all particles are desorbed from a mono-layer of the substrate to neglect non-linearity effects in desorption. With the volume V of the sphere being $V = \frac{4}{3}\pi r^3$ and an amount of $m = 0.55\,\mu\text{g}$ for cholesterol, the particle density of the desorbate n can be estimated using ideal gas theory:

$$n = \frac{N}{V} = \frac{{}^{m}/_{M} \times \mathrm{N_A}}{{}^{4}/_{3}\,\pi r^3}$$

with the number of the particles N of the desorbate, the molar mass of cholesterol $M = 386.4\,\text{g/mol}$ [110] and the Avogadro constant $\mathrm{N_A}$. The particle density of the desorbate yields

$$n_{\text{Cholesterol}} \approx 2 \times 10^{18}\,\text{cm}^{-3}.$$

It is worth noting that for a smaller desorption radius $r = 50\,\mu\text{m}$, the particle density of the desorbate of cholesterol yields $n_{\text{Cholesterol}} = 2 \times 10^{21}\,\text{cm}^{-3}$. Hence, the estimation of $r = 500\,\mu\text{m}$ is considered as a lower limit. The particle density of the desorbate of propazine with $M = 229.1\,\text{g/mol}$ [110] and $r = 500\,\mu\text{m}$ yields $n_{\text{Propazine}} \approx 3 \times 10^{18}\,\text{cm}^{-3}$. In conclusion, the particle density of the desorbate an analyte is related to the quantification limits of the method, but not to the transients of the compounds and thus the signal length in the chromatogram. Therefore, the shape of the signal in the chromatogram and thus short or long signals do not impact the limit of detection. This conclusion implies that the signal time t is $t \gg {}^{1}/_{f_{\text{MS}}}$, with the sampling rate f_{MS} of the mass spectrometer.

In the following, the substrate is set perpendicular to the inlet of the mass spectrometer with the plasma parallel to the substrate as in Figure 3.2. In this case, the laser beam propagates through glass but is absorbed and reflected by the Chromium from the cavity design of the substrates. The glass does not significantly absorb the laser beam. The reflectivity of Chromium is roughly 10 % higher than the Coppers reflectivity [111], which means that the desorption efficiency should decrease. The same experimental conditions as before are used in the following experiment.

In Figure 7.2, the relative ion intensity of cholesterol is shown for the laser application

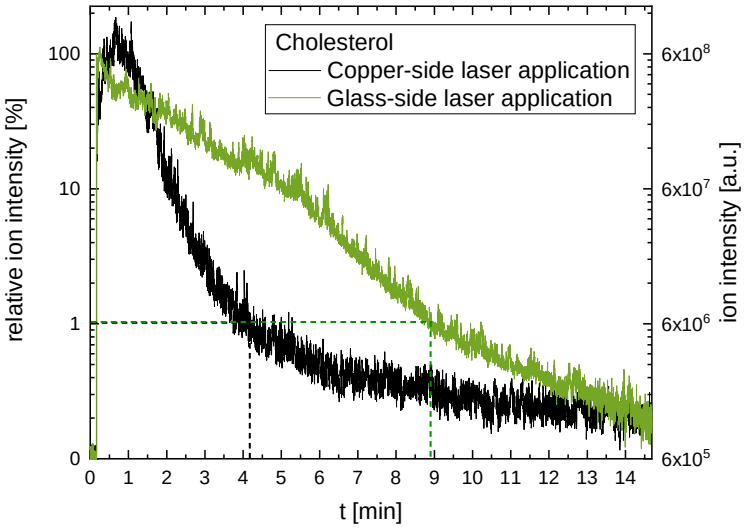

Figure 7.2: Extracted ion mass chromatograms of cholesterol (m/z 369.8) for both Copper and glass side laser application ($m = 0.55\,\mu g$). [52]

from the Copper and the glass side, normalized for the beginning of the respective falling edges as in Figure 7.1. The Copper-side laser application known from Figure 7.1 is only listed for comparison. The ion intensity is comparable in both settings, but the decrease rate of the ion signal differs. The decrease rate for cholesterol with the laser application from the glass-side can be read from the dashed lines in Figure 7.2:

$$\frac{\delta N}{\delta t} \approx \frac{100}{510\,\mathrm{s}} \approx 0.2\,\mathrm{s}^{-1}.$$

Thus, the decrease rate is in the same order of magnitude for both experimental settings, but slightly longer for the glass-side laser application. This longer decrease rate might be linked to a slower heat propagation on the substrate. This effect is generally favorable for imaging applications, in which heat propagation is unwanted. However, the different decrease rates for cholesterol do not change its limit of detection in either experimental setting, as discussed previously.

7.2 Desorption Limits in Ambient Air

Although mass spectrometry at ambient air benefits from little to no sample preparation and decreased lab time, it suffers from its unstable experimental conditions. In the following, a desorption limit is estimated, which allows to investigate the

robustness of the method. The upcoming experiment will evaluate the ion signal loss with an increasing distance between the substrate and the ion source. The plasma source remains on the same spot, but the substrate is moved. The laser spot is moved accordingly in order to keep the focus to the substrate. For the following experiment, the AGC is turned off and the injection time is set to 2 ms. The mass window is $\delta m/z$ 364.8-374.8.

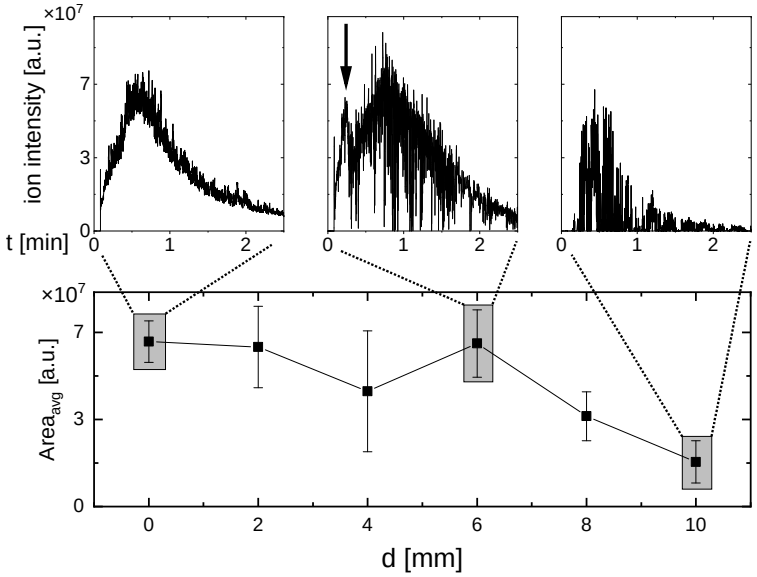

Figure 7.3: Integrated area of the extracted ion mass chromatograms of cholesterol (m/z 369.8) with highlighted ion currents of the signal at $d = (0 \pm 1)$ mm, $d = (6 \pm 1)$ mm and $d = (10 \pm 1)$ mm ($m = 195$ ng). [52]

In the upper part of Figure 7.3, extracted ion mass chromatograms of cholesterol (m/z 369.8) are shown at three different distances d of the substrate to the plasma. The lower part of the figure shows the time-integrated ion intensities up to $d = 10$ mm of distance.

A continuous ion signal is shown in the upper left chromatogram, as the substrate is placed close to the ion source at $d = (0 \pm 1)$ mm. This signal course replicates the cholesterol signal of the previous section.

At a distance of $d = 6$ mm from the ion source, the ion signal becomes unstable. The signal continuously increases up to a laser application time of 10 s, as indicated in the upper middle chromatogram. After this duration, the signal fluctuates becomes increasingly unstable. The reason for this observation may be that the flow of the desorbate is subject to a velocity distribution. In this sense, it is assumed that only the desorbate ejected with a velocity higher than 5 mm/s is detected in the first 10 s.

However, a second ion peak can be observed after the initial peak. This second peak may be related to the diffusion of slower desorbate. The overall amplitude and course of the ion response are comparable to the figure in the upper left. Anyhow, this observation is surprising, as the mean free path in ambient air is within nanometers. In this sense, a bigger ion loss was expected.

At a distance of $d = 10\,\text{mm}$, only single ion peaks with ion intensities up to approximately 5×10^7 a.u. (approximately 71 % of the maximum ion signal of 7×10^7 a.u. from the previous figures) can be observed. This length may replicate the length of the desorption plume as only a few ions are detected. Further, the drift time of the desorbate increases at this position. However, the drift time of the particles is strongly influenced by the atmospheric conditions and the collisions of the particles at ambient air. As a result, laser desorption at a distance of 6 mm and above requires guided particle transport into the MS.

7.3 Ionization Limits of the Flexible Microtube Plasma

If the desorbate is ionized by the plasma, charged particles propagate into the MS. In a similar sense as seen with the desorbate, the ion signal will be lower or completely lost, if the analyte ions are not efficiently guided into the MS. This issue will be the central part of this section.

7.3.1 Tuning the Ion Transport with a Bias Potential

In theory, the glass of the capillary of the FμTP will polarize from the externally applied electric field. After breakdown of the discharge, ions accumulate on the inner walls of the capillary. These ions form an intrinsic electric field that accelerate the charged particles from the glass orifice to the grounded inlet of the MS. Technically, this charge accumulation can be compared to the functionality of a capacitor. This issue has been addressed by Klute *et al.* [16]. The authors connected capacitors to the grounded electrode of a DBD. These capacitors were charged by the charged particles of the plasma.

MALDI- and SALDI-based methods use an externally applied bias potential on the desorption substrate to tune their ion yields by focusing (funneling) ions to the inlet of the MS [97, 112]. Likewise, a bias potential on the desorption substrate will

be used to alter the pathway of the ions from the FμTP. In contrast to MALDI, such a bias potential is more complex with a plasma present in the method. The bias potential generates an electric field from the substrate to the inlet of the MS that accelerates the ions either from or to the MS, depending on the polarity of the potential and the charge of the particles. This electric field will overlap with the intrinsic field by the FμTP. Depending on their superposition, the tuning effects might be different from MALDI.

It is worth noting that the laser also generates an electric field, which may be comparably high to the intrinsic electric field induced by the FμTP and thus cause ion dispersion. However, the Poynting vector of the laser points in the direction of the laser beam and perpendicular to its electric field. Thus, the electric field created by the laser is parallel to the substrate and thus neglectable for the following experiments.

In the following experiment, the desorption substrate is placed at a distance of 1 mm from the inlet of the MS. In contrast to previous measurements, only the plasma ion current is used. As the plasma ions are the protonation partners for the analyte ions, their tunings are directly correlated. Further, the plasma ions are assumed to be a convolution of a constant signal with white noise. In other words, the time-integrated area of the ion signal and the averaged ion intensity only differ by a constant factor. Thus, the averaged ion current is measured for simplicity. These two time-decreasing efforts are mandatory to avoid long-term drifts in the ion intensity.

Each measurement is averaged over 100 mass spectra of the ion source, with a fixed ion injection time of 55 ms without AGC. The mass window is $\delta m/z$ 100-500.

In Figure 7.4, the ion intensity, normalized for the base peak of the spectrum, is shown for different voltages that are applied to the desorption substrate. The ions are detected in both ionization modes of the MS. The black line belongs to the negative ions, the red line to the positive ions. Ions can be detected from approximately -950 V to +250 V in negative mode and from roughly -400 V to +900 V in positive mode. Furthermore, sudden ion drops to zero ions can be observed out of the aforementioned limits. In positive mode, the ion intensity is at its maximum without any bias potential. In negative mode, the maximum is at approximately +200 V.

As stated, the bias potential generates an electric field between the substrate and the grounded inlet of the MS, thus accelerates the ions to the inlet or the substrate,

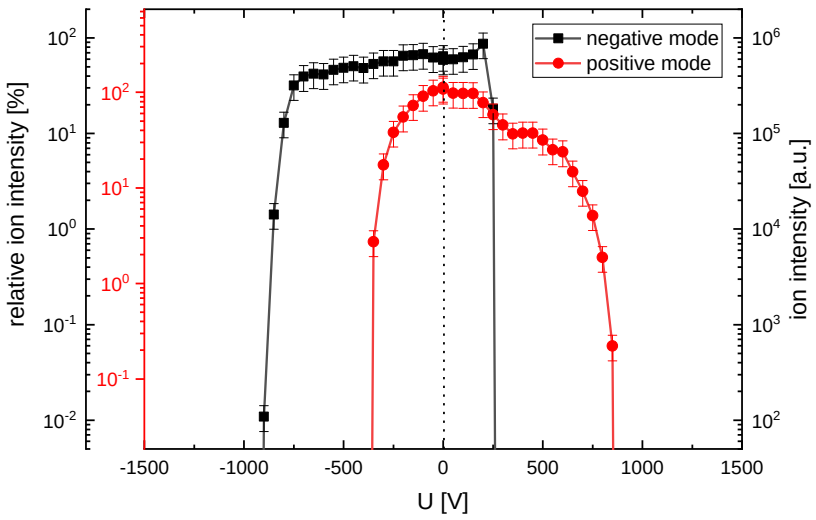

Figure 7.4: Ion intensity normalized for base peak of the plasma ions, with different external bias voltages applied to the Copper-glass substrate. [52] Voltage generator: *PNC1500-40, Knürr-Heizinger*, Germany

depending on its polarity. However, the highest ion current for the positive ions is achieved without any bias potential. This interpretation fits to the observation that the dielectrics of the glass capillary act as a capacitor [16], as previously mentioned. A positive bias potential on the substrate may add to the field of the capillary and further accelerate the ions until they seem to overshoot the tube lens in the skimmer region of the MS and are no longer detected. In contrast, a negative potential seems to decrease the electric field of the capillary, until the electric field lines switch directions to the substrate and cause deflection of the positive ions.

The kinetic energy of the ions after the acceleration in the electric field of the FμTP and the bias potential must be higher than the two-step potential barrier of the transfer capillary and the tube lens of the MS. However, changing the tube lens offset and the capillary voltage only resulted in an ion intensity decrease. Therefore, the ions are not accelerated in the electric field of the bias potential but rather slowed down by collisions with the other particles. This is the reason why the tuning is beneficial in MALDI at vacuum conditions, but not in plasma-based methods at ambient air.

For the negative ions, a slightly positive bias potential results in the highest ion signal. This offset fits to the previous conclusions of a charged capillary. However, the positive polarity of the bias potential is unexpected, as a positive bias potential should accelerate the negative ions to the substrate. This result suggests that the

phenomenon is more complex and cannot be accessed through a single experiment. For instance, the potential raised from the accumulated ions on the walls of the glass capillary may oscillate with each voltage cycle of the square-wave signal. In this sense, residual charges from previous voltage cycles and thus the floating potential on the glass can make this effect more dynamic. In conclusion, a tuning of the ion detection efficiency using bias potentials on the substrate is not feasible, even though they have a major influence on the ion path. Therefore, the voltage drop or electric field gradient from the glass capillary to the inlet of the MS is optimal for the ion detection.

The distance from the substrate to the inlet mainly influences the reproducibility of this experiment. However, the ion detection limits fluctuate with $\pm 100\,\mathrm{V}$ intraday. Deviations of $\pm 200\,\mathrm{V}$ are observed interday and after repositioning of the substrate. These differences might be related to charge effects on the desorption substrate.

7.3.2 Charge Effects on the Desorption Substrate

As mentioned in the previous section, the ion detection limit with an applied bias potential to the substrate is only constant between directly successive experiments but not after several hours. This deviation indicates that plasma ions accumulate on the substrate.

This memory effect can be assessed with an electrometer on the substrate that allows to estimate the ion loss of the plasma. The data is extracted with a data acquisition interface and the charge on the Copper-glass substrate is measured at a sampling rate of $f = 100\,\mathrm{Hz}$ for $10\,\mathrm{s}$ per point.

In Figure 7.5, the detected and averaged signal of the charge δQ_{avg} per time interval δs is shown for increasing distances d from the inlet of the MS. In closer distances than 2 mm, the FµTP bends towards the Copper substrate, which results in unstable experimental conditions. Therefore, the first data is taken at a distance of 2 mm from the ion source. Without any plasma ignition, there is no charge on the substrate. After exceeding the breakdown voltage of the plasma, the substrate charges increasingly positive. $0.12\,\mu\mathrm{C/s}$ are collected on the substrate at a distance of $d = 2\,\mathrm{mm}$. From a distance of $d = 4\,\mathrm{mm}$, the charge decrease in distance with $1/d^2$ in accordance to the electric field of a point charge. On a Copper surface of $20\,\mathrm{mm} \times 25\,\mathrm{mm}$, this equals to a current density of $0.24 \times 10^{-3}\,\mathrm{Cs^{-1}\,m^{-2}}$.

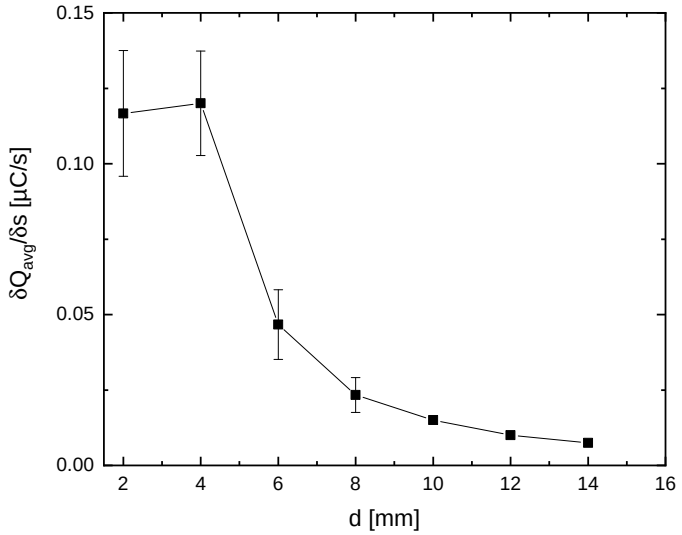

Figure 7.5: Averaged charge δQ_{avg} per time interval δs on the Copper-glass substrate with increasing distances d from the inlet of the MS, measured with a sampling rate of $f = 100\,\text{Hz}$ for 10 s each. [52] Electrometer (input high): *Model 6514, Keithley*, USA. DAQ: *USB-6341 BNC DAQ, National Instruments*, USA.

This charge accumulation reduces the electric field generated by the charged glass capillary and confines further ion loss to the substrate. Therefore, the substrate acts as a floating potential electrode to the plasma, which confines the ion plume to the inlet of the mass spectrometer.

8 Summary

This thesis focused on a systematic study on fast laser desorption coupled with plasma ionization in mass spectrometry, which was applied to analytical standards as well as biological tissue. As part of this study, its inherent effects were studied from both physical and chemical sides and used to construct optimized substrates for the method, separately for analytical standards and imaging of biological tissue.

The first two chapters included the essence of thermal, laser-based desorption and soft, plasma-based ionization in mass spectrometry as well as the coupling of these methods. The third chapter dealt with the experimental design and the characterization of the coupling. In chapter 4, a continuous-wave diode laser was applied to a substrate for the desorption of analytical standards. For this reason, Copper-glass sandwich-structured substrates were designed, which allowed for a more reproducible protocol in mass spectrometric experiments. The analyte was placed in a cavity of 1 mm inner diameter, which was formed by photo-resistive coating and a hydrophobic polymer.

A focus of the upcoming section was the laser-surface interaction to understand the laser application phenomena, which triggered laser desorption. Investigations on the surface modifications showed that liquefied Copper entered the glass as soon as the softening point of the glass was reached. This experiment indicated that the local surface temperature was above 1000 °C. Despite the high surface temperature, the laser heating did not increase the fragmentation degree of the analytes. An interpretation of this outcome led to the conclusion that an air buffer similar to the Leidenfrost effect was formed above the surface, which shielded the analyte from excessive fragmentation.

The metal liquefaction phenomenon initially suggested that a laser-induced plasma was formed on the surface. However, as no ions were detected by the mass spectrometer without the ion source and no characteristic light emission was detected from the substrate by an ICCD camera either, the formation of a laser-induced plasma

was excluded. However, continuously emitted light was detected by the camera. Therefore, it was assumed that this light was related to glowing metal. Interestingly, this glowing was fully developed within microseconds, thus it was assumed that the desorption took place on the same time scale. In conclusion, a synchronization of the plasma source and the laser was not needed for the desorption of analytical standards, as the sampling rate of the mass spectrometer was several orders of magnitude smaller than the joint time scale of the laser desorption and the plasma ionization.

Another key element of the chapter was related to the laser intensity thresholds for different hydrophobic compounds. That section proved that laser desorption did not depend only on the temperature and the temporal temperature gradient on the surface, but also on the desorption threshold of each analyte. These thresholds ranged from $7\,\mathrm{W/mm^2}$ for ibuprofen to $36\,\mathrm{W/mm^2}$ for different lipid classes and were linked to the surface modifications on the substrate.

In chapter 5, the method proved soft ionization capabilities and demonstrated similarities to other plasma- and electrospray-based ionization techniques, such as low temperatures plasmas (LTP) or desorption electrospray ionization (DESI). Different ionization mechanisms were observed, such as the dimerization and the fragmentation of non-steroidal anti-inflammatory drugs or the oxygen addition to polyunsaturated molecules such as beta-carotene. Further, complex matrices such as blood plasma or extracts with a given lipid profile were presented. In this sense, known fragmentation patterns of certain lipid classes were confirmed, such as the neutral loss of the phosphocholine head group of sphingomyelin. However, not all lipids shared the same sensitivity and signal stability in detection. In this sense, certain lipids were detected at the same mass, for instance the fragment dehydrated cholesterol gained from cholesterol and cholesterol ester.

A calibration of the ion signal to the amount of the analyte placed on the substrate was possible, as the analyte was effectively desorbed from the surface. This calibration curve yielded the quantification limits of the analytes. The limit of detection (LOD) for cholesterol was 460 fg, doubling in a complex matrix. The LOD for the herbicide propazine was 140 fg. The locally high surface temperature did not increase the fragmentation degree of the analyte, but rather decreased it. This was exemplarily shown for propazine, whose fragmentation degree decreased from 14 % in a previous publication [18] to 2 % with this method.

Other used analytical standards are summarized in Table A.8 in the appendix. These results yielded essential practical values for the desorption of unknown analytes from biological samples in the next chapter.

In chapter 6, the transition from standards to biological samples was made. The aim of this chapter was to provide an easy-to-use, fast and robust method for screening of biological tissue in ambient air. Only little sample preparation was required for the tissue as the method was matrix-free. However, the substrate required a different design and an adaption of the experimental parameters. For this reason, a grid of Copper spots with a diameter of 30 µm and a defined gap of 10 µm was constructed on microscope glass slides. This design was matched to the properties of the focused diode laser and the quantification limits of cholesterol from the previous chapter. The diode was switched from continuous to pulsed operation to confine the laser-induced thermal spread on the biological sample. The pulsing characteristic was gradually matched to the heat propagation on the biological tissue. One drawback was that the diode laser could not be arbitrarily pulsed, as the pulsing is connected to a loss of laser output power.

Furthermore, an imaging software for the synchronization of the mass spectrometer to the method was developed and presented, including an offset correction to the substrate and a stabilization of the laser focus. Further, two imaging modes namely step-by-step and line scanning at a constant speed as well as its inherent effects were compared and discussed. The experimental duration of step-by-step scanning was reduced from two days down to roughly six hours using a regular low-resolution ion trap mass spectrometer and a self-made integration tool for data processing after the measurement. That tool reconstructed the image from the data even for low abundant signals including a blacklist, a plausibility test and void signals. As a results of these efforts, the morphology of the tissue was validated.

Dehydrated cholesterol was imaged on mouse liver tissue and yielded different ion intensities. However, the imaging of biological tissue in this method is not only limited to cholesterol. In Figure 8.1, mass spectra gained from the mouse liver, kidney and brain are shown. These spectra show further imaging possibilities in upcoming experiments. For instance, imaging of cholesterol in non-alcoholic fatty liver or in mice with a certain phenotype looks promising, as it may draw conclusions of different diseases. However, high-resolution mass spectrometry, standards or tracking of fragmentation patterns are required for the identification of these lipids.

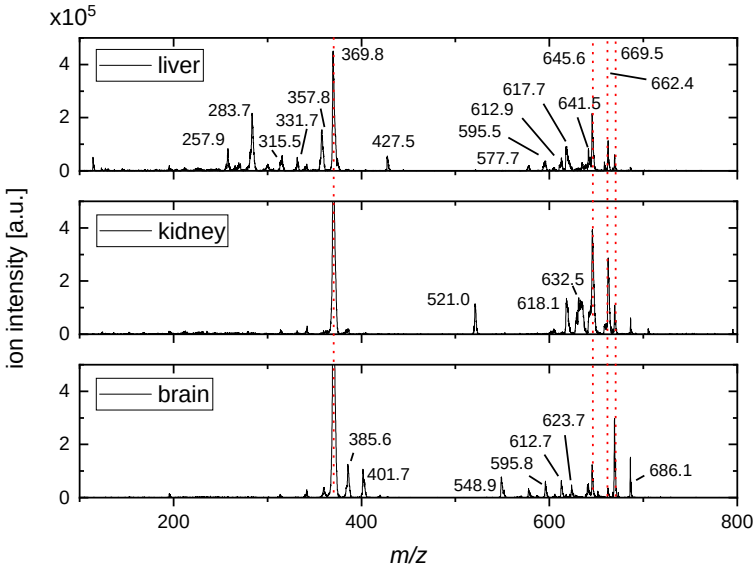

Figure 8.1: Mass spectra gained from the mouse liver, kidney and brain tissue, which are measured with an ion trap mass spectrometer on pure Copper-glass substrates with the same experimental conditions of chapter 6. [53] Dehydrated cholesterol (m/z 369.8) can be identified as the main peak of the spectrum. Further, phospholipids and glycerophospholipids around m/z 600 are detected. On the one hand, all three tissue share several lipids of the same detected mass, for instance at m/z 645.6, m/z 662.4 and m/z 669.5. On the other hand, other compounds are only detected in one or the other tissue, such as m/z 521.0 in the kidney, m/z 385.6 in the brain or m/z 283.7 in the liver.

Finally, this method was compared to methods carried out in vacuum conditions and other imaging methods at ambient air. This comparison showed that the working pressure played an important role for the achievable spatial resolution. Further, ambient air experiments generally come along with a higher ion background, thus a lower signal to noise ratio. However, no bias potentials, external heating or vacuum conditions were needed in contrast to other methods such as matrix-assisted laser desorption ionization (MALDI). In this sense, the flexibility of the ambient air design of the method was both an advantage and a disadvantage as it simplified the experiment, but also decreased its sensitivity.

In chapter 7, the limits of the method were evaluated. The ion response was comparable in two different experimental configurations. The decrease rates of the desorbates of cholesterol and propazine were measured and showed that the herbicide is four times more transient than cholesterol, with decrease rates at $2.0\,\mathrm{s}^{-1}$ for propazine and $0.5\,\mathrm{s}^{-1}$ for cholesterol. The particle densities of the desorbates of cholesterol and propazine were estimated to approximately $10^{18}\,\mathrm{cm}^{-3}$ and were only correlated to their quantification limits, but neither to the aforementioned transients of these compounds nor to their signal courses in the chromatogram. Further desorption limits were evaluated in distances further away from the inlet of the mass spectrometer. The ion signal of the desorbate was stable up to a distance of $(6 \pm 1)\,\mathrm{mm}$ to the inlet of the mass spectrometer. This result showed that no guided transport is necessary for the desorbate.

The pathway of the plasma ions was altered using a bias potential on the substrate in order to address the ionization limits of the method. However, due to the overlap of several electric fields, no increase in the ion yield was observed. This was in contrast to MALDI methods, in which such a bias potential is mandatory. An interpretation of this result was that collisions prevented the acceleration of the ions in the electric field. Moreover, several inherent properties of the ionization source were revealed, such as the ion deposition on the walls of the glass capillary. This effect guided charged particles to the mass spectrometer and the substrate. The charge on the substrate was measured with $0.12\,\mu\mathrm{C/s}$ and formed a floating potential on the substrate, which consequently acted as a floating potential electrode to the ion source.

Apart from the scope of this thesis, several research branches emerged from its results despite the field of imaging. As different analytes showed distinct threshold

intensities, these analytes may be bound to the surface with a certain binding energy. A method to measure this binding energy is known from gases and smaller molecules [113, 114] and called temperature-programmed desorption. In this method, the thermal desorption rate is quantified with a rising surface temperature separately for each compound. First, the thermal desorption rate is calculated on the basis of the partial pressure in a vacuum chamber using the ion current of a mass spectrometer or a pressure sensor. Second, the surface temperature is measured using a sensitive thermal or IR camera. These results yield the binding energy of the adsorbate. In addition, this method may be applied to the laser desorption of this thesis and may enable thermally controlled desorption. In addition to the binding energy of the adsorbate, this method yields the purity and the catalytic activity of the surface. The latter observable is particularly interesting, as Copper may also show catalytic effects [115] during laser desorption coupled with plasma ionization and thus may influence the ionization mechanisms.

Another interesting outlook of the imaging relates to homogenized liver tissue. The idea is to provide a known concentration of the analyte in the tissue, which may require four steps. First, frozen liver is mashed to produce a homogeneous mixture with a fixed but unknown amount of the analyte. This method has been used in literature for decades already [116]. Second, calibration curves can be created from diluted extracts of the homogenate, which allow to link the amount of the analyte to the ion intensity of the mass spectrometer. Third, microtome cuts of the homogenate may allow to estimate the matrix effects from the tissue. Finally, the ion intensity measured in imaging is compared to the calibration curves and the matrix effects from the homogenate to report not only on the spatial distribution and an ion intensity, but also on the amount of the analyte inside the tissue.

Bibliography

[1] C. L. Feider *et al.*, "Ambient Ionization Mass Spectrometry: Recent Developments and Applications", *Analytical Chemistry* **2019**, *91*, 4266–4290, ISSN: 0003-2700, DOI 10.1021/acs.analchem.9b00807.

[2] S. F. Wong *et al.*, "Multiple charging in electrospray ionization of poly(ethylene glycols)", *The Journal of Physical Chemistry* **1988**, *92*, 546–550, ISSN: 0022-3654, DOI 10.1021/j100313a058.

[3] R. B. Cody *et al.*, "Versatile new ion source for the analysis of materials in open air under ambient conditions", *Analytical Chemistry* **2005**, *77*, 2297–2302, ISSN: 0003-2700, DOI 10.1021/ac050162j.

[4] Y. Liu *et al.*, "Imaging mass spectrometry with a low-temperature plasma probe for the analysis of works of art", *Angewandte Chemie - International Edition* **2010**, *49*, 4435–4437, DOI 10.1002/anie.200906975.

[5] R. G. Cooks *et al.*, "Detection Technologies. Ambient mass spectrometry", *Science* **2006**, *311*, 1566–1570, DOI 10.1126/science.1119426.

[6] P. Nemes, A. Vertes, "Laser ablation electrospray ionization for atmospheric pressure, in vivo, and imaging mass spectrometry", *Analytical Chemistry* **2007**, *79*, 8098–8106, ISSN: 0003-2700, DOI 10.1021/ac071181r.

[7] B. Feng *et al.*, "Ambient mass spectrometry imaging: plasma assisted laser desorption ionization mass spectrometry imaging and its applications", *Analytical Chemistry* **2014**, *86*, 4164–4169, ISSN: 0003-2700, DOI 10.1021/ac403310k.

[8] H. M. Mott-Smith, I. Langmuir, "The Theory of Collectors in Gaseous Discharges", *Physical Review* **1926**, *28*, 727–763, ISSN: 0031-899X, DOI 10.1103/PhysRev.28.727.

[9] E. Mühlberger, R. D. Kremith, US Patent US4328257A, System and method for plasma coating, **1979**.

[10] G. Lister *et al.*, "The physics of discharge lamps", *Reviews of Modern Physics* **2004**, *76*, 541–598, ISSN: 0034-6861, DOI 10.1103/RevModPhys.76.541.

[11] C. S. Wu *et al.*, "Plasma arc welding: Process, sensing, control and modeling", *Journal of Manufacturing Processes* **2014**, *16*, 74–85, DOI 10.1016/j.jmapro.2013.06.004.

[12] M. M. Nudnova *et al.*, "Active capillary plasma source for ambient mass spectrometry", *Rapid communications in Mass Spectrometry* **2012**, *26*, 1447–1452, DOI 10.1002/rcm.6242.

[13] F. Paschen, "Ueber die zum Funkenübergang in Luft, Wasserstoff und Kohlensäure bei verschiedenen Drucken erforderliche Potentialdifferenz", *Annalen der Physik* **1889**, *273*, 69–96, ISSN: 00033804, DOI 10.1002/andp.18892730505.

[14] D. Janasek *et al.*, "Scaling and the design of miniaturized chemical-analysis systems", *Nature* **2006**, *442*, 374–380, DOI 10.1038/nature05059.

[15] B. Gilbert-López *et al.*, "Ambient diode laser desorption dielectric barrier discharge ionization mass spectrometry of nonvolatile chemicals", *Analytical Chemistry* **2013**, *85*, 3174–3182, ISSN: 0003-2700, DOI 10.1021/ac303452w.

[16] F. D. Klute *et al.*, "Systematic Comparison between Half and Full Dielectric Barrier Discharges Based on the Low Temperature Plasma Probe (LTP) and Dielectric Barrier Discharge for Soft Ionization (DBDI) Configurations", *Analytical Chemistry* **2017**, *89*, 9368–9374, ISSN: 0003-2700, DOI 10.1021/acs.analchem.7b02174.

[17] S. Brandt *et al.*, "Flexible Microtube Plasma (F-µTP) as an Embedded Ionization Source for a Microchip Mass Spectrometer Interface", *Analytical Chemistry* **2018**, *90*, 10111–10116, ISSN: 0003-2700, DOI 10.1021/acs.analchem.8b01493.

[18] B. Gilbert-López *et al.*, "Performance of dielectric barrier discharge ionization mass spectrometry for pesticide testing: a comparison with atmospheric pressure chemical ionization and electrospray ionization", *Rapid communications in Mass Spectrometry* **2013**, *27*, 419–429, DOI 10.1002/rcm.6469.

[19] Thermo Fisher Scientific Inc., Hardware manual LCQ Series, **2003**, https://conquerscientific.com/wp-content/ad_images/2014/04/finnigan-lcq-series-manual.pdf (visited on 08/13/2020).

[20] Thermo Fisher Scientific Inc., Hardware manual TSQ Series, **2010**, https://assets.thermofisher.com/TFS-Assets/CMD/manuals/TSQ-Series-Hardware.pdf (visited on 01/11/2021).

[21] H. Sun, *Laser diode beam basics, manipulations and characterizations*, Springer, Dordrecht, **2012**, ISBN: 9789400746640.

[22] H. J. Eichler *et al.*, *Lasers: Basics, Advances and Applications*, Springer International Publishing, Cham, **2018**, ISBN: 9783319998947, DOI 10.1007/978-3-319-99895-4.

[23] M. Anani *et al.*, "InxGa1−xN refractive index calculations", *Microelectronics Journal* **2007**, *38*, 262–266, ISSN: 00262692, DOI 10.1016/j.mejo.2006.11.001.

[24] A. Overberg *et al.*, "Matrix-assisted infrared-laser (2.94 µm) desorption/ionization mass spectrometry of large biomolecules", *Rapid communications in Mass Spectrometry* **1990**, *4*, 293–296, DOI 10.1002/rcm.1290040808.

[25] E. Nordhoff *et al.*, "Matrix-assisted laser desorption/ionization mass spectrometry of nucleic acids with wavelengths in the ultraviolet and infrared", *Rapid communications in Mass Spectrometry* **1992**, *6*, 771–776, DOI 10.1002/rcm.1290061212.

[26] E. Nordhoff *et al.*, "Comparison of IR- and UV-matrix-assisted laser desorption/ionization mass spectrometry of oligodeoxynucleotides", *Nucleic acids research* **1994**, *22*, 2460–2465, DOI 10.1093/nar/22.13.2460.

[27] P. Kraft *et al.*, "Infrared, surface-assisted laser desorption ionization mass spectrometry on frozen aqueous solutions of proteins and peptides using suspensions of organic solids", *Journal of the American Society for Mass Spectrometry* **1998**, *9*, 912–924, DOI 10.1016/S1044-0305(98)00063-4.

[28] A. J. Fresnel, *Oeuvres complètes d'Augustin Fresnel, Vol. 1*, Impr. Impériale, **1866**.

[29] D. Bäuerle, *Laser Processing and Chemistry*, 4th ed., Springer-Verlag Berlin Heidelberg, Berlin, Heidelberg, **2011**, ISBN: 9783642176135, DOI 10.1007/978-3-642-17613-5.

[30] *CRC handbook of chemistry and physics: A ready-reference book of chemical and physical data*, 84th ed., (Ed.: D. R. Lide), CRC Press, Boca Raton, **2003**, ISBN: 0849304849.

[31] M. S. Brown, C. B. Arnold in *Laser Precision Microfabrication*, (Eds.: K. Sugioka *et al.*), Springer Series in Materials Science, Springer Berlin Heidelberg, Berlin, Heidelberg, **2010**, pp. 91–120, ISBN: 978-3-642-10522-7, DOI 10.1007/978-3-642-10523-4_4.

[32] H. D. Young, F. W. Sears, *University physics*, 7th ed., Addison-Wesley Pub. Co, Reading, Mass., **1992**, ISBN: 0201529815.

[33] National Center for Biotechnology Information, PubChem Compound Summary for CID 14915, Chromium trioxide; 23978, Copper, **2020**, (visited on 08/13/2020).

[34] M. W. Chase, *NIST-JANAF thermochemical tables*, 4th ed., American Chemical Society, Woodbury, New York, **1998**, ISBN: 1563968207.

[35] U. Bahr *et al.*, "Mass spectrometry of synthetic polymers by UV-matrix-assisted laser desorption/ionization", *Analytical Chemistry* **1992**, *64*, 2866–2869, ISSN: 0003-2700, DOI 10.1021/ac00046a036.

[36] K. Hiraoka, *Fundamentals of Mass Spectrometry*, Springer New York, New York, **2013**, ISBN: 9781461472339, DOI 10.1007/978-1-4614-7233-9.

[37] J. H. Gross, *Massenspektrometrie*, Springer Berlin Heidelberg, Berlin, Heidelberg, **2013**, ISBN: 978-3-8274-2980-3, DOI 10.1007/978-3-8274-2981-0.

[38] H. Kettling *et al.*, "MALDI mass spectrometry imaging of bioactive lipids in mouse brain with a Synapt G2-S mass spectrometer operated at elevated pressure: improving the analytical sensitivity and the lateral resolution to ten micrometers", *Analytical Chemistry* **2014**, *86*, 7798–7805, ISSN: 0003-2700, DOI 10.1021/ac5017248.

[39] J. M. Spraggins *et al.*, "Next-generation technologies for spatial proteomics: Integrating ultra-high speed MALDI-TOF and high mass resolution MALDI FTICR imaging mass spectrometry for protein analysis", *Proteomics* **2016**, *16*, 1678–1689, DOI 10.1002/pmic.201600003.

[40] M. Kompauer *et al.*, "Atmospheric pressure MALDI mass spectrometry imaging of tissues and cells at 1.4µm lateral resolution", *Nature methods* **2017**, *14*, 90–96, DOI 10.1038/nmeth.4071.

[41] A. P. Quist *et al.*, "Total yield measurements in matrix-assisted laser desorption using a quartz crystal microbalance", *Rapid communications in Mass Spectrometry* **1994**, *8*, 149–154, DOI 10.1002/rcm.1290080204.

[42] P. M. V. Raja, A. R. Barron, *Physical Methods in Chemistry and Nano Science*, **2019**, ISBN: 978-1300065449, (visited on 08/13/2020).

[43] M. Niehaus *et al.*, "Transmission-mode MALDI-2 mass spectrometry imaging of cells and tissues at subcellular resolution", *Nature methods* **2019**, *16*, 925–931, DOI 10.1038/s41592-019-0536-2.

[44] M. A. Lieberman, A. J. Lichtenberg, *Principles of plasma discharges and materials processing*, 2nd ed., Wiley-Interscience, Hoboken, N.J, **2005**, ISBN: 0471720011, DOI 10.1002/0471724254.

[45] M. Kaufmann, *Plasmaphysik und Fusionsforschung*, 2nd ed., Springer Fachmedien Wiesbaden, Wiesbaden, **2013**, ISBN: 9783658032388, DOI 10.1007/978-3-658-03239-5.

[46] F. F. Chen, *Introduction to Plasma Physics and Controlled Fusion*, Third edition, Springer, Cham et al., **2016**, ISBN: 9783319223087, DOI 10.1007/978-3-319-22309-4.

[47] F. D. Klute *et al.*, "Capillary Dielectric Barrier Discharge: Transition from Soft Ionization to Dissociative Plasma", *Analytical Chemistry* **2016**, *88*, 4701–4705, ISSN: 0003-2700, DOI 10.1021/acs.analchem.5b04605.

[48] A. Schütz *et al.*, "Tuning Soft Ionization Strength for Organic Mass Spectrometry", *Analytical Chemistry* **2016**, *88*, 5538–5541, ISSN: 0003-2700, DOI 10.1021/acs.analchem.6b01131.

[49] A. Schütz *et al.*, "Soft Argon-Propane Dielectric Barrier Discharge Ionization", *Analytical Chemistry* **2018**, *90*, 3537–3542, ISSN: 0003-2700, DOI 10.1021/acs.analchem.7b05390.

[50] J. D. Harper *et al.*, "Low-temperature plasma probe for ambient desorption ionization", *Analytical Chemistry* **2008**, *80*, 9097–9104, ISSN: 0003-2700, DOI 10.1021/ac801641a.

[51] I. Adamovich *et al.*, "The 2017 Plasma Roadmap: Low temperature plasma science and technology", *The Journal of Physical Chemistry* **2017**, *50*, 323001, ISSN: 0022-3654, DOI 10.1088/1361-6463/aa76f5.

[52] A. Knodel *et al.*, "Detection and Evaluation of Lipid Classes and Other Hydrophobic Compounds Using a Laser Desorption/Plasma Ionization Interface", *Analytical Chemistry* **2020**, DOI 10.1021/acs.analchem.0c03839, ISSN: 0003-2700.

[53] A. Knodel *et al.*, "Matrix-Free, Ambient Air Imaging of Mouse Liver Tissue on Copper-Glass Spots by Laser Desorption Plasma Ionization Mass Spectrometry", **2021**, *Manuscript submitted for publication.*

[54] Lasertack GmbH, LDM-448-3500-C Blue Laser Module, **2020**, https://lasertack.com/Media/Default/Uploaded/Datasheets_software/LDM-448-3500-(C).pdf (visited on 09/07/2020).

[55] Lasertack GmbH, LDM-450-1600-C Blue Laser Module, **2020**, https://lasertack.com/Media/Uploaded/Datasheets_software/LDM-450-1600-C.pdf (visited on 06/18/2020).

[56] OptoTools GmbH, OTF30P-40, web.archive.org/web/20050222231235fw_/http://www.optotools.de/web_english/elements/pdfs/OTF30P-40_eng.pdf (visited on 09/14/2020).

[57] S. Brandt *et al.*, Patent WO/2018/224307, Method For Ionizing Gaseous Samples By Means Of A Dielectric Barrier Discharge And For Subsequently Analyzing The Produced Sample Ions In An Analysis Appliance, **2020**.

[58] F. D. Klute, "Characterization of dielectric barrier discharges for analytical applications", *Technische Universität Dortmund* **2019**, DOI 10.17877/DE290R-20612.

[59] N. P. Bansal, R. H. Doremus, *Handbook of glass properties*, Acad. Pr, Orlando, **1986**, ISBN: 0120781409.

[60] A. Knodel *et al.*, "Standardization of Sandwich-Structured Cu-Glass Substrates Embedded in a Flexible Diode Laser-Plasma Interface for the Detection of Cholesterol", *Analytical Chemistry* **2020**, *92*, 4663–4671, ISSN: 0003-2700, DOI 10.1021/acs.analchem.0c00311.

[61] M. S. Zediker *et al.*, Eds., Blue laser diode (450 nm) system for welding copper, *Vol. 10514*, Proceedings of SPIE, SPIE, Bellingham, Washington, USA, **2018**, ISBN: 9781510615137, DOI 10.1117/12.2291716.

[62] MicroChemicals GmBH, Technical Data Sheet: TechniEtch Cr01, https://www.microchemicals.com/products/etching_mixtures/technietch_cr01chromium_etchant.html (visited on 07/09/2020).

[63] *Laser ablation and its applications*, (Ed.: C. R. Phipps), Springer, New York, NY, **2007**, ISBN: 9780387304526.

[64] S.-B. Olenici-Craciunescu *et al.*, "Characterization of a capillary dielectric barrier plasma jet for use as a soft ionization source by optical emission and ion mobility spectrometry", *Spectrochimica Acta Part B: Atomic Spectroscopy* **2009**, *64*, 1253–1258, DOI 10.1016/j.sab.2009.10.001.

[65] F. J. Lara-Ortega *et al.*, "Direct olive oil analysis by mass spectrometry: A comparison of different ambient ionization methods", *Talanta* **2018**, *180*, 168–175, DOI 10.1016/j.talanta.2017.12.027.

[66] M. Moini, "Ultramark 1621 as a calibration/reference compound for mass spectrometry. II. Positive- and negative-ion electrospray ionization", *Rapid communications in Mass Spectrometry* **1994**, *8*, 711–714, DOI 10.1002/rcm.1290080910.

[67] A. R. Tall, D. M. Small in *Advances in lipid research*, (Eds.: R. Paoletti, D. Kritchevsky), Advances in Lipid Research, Academic Press, New York, **1980**, pp. 1–51, ISBN: 9780120249176, DOI 10.1016/B978-0-12-024917-6.50007-0.

[68] R. A. Cox, M. R. García-Palmieri, *Clinical Methods: The History, Physical, and Laboratory Examinations: Cholesterol, Triglycerides, and Associated Lipoproteins*, 3rd ed., Boston, **1990**, ISBN: 040990077X.

[69] K. G. Heinrich, "Efficacy of injections of phosphatidylcholine into fat deposits-a non-surgical alternative to liposuction in body-contouring", *Indian Journal of Plastic Surgery* **2005**, *38*, 119–122, DOI 10.1055/s-0039-1699118.

[70] S. Szanto, J. Yudkin, "The effect of dietary sucrose on blood lipids, serum insulin, platelet adhesiveness and body weight in human volunteers", *Postgraduate medical journal* **1969**, *45*, 602–607, DOI 10.1136/pgmj.45.527.602.

[71] R. L. Atkinson *et al.*, "Human adenovirus-36 is associated with increased body weight and paradoxical reduction of serum lipids", *International journal of obesity* **2005**, *29*, 281–286, DOI 10.1038/sj.ijo.0802830.

[72] J. E. Vance, "Dysregulation of cholesterol balance in the brain: contribution to neurodegenerative diseases", *Disease models & mechanisms* **2012**, *5*, 746–755, DOI 10.1242/dmm.010124.

[73] A. Hubaux, G. Vos, "Decision and detection limits for calibration curves", *Analytical Chemistry* **1970**, *42*, 849–855, ISSN: 0003-2700, DOI 10.1021/ac60290a013.

[74] E. Voigtman, *Limits of Detection in Chemical Analysis*, John Wiley & Sons, Inc, Hoboken, New Jersey, **2017**, ISBN: 9781119189008, DOI 10.1002/9781119189008.

[75] C. Wu *et al.*, "Rapid, direct analysis of cholesterol by charge labeling in reactive desorption electrospray ionization", *Analytical Chemistry* **2009**, *81*, 7618–7624, ISSN: 0003-2700, DOI 10.1021/ac901003u.

[76] H.-Y. Hsieh *et al.*, "Quantification of Endogenous Cholesterol in Human Serum on Paper Using Direct Analysis in Real Time Mass Spectrometry", *Analytical Chemistry* **2017**, *89*, 6146–6152, ISSN: 0003-2700, DOI 10.1021/acs.analchem.7b00943.

[77] S. Peng *et al.*, "A new interface to couple thin-layer chromatography with laser desorption/atmospheric pressure chemical ionization mass spectrometry for plate scanning", *Rapid communications in Mass Spectrometry* **2005**, *19*, 2789–2793, DOI 10.1002/rcm.2120.

[78] H. Hayen *et al.*, "Dielectric barrier discharge ionization for liquid chromatography/mass spectrometry", *Analytical Chemistry* **2009**, *81*, 10239–10245, ISSN: 0003-2700, DOI 10.1021/ac902176k.

[79] E. Kofronová *et al.*, "A comparison of HPLC/APCI-MS and MALDI-MS for characterising triacylglycerols in insects: species-specific composition of lipids in the fat bodies of bumblebee males", *Journal of chromatography. B Analytical technologies in the biomedical and life sciences* **2009**, *877*, 3878–3884, DOI 10.1016/j.jchromb.2009.09.040.

[80] F. Donot *et al.*, "Analysis of neutral lipids from microalgae by HPLC-ELSD and APCI-MS/MS", *Journal of chromatography. B Analytical technologies in the biomedical and life sciences* **2013**, *942-943*, 98–106, DOI 10.1016/j.jchromb.2013.10.016.

[81] Avanti Polar Lipids Inc., Liver Extract Total: Liver Total Lipid Extract (Bovine), avantilipids.com/product/181104 (visited on 06/18/2020).

[82] J. Milnes *et al.*, "The laser desorption/laser ionization mass spectra of some anti-inflammatory drugs", *International Journal of Mass Spectrometry and Ion Processes* **1994**, *132*, 49–55, DOI 10.1016/0168-1176(93)03921-8.

[83] I. R. Miksa *et al.*, "Multi-residue determination of anti-inflammatory analgesics in sera by liquid chromatography–mass spectrometry", *Journal of analytical toxicology* **2005**, *29*, 95–104, DOI 10.1093/jat/29.2.95.

[84] R. N. O. Tettey-Amlalo, I. Kanfer, "Rapid UPLC-MS/MS method for the determination of ketoprofen in human dermal microdialysis samples", *Journal of pharmaceutical and biomedical analysis* **2009**, *50*, 580–586, DOI 10.1016/j.jpba.2008.09.051.

[85] M. Gué, G. Schroeder, "Application of Molecularly Imprinted Polymers (MIP) and Flowing Atmospheric-Pressure Afterglow Mass Spectrometry (FAPA-MS) to Analysis of Nonsteroidal Anti-Inflammatory Drugs (NSAIDs)", *Applied Sciences* **2020**, *10*, 4217, DOI 10.3390/app10124217.

[86] J. P. Williams, J. H. Scrivens, "Rapid accurate mass desorption electrospray ionisation tandem mass spectrometry of pharmaceutical samples", *Rapid communications in Mass Spectrometry* **2005**, *19*, 3643–3650, DOI 10.1002/rcm.2251.

[87] V. N. Emel'yanenko *et al.*, "Dissecting intermolecular interactions in the condensed phase of ibuprofen and related compounds: the specific role and quantification of hydrogen bonding and dispersion forces", *Physical chemistry chemical physics* **2020**, *22*, 4896–4904, DOI 10.1039/c9cp06641a.

[88] Y.-J. Kim *et al.*, "Fluorometric assay of DNA in cartilage explants using Hoechst 33258", *Analytical Biochemistry* **1988**, *174*, 168–176, DOI 10.1016/0003-2697(88)90532-5.

[89] T. P. Misko *et al.*, "A fluorometric assay for the measurement of nitrite in biological samples", *Analytical Biochemistry* **1993**, *214*, 11–16, DOI 10.1006/abio.1993.1449.

[90] V. H. Cohn, J. Lyle, "A fluorometric assay for glutathione", *Analytical Biochemistry* **1966**, *14*, 434–440, DOI 10.1016/0003-2697(66)90286-7.

[91] R. Castaing, G. Slodzian, "Microanalysis by secondary ionic emission", *Journal of Microscopy* **1962**, *1*, 395–410.

[92] M. Karas *et al.*, "Influence of the wavelength in high-irradiance ultraviolet laser desorption mass spectrometry of organic molecules", *Analytical Chemistry* **1985**, *57*, 2935–2939, ISSN: 0003-2700, DOI 10.1021/ac00291a042.

[93] V. V. Laiko *et al.*, "Atmospheric pressure matrix-assisted laser desorption/ionization mass spectrometry", *Analytical Chemistry* **2000**, *72*, 652–657, ISSN: 0003-2700, DOI 10.1021/ac990998k.

[94] J. M. Wiseman *et al.*, "Tissue imaging at atmospheric pressure using desorption electrospray ionization (DESI) mass spectrometry", *Angewandte Chemie - International Edition* **2006**, *45*, 7188–7192, DOI 10.1002/anie.200602449.

[95] J.-C. Wolf *et al.*, "Direct and Sensitive Detection of CWA Simulants by Active Capillary Plasma Ionization Coupled to a Handheld Ion Trap Mass Spectrometer", *Journal of the American Society for Mass Spectrometry* **2016**, *27*, 1197–1202.

[96] V. Garikapati *et al.*, "High-resolution atmospheric-pressure MALDI mass spectrometry imaging workflow for lipidomic analysis of late fetal mouse lungs", *Scientific reports* **2019**, *9*, 3192, DOI 10.1038/s41598-019-39452-3.

[97] S. N. Jackson *et al.*, "AP-MALDI Mass Spectrometry Imaging of Gangliosides Using 2,6-Dihydroxyacetophenone", *Journal of the American Society for Mass Spectrometry* **2018**, *29*, 1463–1472, DOI 10.1007/s13361-018-1928-8.

[98] Thorlabs Inc., NPL Series of Nanosecond Pulsed Lasers, www.thorlabs.com/_sd.cfm?fileName=TTN122959-D02.pdf&partNumber=NPL45C (visited on 12/09/2020).

[99] A. Zavalin *et al.*, "Tissue protein imaging at 1-µm laser spot diameter for high spatial resolution and high imaging speed using transmission geometry MALDI TOF MS", *Analytical and bioanalytical chemistry* **2015**, *407*, 2337–2342, DOI 10.1007/s00216-015-8532-6.

[100] K. A. Z. Berry *et al.*, "MALDI imaging of lipid biochemistry in tissues by mass spectrometry", *Chemical reviews* **2011**, *111*, 6491–6512, DOI 10.1021/cr200280p.

[101] M. C. Sullards *et al.*, "Analysis of mammalian sphingolipids by liquid chromatography tandem mass spectrometry (LC-MS/MS) and tissue imaging mass spectrometry (TIMS)", *Biochimica et biophysica acta* **2011**, *1811*, 838–853, ISSN: 0006-3002, DOI 10.1016/j.bbalip.2011.06.027.

[102] Y. Sugiura, M. Setou, "Selective imaging of positively charged polar and nonpolar lipids by optimizing matrix solution composition", *Rapid communications in Mass Spectrometry* **2009**, *23*, 3269–3278, DOI 10.1002/rcm.4242.

[103] Y. Schober *et al.*, "Single cell matrix-assisted laser desorption/ionization mass spectrometry imaging", *Analytical Chemistry* **2012**, *84*, 6293–6297, ISSN: 0003-2700, DOI 10.1021/ac301337h.

[104] S. M. Cologna, "Mass Spectrometry Imaging of Cholesterol", *Adv. Exp. Med. Biol. (Advances in experimental medicine and biology)* **2019**, *1115*, 155–166, DOI 10.1007/978-3-030-04278-3_7.

[105] M. L. Kraft, H. A. Klitzing, "Imaging lipids with secondary ion mass spectrometry", *Biochimica et biophysica acta* **2014**, *1841*, 1108–1119, ISSN: 0006-3002, DOI 10.1016/j.bbalip.2014.03.003.

[106] L. Morosi *et al.*, "Determination of Paclitaxel Distribution in Solid Tumors by Nano-Particle Assisted Laser Desorption Ionization Mass Spectrometry Imaging", *PloS one* **2013**, *8*, DOI 10.1371/journal.pone.0072532.

[107] B. Yan *et al.*, "Direct Tissue Mass Spectrometry Imaging by Atmospheric Pressure UV-Laser Desorption Plasma Postionization", *Journal of the American Society for Mass Spectrometry* **2020**, DOI 10.1021/jasms.0c00315.

[108] J. Tillner *et al.*, "Faster, More Reproducible DESI-MS for Biological Tissue Imaging", *Journal of the American Society for Mass Spectrometry* **2017**, *28*, 2090–2098, DOI 10.1021/jasms.8b05382.

[109] A. Moreno-Pedraza *et al.*, "Elucidating the Distribution of Plant Metabolites from Native Tissues with Laser Desorption Low-Temperature Plasma Mass Spectrometry Imaging", *Analytical chemistry* **2019**, *91*, 2734–2743, DOI 10.1021/acs.analchem.8b04406.

[110] National Center for Biotechnology Information, PubChem Compound Summary for CIDs 5997, Cholesterol; 14077841, Cholesterol Margarate; 5280489, Beta-Carotene; 9939941, N-Palmitoylsphingomyelin; 512874 1,2-Dilauroyl-sn-Glycero-3-Phosphocholine; 445639, Oleic Acid; 3672, Ibuprofen; 3825, Ketoprofen and 4937, Propazine, **2020**, (visited on 08/13/2020).

[111] Z. Sárosi *et al.*, Evaluation of reflectivity of metal parts by a thermo-camera, **2010**, DOI 10.3929/ETHZ-A-006206911.

[112] M. Koestler *et al.*, "A high-resolution scanning microprobe matrix-assisted laser desorption/ionization ion source for imaging analysis on an ion trap / Fourier transform ion cyclotron resonance mass spectrometer", *Rapid communications in Mass Spectrometry* **2008**, *22*, 3275–3285, DOI 10.1002/rcm.3733.

[113] P. A. Redhead, "Thermal desorption of gases", *Vacuum* **1962**, *12*, 203–211, DOI 10.1016/0042-207X(62)90978-8.

[114] D. A. King, "Thermal desorption from metal surfaces: A review", *Surface Science* **1975**, *47*, 384–402, DOI 10.1016/0039-6028(75)90302-7.

[115] H. Adkins *et al.*, "The Copper—Chromium Oxide Catalyst for Hydrogenation 1", *Journal of the American Chemical Society* **1950**, *72*, 2626–2629, ISSN: 0002-7863, DOI 10.1021/ja01162a079.

[116] J. Stocks *et al.*, "Assay using brain homogenate for measuring the antioxidant activity of biological fluids", *Clinical science and molecular medicine* **1974**, *47*, 215–222, ISSN: 0301-0538, DOI 10.1042/cs0470215.

List of Figures

List of Tables

Appendix: Settings and Parameters, Chemicals, Substrate Recipes and Analytical Standards

This appendix includes settings and parameters that are not of immediate interest for the reader, but are nevertheless important to reproduce the experiments. The following sections will only include parameters and settings of the specified method or system.

1 Mass Spectrometry

The settings of the Paul ion trap *LCQ Deca XP* and the triple quadrupole *TSQ Vantage*, both *Thermo Fisher Scientific*, USA, are summarized in Table A.1 and Table A.2.

Table A.1: Common working parameters for the LCQ

Component	Setting
API Source	
Mass range ($\delta m/z$)	100-1000
Injection time (IT) / ms	20
full MS AGC target	5×10^7
Capillary voltage / V	4
Capillary temperature / K	523
Tube Lens voltage / V	49
Vacuum	
Convectron gauge / Pa	121.3
Ion gauge / Pa	0.2
Ion Optics (most important parameters only)	
Multipole RF amplitude 2.45 MHz peak-peak / V	400.00
Quadrupole 1 offset / V	-7.54
Interoctapole Lens offset / V	-14.05
Quadrupole 2 offset / V	-10.32
Mass Analyzer	
Coarse trap offset / V	-10.39
Fine trap offset / V	-10.26
Ion Detection System	
Dynode voltage / V	-14840
Multiplier / V	-833

Table A.2: Common working parameters for the TSQ

Component	Setting
API Source	
Mass range ($\delta m/z$)	100-1000 (full scan)
	368.6-370.1 (SIM)
Cycle time / ms	10
Capillary voltage / V	0.1
Capillary temperature / K	523
S-Lens amplitude at 650 kHz (m/z 360) / V	$\approx$ 90
Vacuum	
see Table A.1	
Ion Optics	
Q_{00} amplitude (m/z 300) / V	232
Q_{00} offset / V	-3
Lens 0 offset / V	-0.7
Q_0 amplitude (m/z 300) / V	232
Q_0 offset / V	-1.7
Lens 1-1 offset / V	-2.0
Lens 1-2 offset / V	-40.0
Q1 offset / V	-8.0
Q1 RF amplitude (1.123 MHz, m/z 300) / V	84.0
Lens 2-1 offset / V	-15.0
Lens 2-2 offset / V	-225.0
Lens 2-3 offset / V	-15.0
Q2 offset / V	-10.0
Q2 RF amplitude (1.123 MHz, m/z 300) / V	400.0
Lens 3-1 offset / V	-15.0
Lens 3-2 offset / V	-225.0
Lens 3-3 offset / V (m/z 360)	$\approx$ -21.0
Mass Analyzer	
Q3 offset (m/z 360) / V	-2.5
Q3 RF amplitude (m/z 300, 1.123 MHz) / V	10000
Q3 resolution [0.6 FWHM, m/z 360] / V	-12.3
Q3 calibration [0.6 FWHM, m/z 360] / V	-2.16
Ion Detection	
Dynode voltage / V	-14911
Multiplier voltage / V	-740

2 Chemicals

The chemicals used within this thesis are listed in Table A.3.

Table A.3: Chemicals and solvents used in this study, added by appearance and with manufacturer.

Compound	Solvent
Cholesterol (95 %, *Merck*, Germany)	Chloroform (*Rotipuran*, *Carl Roth*, Germany)
Bovine total liver extract (*Avanti Polar Lipids*, USA)	Chloroform:Methanol (delivered in solution by the manufacturer)
Cholest-5-en-3-yl heptadecanoate (*Avanti Polar Lipids*, USA)	Chloroform (*Rotipuran*, *Carl Roth*, Germany)
1,2-dilauroyl-sn-glycero-3-phosphocholine (*Avanti Polar Lipids*, USA)	Chloroform (*Rotipuran*, *Carl Roth*, Germany)
Sphingomyelin (from chicken egg, *Sigma-Aldrich*, USA)	Chloroform:Methanol (1:1) $CHCl_3$: *Rotipuran*,*Carl Roth*, Germany, MeOH: ULCMS grade, *Biosolve BV*, Netherlands)
Beta-carotene (95 %, HPLC grade, *Sigma-Aldrich*, USA)	Chloroform:Methanol (2:1) $CHCl_3$: *Rotipuran*, *Carl Roth*, Germany, MeOH: ULCMS grade, *Biosolve BV*, Netherlands)
Ibuprofen (*Sigma-Aldrich*, USA)	Acetonitrile (*Sigma-Aldrich*, USA)
Ketoprofen (*Sigma-Aldrich*, USA)	Acetonitrile (*Sigma-Aldrich*, USA)
Oleic Acid (*Sigma-Aldrich*, USA)	Methanol (*Sigma-Aldrich*, USA)
Propazine (Pestanal Grade, *Sigma-Aldrich, USA*)	Methanol, dilution in Ethyl Acetate MeOH: *Sigma-Aldrich*, USA, $C_4H_8O_2$: *LiChrosolv*, *Merck*, Germany

3 Substrate Recipes

The desorption substrates are build on lithography and sputtering. These processes will be summarized in this section. The parameters used in spin coating are listed as total rotational frequency (revolutions per minute, [rpm])/acceleration (rpm)/total time (s). The soda lime glass mask (127 mm×127 mm×2.3 mm) used for lithography

is commercially available and constructed with a low reflective chromium layer on top. The tolerance given by the manufacturer (*Rose Fotomasken*, Germany) is 0.35 µm with a defect density of 0.2 cm^{-2}.

3.1 Desorption Substrates for Analytical Standards

The recipe to build substrates used for desorption of analytical standards is summarized in Table A.4.

Table A.4: Settings used in the lithography, sputtering and in the post processing.

Preparation (adhesive layer)
Cleaning, Drying, Preheat (150 °C, 15 minutes)
Option 1: HDMS & N_2 fill, polymerization (150 °C, 15 minutes)
Option 2: 1 ml SU8-2, spin coating (500/100/15 – 3500/500/40)
Manufacturer: *Kayakuam Advanced Materials*, formally *MicroChem*, USA
Softbake (95 °C, 2 minutes)
Light exposure (λ = 365 nm, 10 s, I_L = 6 mW/cm^2)
Post-Exposure bake (95 °C, 2 minutes)
Application of the coating (structural layer)
1 ml SU8-25, spin coating (500/100/15 → 1500/500/30 → 4000/2500/4),
Manufacturer: *Kayakuam Advanced Materials*, formally *MicroChem*, USA
Softbake (95 °C, 5 minutes)
Light exposure (λ = 365 nm, 7 s, I_L = 6 mW/cm^2)
Post-Exposure bake (95 °C, 5 minutes)
Polymerization
Developer: mr-dev 600 (bathing 4 minutes+2 minutes, rinse)
Manufacturer: *micro resist technology GmbH*, Germany
Hardbake (95 °C to 160 °C, 5 minutes)
Sputtering
Cr: 200 W, Argon flow of 60 sccm for 5 minutes with aperture
Cu: 250 W, Argon flow of 40 sccm for 1 minute without aperture and
200 W, Argon flow of 80 sccm for 10 minutes without aperture
Post processing
60 µL HP310 (80 °C, 5 minutes & 160 °C, 120 minutes)
Manufacturer: *SurA Chemicals GmbH*, Germany
Cutting the slides with a water-cooled wafer saw
10 000 rpm, feed 0.7 cm/m, chuck distance 500 µm

3.2 Desorption Substrates for Tissue

The steps to built substrates used for imaging of biological tissue are summarized in Table A.5.

Table A.5: Settings used in the lithography, sputtering and in the post processing.

Preparation (adhesive layer)
Cleaning in peroxymonosulfuric acid (80 °C, 60 minutes)
Sputtering Copper using the settings of Table A.4
Application of the coating (adhesive / structural layer)
1 ml AZ 5214E , spin coating (4400/2000/30)
Manufacturer: *MicroChemicals GmbH*, Germany
Softbake (90 °C, 2 minutes)
Light exposure (λ = 365 nm, 40 s, I_L = 6 mW/cm^2)
Development
Developer: AZ 351B (diluted 2:1 with deionized water,
bathing 1 minutes to 2.5 minutes, rinse)
Manufacturer: *MicroChemicals GmbH*, Germany
Etching
Sodium persulfate (100 g/L, 20 s to 40 s)

4 White-light interferometry

The settings used in white-light inteferometry are summarized in Table A.6.

Table A.6: Settings used for white-light interferometry.

Property	Setting
Zoom	0.4
Objective	20x (Mirau), 4.7 mm working distance
Scan length	20 µm bipolar
Minimum modulation	0.001 %
Effective size	640x480 px, f = 30 Hz, full aperture
	11 µm pixel spacing, 2.43 µm/s scan speed
Resolution FDA	Centroid peak detection, FFT including phase offset
Vertical resolution	0.1 nm
AGC, Phase resolution	On

5 Optical Emission Spectroscopy

The settings for ICCD and laser operation are listed in Table A.7.

Table A.7: Settings used for ICCD and diode laser operation. The TTL trigger settings are also listed.

Property	Setting
Gate delay / µs	13
Gate width / ns	500
Accumulations	50
Gain	150
Input slit width / µm	10
Chip temperature / °C	−15
Laser pulse frequency / kHz	10
U_{pp} / V	1.86
U_{offset} / V	0.93
Laser intensity / W/mm^2	16

6 Analytical Standards

The analytical standards, their mono-isotopic [110] and detected mass, ion mode, identification and ion intensity are summarized in Table A.8. The mono-isotopic mass is given in **u**nified atomic mass unit, also known as Dalton (Da).

Table A.8: Standards used within this thesis. MRFA, marked with an asterisk, is not detected in laser desorption, plasma ionization mass spectrometry. For Ultramark 1621, only the most abundant species is listed. BP is abbreviated for base peak, the highest ion current in the spectrum.

Compound	Mass / u	Ion mode	*m/z*	Identification	BP?
Caffeine, $m = 10\,\mathrm{ng}$	194.1	+	195.5	$[\mathrm{M+H}]^+$	
MRFA*, $m = 0.5\,\mathrm{ng}$	523.7	+	524.42	$[\mathrm{M+H}]^+$	
Ultramark 1621, 5 ng	1721.0	+	1721.7	$[\mathrm{M+H}]^+$	x
Cholesterol,	386.4	+	369.8	$[\mathrm{M-H_2O+H}]^+$	x
$m = 0.2\,\mu\mathrm{g}$					
Cholesterol margarate	638.6	+	369.8	$[\mathrm{M-R-COOH+H}]^+$	x
C17, $m = 500\,\mathrm{ng}$		+	656.2	$[\mathrm{M+O+H}]^+$	
Beta carotene,	536.4	+	537.6	$[\mathrm{M+H}]^+$	x
$m = 50\,\mathrm{ng}$		+	553.4	$[\mathrm{M+O+H}]^+$	
Sphingomyelin C16,	702.6	+	521.5	$[\mathrm{M+H-C_5H_{13}NO_4P}]^+$	x
$m = 250\,\mathrm{ng}$					
1,2-dilauroyl-sn-	621.4	+	440.1	$[\mathrm{M+H-C_5H_{13}NO_4P}]^+$	x
glycero-3-phosphocholine					
(DLPC) C12, $m = 50\,\mathrm{ng}$					
Oleic acid, $m = 50\,\mathrm{ng}$	282.3	+	283.6	$[\mathrm{M+H}]^+$	x
			564.0	$[\mathrm{2\,M-H}]^-$	x
Ibuprofen, $m = 250\,\mathrm{ng}$	206.3	+	161.4	$[\mathrm{M-COOH}]^+$	
			207.5	$[\mathrm{M+H}]^+$	x
			224.5	$[\mathrm{M+H_2O}]^+$	
			413.2	$[\mathrm{2\,M+H}]^+$	
		-	205.6	$[\mathrm{M-H}]^-$	
			411.6	$[\mathrm{2\,M-H}]^-$	x
Ketoprofen, $m = 250\,\mathrm{ng}$	254.3	+	255.5	$[\mathrm{M+H}]^+$	x
			272.5	$[\mathrm{M+H_2O}]^+$	
			508.8	$[\mathrm{2\,M+H}]^+$	
		-	253.7	$[\mathrm{M-H}]^-$	
			463.6	$[\mathrm{2\,M-COOH}]^+$	
			507.2	$[\mathrm{2\,M-H}]^-$	x
Propazine, $m = 0.5\,\mu\mathrm{g}$	229.7	+	230.4	$[\mathrm{M+H}]^+$	x

List of Publications and Presentations

The following list includes peer-reviewed papers, both published or submitted, as first and co-author, and given presentations or posters.

Standardization of Sandwich-Structured Cu–Glass Substrates Embedded in a Flexible Diode Laser–Plasma Interface for the Detection of Cholesterol
Alexander Knodel, Ulrich Marggraf, Norman Ahlmann, Sebastian Brandt, Daniel Foest, Bienvenida Gilbert-López, and Joachim Franzke
Analytical Chemistry, 2020, DOI: 10.1021/acs.analchem.0c00311

Detection and Evaluation of Lipid Classes and Other Hydrophobic Compounds Using a Laser Desorption/Plasma Ionization Interface
Alexander Knodel, Daniel Foest, Sebastian Brandt, Norman Ahlmann, Ulrich Marggraf, Bienvenida Gilbert-López, and Joachim Franzke
Analytical Chemistry, 2020, DOI: 10.1021/acs.analchem.0c03839

Matrix-Free, Ambient Air Imaging of Mouse Liver Tissue on Copper-Glass Spots by Laser Desorption Plasma Ionization Mass Spectrometry
Alexander Knodel, Ulrich Marggraf, Edeltraut Hoffmann-Posorske, Sebastian Burhenn, Sebastian Brandt, Norman Ahlmann, Daniel Foest, Kristina Lorenz and Joachim Franzke
Manuscript submitted for publication, 2021.

Review: Miniature dielectric barrier discharge (DBD) in analytical atomic spectrometry

Guanghui Niu, Alexander Knodel, Sebastian Burhenn, Sebastian Brandt and Joachim Franzke

Analytica Chimica Acta, 2020, DOI: 10.1016/j.aca.2020.11.034

Laser Desorption and DBDI for Mass Spectrometry

Kickoff meeting TImPANI, 2018, Nicosia, Cyprus

Sandwich-structured Substrates embedded in a Diode Laser-Plasma Interface for Analytical Chemistry

DGMS, 2020, Münster, Germany

Sandwich-structured Substrates used in a Diode Laser-Plasma Interface for Mass Spectrometry

Department of Physics, Medical and Biological Physics, 2020, Dortmund, Germany

Facets of Ambient Air Diode Laser Desorption/Plasma Ionization Mass Spectrometry

Webinar on novel ionization methods for mass spectrometry, 2021, Jaén, Spain

Danksagung

Vielen Dank an all diejenigen, die mich und diese Arbeit in meiner Promotionszeit von November 2018 bis Ende März 2021 begleitet, unterstützt und gefördert haben. Insbesondere möchte ich dabei namentlich nennen

- Herrn PD Dr. Joachim Franzke – nicht nur als Doktorvater, sondern insbesondere auch für die Faszination an den Dingen, den Einfallsreichtum und die Offenheit selbst. Es hat mir sehr viel Freude bereitet, Dich regelmäßig von Deiner Arbeit abzuhalten! In vielen Gesichtspunkten wurde diese Betreuung also tatsächlich der Bezeichnung "Doktorvater" gerecht. Im Sinne des Arbeitsschutzes möchte ich erwähnen, dass die Diskussionen inzwischen nicht mehr ausschließlich auf Fußböden sitzend ausgetragen werden..

- Herrn Prof. Dr. Manfred Bayer für die zweite Begutachtung und das Interesse an dieser Arbeit.

- Dr. Bienvenida Gilbert López for making me feel and understand the world of analytical chemistry, mass spectrometry, scientific writing and olive oils. I still owe you a Glühwein on the Christmas market – now you have it in written form.

- Ulrich Marggraf für die äußerst angenehme Zusammenarbeit, insbesondere auch für die Expertise im Bereich der *Litho* und des *Sputterns*, dessen Einfluss auf diese Arbeit ganz wesentlich ist.

- Daniel Foest für die endlosen Gespräche über die Arbeit, aber insbesondere auch Gott und die Welt, vor allem während der Zypern-Reisen. Dein Netflix-Geschmack wird meine Psyche noch für viele Jahre prägen.

- Norman Ahlmann für seine einzigartige, lockere und direkte Art und die Kompetenz, schwierige Dinge pragmatisch umzusetzen.

- Dr. Sebastian Burhen insbesondere für den Burhennschen Taxidienst zum Lidlisieren.
- Antje Michels und Dr. David Klute, meinen (ehemaligen) Bürokollegen.
- allen anderen (ehemaligen) Kollegen aus der Arbeitsgruppe Miniaturisierung, den umliegenden AGs und den Werkstättlern, bei dessen Aufzählung ich keinen vergessen möchte. Auch hier fallen mir noch viele schöne Erinnerungen ein, die leider nicht alle in diese Arbeit gepasst haben. Es wurde immer für eine tolle Arbeitsatmosphäre gesorgt und mir mit Rat und Tat zur Seite gestanden.
- meine Freunde, insbesondere Miles, Sebastian (Trauzeugenbonus), Marc, Fabian und noch einigen weiteren, ungenannten, die mich teils schon seit der Schulzeit begleiten und stets mit Rat und Tat zur Seite stehen!
- meine Familie, bestehend aus den beiden Ogern, meinem Bruder und meiner Oma, die alle alleine eine eigene Seite verdient hätten. Danke für die noch immer so vielen schönen Erinnerungen, egal ob an Weihnachten, Ostern oder *mal eben* zwischendurch! Ich hab' Euch immer im Herzen!
- meine Freundin (Update vom 24.03.2021: jetzt Verlobte, bald Frau) Valerie für ihr Dasein als *Hauself* in einer Zeit als die Pandemie und ihre eigene Arbeit sonst nur wenig zugelassen hat. Danke!

The thesis was partially founded by the TImPANI ("twinning in atmospheric Plasma science and applications") project as part of the European Union's Horizon 2020 research and innovation program. I would like to thank the colleagues from Jaén, chaired by Prof. Dr. Juan F. Garciá-Reyes, and Cyprus, chaired by Prof. Dr. George E. Georghiou, for their generosity and open-mindedness whenever we got the chance to see each other before a global pandemic changed plans. These days will be greatly remembered.

Noch ein äußerst ernst zu nehmender, informeller Abschlusshinweis: Falls bei Ihnen irgendwo in dieser Arbeit Verständnisprobleme aufgetaucht sind, dann muss das ganz klar an Ihnen liegen. Fehler meinerseits sind natürlich ausgeschlossen. Warum? Selbst meine Freundin, die nichts mit Laser, Massenspektrometrie oder Plasmen zu tun hatte, hat den Grundgedanken in dieser Arbeit verstanden und dieses (anfängliche Un-)Verständnis in jedem zweiten Absatz fröhlich mit einem *Häää?!* quittiert. Das gilt bekanntermaßen als Qualitätssiegel.